Dynamics of Geyser systems, El Tatio, Atacama

by

Carolina Munoz-Saez

A dissertation submitted in partial satisfaction of the

Requirements for the degree of

Doctor of Philosophy

in

Earth and Planetary Science

in the

Graduation Division

of the

University of California, Berkeley

Committee in charge:
Professor Michael Manga, Chair
Professor Roland Burgmann
Professor Paul Renne
Professor Beatriz Manz

Fall 2016

Dynamics of Geyser systems, El Tatio, Atacama

By

Carolina Munoz-Saez

Abstract

Dynamics of Geyser systems, El Tatio, Atacama

by

Carolina Munoz-Saez

Doctor of Philosophy in Earth and Planetary Science

University of California, Berkeley

Professor Michael Manga, Chair

Geysers are hot springs that periodically or episodically erupt liquid water and vapor. They are uncommon because they require a combination of abundant water recharge, magmatism to supply heat and silica, and fractures or cavities to trap rising multiphase fluids. To better understand the dynamics inside of geyser conduits, interaction between geysers, properties of the surrounding rock, and the origin of the fluid, we collected data in the El Tatio geothermal field, Atacama Desert in Chile, during October 2012 and 2014. We monitored eruption intervals, durations, and discharge through measurements of pressure and temperature within geyser conduits. At the surface, we collected samples for petro-physical and geochemical analysis. We identify that geyser systems evolve over time, including changes in the interval between eruptions, development of new thermal features, and interactions between geysers. Though geysers erupt with different styles, we recognize some common features: the conduit recharges with liquid during the quiescent period, bubbles enter the conduit before eruptions, and eruptions occur when water boils in the upper part of the conduit. Eruptions are triggered by the episodic addition of steam coming from depth suggesting that the dynamics of the eruptions are dominated by geometrical and thermodynamic complexities in the conduit and deeper reservoir. The depth where heat is added dictates the eruption style: conduits with deeper heat input are more likely to show pre-play or minor eruptions. Further evidence favoring the dominance of internal processes in controlling periodicity is also provided by the absence of responses of the geyser to environmental perturbations (air pressure, temperature and Earth tides). The thermal features interact by pressure transmission through subsurface permeable layers, which is consistent with permeability measurements of sinter in the lab. Sinter closely resembles vesicular volcanic rocks and other material formed by precipitation in geothermal settings such as travertine. We find that in fresh geyserite sinter the pore structure, and thus hydrological and geophysical properties, is controlled by the distribution of microbial matter. The geochemistry of water indicates mixing of andesitic and meteoric water. Steam separation, and dilution underground occurs as fluids

rise to the surface. Evaporation at the surface seems to affect thermal pools, fountain geysers, and water in discharge channels.

Table of Contents

List of Figures

List of Tables

Acknowledgement

Living in Berkeley and sharing in this intellectually and socially vibrant community, studying in the Department of Earth and Planetary Science at UC Berkeley and participating in all the student activities have been wonderful experiences. I cannot imagine a better place to spend the last 6 years of my life.

In professional terms, I want specially thank my advisor Michael Manga, who is one of the most knowledgeable people, and the best scientist that I have ever met. I admire his way thinking, professionalism, dedication, generosity and devotion to science. He has been a brilliant mentor; I am really graceful of his availability, patience, and support every time that I need it.

I am also graceful to all my collaborators, especially Atsuko Namiki, Shaul Hurwitz, Max Rudoph, Chi-Yueng Wang, who have generously shared their time and knowledge with me. Thanks to the Committee members of my dissertation Roland Burgmann, Paul Renne, Beatriz Manz. Thanks to Fulbright and Conicyt-Chile, and NSF for funding my research.

I want to thanks to my family and fiends in Chile that have believed in my capacities, and respected my decisions in life. Thank you to the tios Mona and Horacio Mena, and Nancy, and the primas Tania, Mariela, who adopted me as part of their family and give me all the support that I needed being far away from home. Also, I want to thank Yovanka and Amarali, and the araucarias dancers Carolina, Raul Munoz (Q.E.D.), Nestor Cuevas, Poly Gallardo and the kids for all the encouragement. Also, I admire the courage of the Chilean community that had to leave Chile and have become refugees around the world because of their beliefs. Thanks for not loosing hope, keep believing, and actively working in developing a more equal and fair society. Thanks to Mayra, Miguel, and Jenny for all sharing all these life experiences and for the emotional support. Thanks to Fernando and Erin to keep the enthusiasm and the moral of Chile Chico Running Club high. Thanks to my housemates Seth, Adriana, Nacho, and little Venus who made our house into a home. Thanks to Beatriz Manz and Yito Wilson for keeping the Chilean students active and together.

I want to thanks my friends, group mates and officemates from the EPS department, specially David Mangiante, Ian Rose and Seth Saltiel for making my life happier and full of adventures, also for all your emotional and academic support. Thanks to my first year's classmates: Andrea, Jesse, Shuo, Jenn and Ana to make that first year less scary. Thanks to Pam, Eloisa, Felipe, Noah, Mong Han, Kristen, Patrick, and all my friends for your encouragement, perspective, and love.

Chapter 1 Introduction

Hot springs that episodically erupt steam, liquid water, and non-condensable gases are called geysers. Geysers are uncommon compared to other non-eruptive hot springs. Fewer than 1000 geysers have been reported on Earth and most geysers are concentrated in three geyser fields: Yellowstone National Park (Wyoming, United States), Geyser Valley (Kamchatka, Russia), and El Tatio (Atacama, Chile). Other two geyser fields Steam Boat (Nevada, United States) and Taupo (New Zealand) have become extinct due to the development geothermal energy (Bryan, 1995). A special combination of water supply, a heat source, and a particular underground geometry of the conduit/reservoir are required to generate geysers (e.g., White, 1967; Fournier, 1969; Kieffer, 1989; Ingebritsen and Rojstaczer, 1993, 1996; Kedar et al., 1998; Kiryukhin et al., 2012; Belousov et al., 2013; Karlstrom et al., 2013; Shteinberg et al., 2013; Vandemeulebrouck et al., 2013; Namiki et al., 2014; Vandemeulebrouck et al., 2014; Munoz-Saez et al., 2015ab). The episodic release of fluid, especially steam, from cavities underneath the conduit may control geyser periodicity (Mackenzie, 1811; Belousov et al., 2013; Vandemeulebrouck et al., 2013; Adelstein et al., 2014; Munoz-Saez et al., 2015ab). There is also evidence of geysers interacting with other nearby thermal springs (e.g., Scott, 1992, 1994; Munoz-Saez et al., 2015b), which can be attributed to changes of fluid pressure (Rojstaczer et al., 2003). Water erupted from geysers has a high content of silica, which precipitates to form opaline deposits called sinter.

The study of geysers is important because they are diagnostic features of high temperature reservoirs at depth, and provide information about the underlying geothermal systems. Eruption processes in geysers are similar to those operating in volcanoes or hydrothermal eruptions, but are smaller and more frequent; they provide a natural laboratory to study eruptive phenomena (Kieffer, 1984). Studying properties of modern sinter rocks around geysers provides measurements than can improve the interpretation of geophysical surveys and assess fluid transport.

By studying the thermodynamic state and composition of water, and the properties of the rocks around geysers, we can address some long-standing fundamental questions about geyser systems:

- What are processes and thermodynamic conditions in the conduit during the entire cycle? At what depth does the eruption begin? How is heat transported in geyser system?
- Why do so few hot springs erupt as geysers? Why are most geysers concentrated in few areas? How does geology control the distribution of thermal features?
- What is the geometry of subsurface permeable zones? How does this geometry affect the eruption process? Are geysers connected through permeable pathways to other thermal sources? How does this connection affect the eruption cycle? Does sinter play a role in the circulation of fluid?

- How and why does the geyser cycle evolve over time? How do external perturbations including earthquakes, atmospheric conditions, and Earth tides affect the eruption cycle?
- What is the origin of the fluids that erupt? Do geysers and non-eruptive hot spring have the same reservoir?
- What is the longevity of geothermal systems?

To provide answers to these questions we collected data from El Tatio geyser field in Chile in 2012 and 2014. This area presents ideal conditions for studying geyser behaviour: there is a variety of thermal features; more than 200 geothermal features have been reported including ~80 eruptive features at the local boiling temperature of 86°C (Glennon and Pfaff, 2003); the recharge of local meteoric water is limited compared to other geyser around world; and daily variation in atmospheric conditions are large compared to elsewhere.

We collected data of pressure and temperature inside geyser conduits, and we combine this data with observations at the surface; we collected rock samples from sinter structures (cones and terraces) with different relative ages and measure properties in the laboratory; and we collected measurements of the steam flow and water samples from different thermal features. The data analysis and interpretation are presented in four main chapters:

- Chapter 2: We analysed data from a regular geyser with a regular cycle in order to understand the response to environmental forcing and thermodynamics within the geyser conduit.
- Chapter 3: We analysed the evolution of the eruption's characteristics over time and the interaction between hot springs and geysers.
- Chapter 4: We analysed hydraulic and physical properties of the rock samples to better understand modern sinter, interpret geophysical surveys, and controls on the transport of fluids.
- Chapter 5: We analyzed the geochemistry of the water in the entire basin to develop a regional understanding of the source of fluids, differences between thermal sources, processes affecting fluids as they ascend to the surface, and assess the mass balance and energy balance of the geothermal basin.

Finally, in chapter 6 the results and conclusions from each chapter are summarized and recommendations for future research are provided.

Chapter 2 Dynamics within geyser conduits, and sensitivity to environmental perturbations: Insights from a periodic geyser in the El Tatio geyser field, Atacama Desert, Chile

The following chapter includes work previously published in:
Munoz-Saez, C., Manga, M., Hurwitz, S., Rudolph, M.L., Namiki, A. and Wang, C.Y., 2015. Dynamics within geyser conduits, and sensitivity to environmental perturbations: Insights from a periodic geyser in the El Tatio geyser field, Atacama Desert, Chile. Journal of Volcanology and Geothermal Research, 292, pp.41-55.

2.1 Abstract

Despite more than 200 years of scientific study, the internal dynamics of geyser systems remain poorly characterized. As a consequence, there remain fundamental questions about what processes initiate and terminate eruptions, and where eruptions begin. Over a one-week period in October 2012, we collected down-hole measurements of pressure and temperature in the conduit of an exceptionally regular geyser (132 s/cycle) located in the Chilean desert. We identified four stages in the geyser cycle: (1) recharge of water into the conduit after an eruption, driven by the pressure difference between water in the conduit and in a deeper reservoir; (2) a pre-eruptive stage that follows the recharge and is dominated by addition of steam from below; (3) the eruption, which occurs by rapid boiling of a large mass of water at the top of the water column, and decompression that propagates boiling conditions downward; (4) a relaxation stage during which pressure and temperature decrease until conditions preceding the recharge stage are restored. Eruptions are triggered by the episodic addition of steam coming from depth, suggesting that the dynamics of the eruptions are dominated by geometrical and thermodynamic complexities in the conduit and reservoir. Further evidence favoring the dominance of internal processes in controlling periodicity is also provided by the absence of responses of the geyser to environmental perturbations (air pressure, temperature and probably also Earth tides).

2.2 Introduction

Geysers are springs that produce discrete eruptions of steam, liquid water, and non-condensable gases. Their eruptions are smaller and typically more frequent than

volcanoes and hydrothermal eruptions, providing a natural laboratory to study eruptive processes (Kieffer, 1984). Geysers are uncommon; less than 1,000 have been described worldwide, and this number is decreasing due to geothermal energy development (Bryan, 1995). Special conditions are needed for their formation: a supply of water, a source of heat, and a particular system of fractures and/or porous rocks to permit episodic discharge (e.g., White, 1967; Fournier, 1969; Kieffer, 1989; Ingebritsen and Rojstaczer, 1993, 1996; Kedar et al., 1998; Kiryukhin et al., 2012; Belousov et al., 2013; Vandemeulebrouck et al., 2013; Karlstrom et al., 2013; Shteinberg et al., 2013; Namiki et al., 2014; Vandemeulebrouck et al., 2014).

There are several open questions about processes and conditions before, during and after the eruption: how is heat transported to and within the geyser system? Do eruptions begin in a conduit as observed in some laboratory experiments (Adelstein et al., 2014)?, or in a deeper reservoir as proposed from limited observations in natural systems (Belousov et al., 2013; Vandemeulebrouck et al., 2013) and experiments (Steinberg et al., 1982)? What is the geometry of subsurface fractures and how do they affect the eruption process? Previous studies of natural geysers provide at least partial answers to these questions. Some observations indicate that prior to an eruption, temperature in the water column is below boiling, and the boiling is caused by ascent-driven decompression (e.g., Bunsen 1847, Fukutomi, 1942ab; Kieffer, 1984). Conversely, some studies in Yellowstone National Park (USA) suggested that intermittent injection of superheated water leads to eruption (Rinehart, 1972,1980), assuming hydrostatic conditions and that the depth of the measurements (23 m) was accurate. White (1967) proposed that eruptions begin with the discharge of water below the boiling temperature (T_{boil}), progress to a liquid-dominated fountain that becomes steam-rich, and end with a quiescent phase. Seismic observations suggest that steam bubbles are crucial in transferring heat to water in the conduit and in driving the eruption (Kieffer, 1984, 1989). Underground cavities at some geysers may create a "bubble trap" that allows for the accumulation of a two-phase fluid (liquid+steam) in the system and the episodic release of this fluid (Mackenzie, 1811, Belousov et al., 2013, Vandemeulebrouck et al., 2013, 2014, Adelstein et al., 2014).

The response of geyser eruptions to external influences provides additional insight into how they work. Some geysers in Yellowstone respond to local and remote earthquakes (Marler, 1964; Rinehart and Murphy, 1969; Marler and White, 1975; Hutchinson, 1985; Husen et al., 2004ab; Manga and Brodsky, 2006; Hurwitz et al., 2014). The responses of geysers to non-seismic strain (Earth tides, barometric pressure), and weather (atmospheric temperature, rainfall and wind) vary between geysers (e.g., Rinehart, 1972; White and Marler, 1972; Rojstaczer et al., 2003; Hurwitz et al., 2008; Hurwitz et al., 2012; Hurwitz et al., 2014).

Most data used to study geysers comes from observations made at the surface. Data on processes in the subsurface of geysers are limited due to the complexity of taking measurements *in situ*. Active and passive field experiments inside conduits have been

performed at Yellowstone National Park (Birch and Kennedy, 1972, Rinehart, 1972; Hutchinson et al., 1997; Kedar et al., 1998), and Kamchatka (Belousov et al., 2013; Shteinberg et al., 2013). Data from these experiments provided a better understanding of conduit geometry (Hutchinson et al., 1997; Belousov et al., 2013), thermodynamic conditions (Kedar et al., 1998, Hutchinson et al., 1997), and recharge processes (Shteinberg et al., 2013).

We obtained continuous time series of pressure and temperature inside the conduit of a geyser located in El Tatio, northern Chile (Figure 2.1a). This geyser does not have an official name, so we nicknamed it "El Jefe" (Figure 2.1b,c) and use this name throughout the manuscript. This geyser corresponds to feature T35 described in Glennon and Pfaff (2003) as one of the more significant and periodic geysers in the basin. One unusual aspect of the El Tatio geysers is that they are located in the middle of a very dry area, the Atacama Desert, in contrast to other geyser fields in the world (Yellowstone National Park, Kamchatka, Iceland, and New Zealand). The marked daily variation in air pressure and temperature, very high evaporation rates, and the limited meteoric water recharge, make El Tatio's geysers ideal for examining the sensitivity of multiphase systems to external perturbations. A better understanding of "cause and effect" relationship between external conditions and geyser cycle may help to constrain and quantify the processes governing the eruptions.

Down-hole measurements of pressure and temperature from 3,531 eruptions of El Jefe Geyser during one week in October 2012 provide an extensive record of thermodynamic conditions during the entire geyser cycle. We combined these data with measurements at the surface to: 1) examine the geyser's response to environmental forcing, and; 2) better understand the thermodynamics within the geyser conduit.

We begin with a description of the study area. Then, we describe the field measurements and instruments, followed by a compilation of observations and results. We end with an interpretation of the measurements and evaluate proposed hypotheses for the mechanisms leading to geyser eruptions.

2.3 El Tatio geyser field

The El Tatio geyser field contains more than 80 active geysers (Glennon and Pfaff, 2003). It is located in northern Chile at an elevation of 4,200 to 4,300 m. The field is situated among Holocene andesitic stratovolcanoes, which provide the heat for the geothermal system, but there are no historical eruptions (Lahsen, 1976ab). Thermal manifestations develop in the hanging wall of a NS trending half-graben (Figure 2.1a), that is filled with ~ 1000 m of sub-horizontal ignimbrites, tuffs and lavas, and covered by Holocene alluvial and glacial deposits (Healy, 1974; Lahsen and Trujillo, 1975). According to the distribution of the geothermal features, the field is divided into a Lower, Middle and Upper Basin (Glennon and Pfaff, 2003) (Figure 2.1a). Data from geothermal

wells suggest that the permeability is dominated by open fractures in the ignimbrite layers (Cusicanqui et al, 1975, 1976). The maximum temperature measured at the bottom of a 600 m deep geothermal well was 253^{o}C (Lahsen and Trujillo, 1976).

At El Tatio in October 2012, we measured the average daily air temperature and pressure, which vary between approximately -5^{o}C to 20^{o}C and 6.07x10^{4} to 6.10x10^{4} Pa, respectively,. The boiling temperature (T_{boil}) of pure water at these air pressures ranges between 86.2 and 86.4^{o}C (http://webbook.nist.gov/chemistry/fluid/). Evaporation is extremely high, leading to rapid silica deposition (Nicolau et al., 2014).

Most water feeding the geyser field is recharged in the Bolivian Altiplano, 15 to 20 km to the east (Lahsen, 1976; Cusicanqui et al., 1976; Giggenbach, 1978; Munoz and Hamsa, 1993; Cortecci et al., 2005). Discharged thermal waters at the El Tatio area have a pH of 6 to 8, and a conductivity of ~20 mS/cm. Most discharged waters have high concentrations of Cl^{-} (6000 to 8000 mg/l), Na^{+} (>3500 mg/l), SiO_2 (>220 mg/l), and As^{3-} (>30 mg/l), and low SO^{4-} (<50 mg/l), (e.g., Cusicanqui et al., 1976; Fernandez-Turiel et al., 2005; Landrum et al., 2009; Cortecci et al., 2005 ; Tassi et al., 2010 ; Nicolau et al., 2014). Chemical and isotopic characteristics of thermal waters indicate complex mixing between magmatic, meteoric and hydrothermal sources (Cusicanqui et al., 1975; Giggenbach, 1978; Tassi et al., 2005; Tassi et al., 2010).

2.4 Instrumentation and measurements

Between October 20 and 27, 2012, we deployed a set of instruments at the surface and within the conduit of "El Jefe" geyser (Figure 2.1 b,c). To synchronize instruments we used a GPS clock (GlobalSat BU-353 USB GPS Receiver) connected to the computer (HP mini 1000) that started the temperature data loggers.

At the surface, we recorded daytime eruptions simultaneously with a video camera (GoPro, ~30 frames per second) and an infrared video camera (FLIR model A320, ~15 frames per second) for 50 minutes on October 20, 2012. To detect eruptions throughout the experiment, one thermocouple was placed at the geyser "mouth" (top of the geyser conduit at the ground surface) and a second thermocouple was placed 30 cm above the ground surface. Sensors were attached to a rigid steel rod so that they would not move during eruptions. These pre-calibrated type K thermocouples recorded temperature every 1 second and were in contact with water only during the eruption; between eruptions they recorded air temperature. QuadTemp 2000 four channel temperature recorders were used to collect all temperature measurements. Air pressure (P_{air}) was measured every 10 min with a barometer (Setra Model 278).

To measure discharge of the erupted water we placed a rectangular wooden flume (length 65 cm, width 15 cm, height 10 cm) in the wide outflow channel of the geyser. Water discharge was calculated by measuring the velocity of floating objects along the flume using a video camera (videos in electronic supplementary material Munoz-Saez et

al., 2015a), and water level in the flume with a ruler. We made measurements during 6 consecutive geyser cycles. Image analysis obtained from the videos was used to estimate the average discharge. Visual observations suggested that the flume captured only ~ 40-60 % of erupted water, with the rest of the water flowing from the pool at the surface back into the conduit. We were unable to better quantify the fate of erupted water.

A GoPro video camera in a custom-built waterproof and insulated housing was lowered into the upper part of the conduit (up to ~0.5 m depth) for one complete geyser cycle to obtain visual images of the conduit geometry and the level of the water during the cycle (videos in electronic supplementary material). However, we observed only the upper conduit (depth up to ~0.7 to 0.8 m) because of the diminution of conduit diameter at depth, and lack of light. We were able to introduce a rigid measuring stick 1.52 cm below the surface.

Inside the conduit, we deployed six pre-calibrated type K thermocouples spaced 30 cm apart, between the conduit mouth and the bottom of the accessible conduit at a depth of 1.5 m (Figure 2.2). Temperature was measured every 1 second. The error in the temperature measurements is less than 1.1 ^{o}C (http://www.omega.com/thermocouples.html). We attached three absolute pressure transducers mounted in watertight housings (Honeywell models 19C050PA4K and 19C030PA4K) to a rigid metal rod and located them adjacent to the three deeper temperature sensors at 0.9 m, 1.2 m and 1.5 m below the surface (Figure 2.2). Measurements were collected at a frequency of 100 Hz with a 24-bit Nanometrics Taurus logger. The data logger had an internal GPS clock to synchronize the measurements. The transducers were calibrated in the laboratory under conditions resembling the down-hole pressures and temperatures at El Jefe. We measured the ground deformation using a surface tiltmeter with a calibrated resolution of 0.23 μrad/mV (Applied Geomechanics Inc. Surface Mount Tiltmeter Model No. 701-2), at a frequency of 2 Hz from October 20 to 22, 2012. The tiltimeter was located 5 m to the East of the vent. We removed the long-term fluctuations with periods greater than the geyser cycle by using a high pass filter $>2\times10^{-3}$ Hz. We used data only at restricted time periods (October 20th, 22:00-24:00, October 21st 23:00-24:00, October 22nd 00:00-01:00, 04:00-05:00, UTC time) during which the amplitude of noise was relatively small. Even during these short periods the signals were noisy, and we only used data when the maximum tilt within three eruptions was smaller than 10 μrad.

2.5 Data analysis and results

2.5.1 Pressure and temperature time series and the interval between eruptions (IBE)

The evolution of both pressure and temperature in the conduit are very repeatable between eruptions (Figure 2.3a). We calculated the interval between eruptions (IBE) for

every geyser cycle using pressure and temperature measurements. To understand the temporal evolution of a single cycle, we compare time series and video observations of the fountain at the surface. We established seven reference points in time (Figure 2.3a; green stars numbered 1 to 7), which identify different key stages in the eruption.

- Point 1 indicates the beginning of the geyser cycle; it is coincident with the minimum water pressure inside the conduit. After this point, pressure increases while the conduit refills.
- Point 2 shows the beginning of a rapid pressure increase, before an eruption.
- Point 3 indicates a sudden increase in pressure and temperature. The beginning of fountaining occurs between points 3 and 4.
- Point 4 indicates the maximum pressure in the conduit; after this point, pressure decreases at an approximately constant rate.
- Point 5 indicates the maximum water temperature; after this point, temperature decreases at an approximately constant rate.
- At Point 6 the rate of pressure decrease changes, and corresponds to the end of fountaining at the surface.
- Point 7 identifies an increase in the rate of pressure decrease, and the end of the geyser cycle.

During the week of measurements, the mean interval between the 3,531 eruptions (IBE) was 132.2 $\pm$ 2.4 s (Figure 2.3b-d): the eruption itself (points 3 to 7) lasted 51.9 $\pm$ 2.5 s, and the quiescent period (including the time from points 1 to 3 and from 7 to 1) was 80.3 $\pm$ 3.0 s. Uncertainties shown here and elsewhere are one standard deviation.

In the next sections, we summarize the observations, beginning at the surface and moving progressively downward in the conduit.

2.5.2 Surface measurements

1.1.1.1. Geometry of the conduit

The sinter-lined conduit is located in the center of a small depression. The diameter of the conduit opening at the surface is 0.25 m to 0.30 m (the geyser's "mouth" – Figure 2.2b). The conduit remains approximately cylindrical to a depth of 0.8 m, below which it narrows. Because we could insert a metal rod to depths of 1.52 m, at greater depth the conduit either has a constriction with a diameter less than ~2 cm, or it bends (Figure 2.2). Fissures and other cavities of unknown dimensions intersect the conduit (Figure 2.2c). Video observations inside the conduit suggest that during the quiescent period the conduit is partially full of water with the minimum water level (air-water interface) at ~0.75 to 0.8 m of depth. The depth of air-water interface varied during the geyser cycle; it increases by ~0.25 m during the quiescent period.

1.1.1.2. Environmental perturbations

Figure 2.4 shows the power spectra for water pressure and temperature inside the geyser, air temperature and pressure, and Earth tides. At high frequencies we recognized a strong and sharp peak in water pressure and temperature, which corresponds to the IBE (Figure 2.4a). At lower frequencies we identify the daily signals of barometric pressure, atmospheric temperature and tides. The phase and amplitude of solid Earth tides were calculated theoretically by the SPOTL software package (Agnew, 2012).

1.1.1.3. Temperature measurements above the ground surface

We overlapped the time series of temperature above the ground surface (for 2 eruptions) with the infrared video (FLIR) recording. We observed the eruptions of hot water at the surface for only ~35 seconds (Figure 2.5, points 3 to 6), while at depth the water stays hot for longer (Figure 2.5, point 3 to 7). The maximum water ejection height (2 m) observed in the FLIR images coincided with the highest temperature measured by the thermocouple at the ground surface (~83^{o}C), which remained almost constant during the eruption, a few degrees below T_{boil}, due to cooling in the atmosphere (Figure 2.5, points 4 to 5). At the end of the eruption (Figure 2.5, between points 5 and 6), the temperature at the surface sensor decreased rapidly, recording air temperature.

1.1.1.4. Discharge measurements

From discharge measurements we obtained an average volumetric flow rate of 1.9×10^{-3} m^3/s during the eruption, corresponding to a mass flow rate of 1.8 kg/s (using a hot water density of 970 kg/m^3). The water flowed through the flume for ~35 s (the duration eruptions at surface). The measured discharge is a lower bound on the erupted volume since we estimated visually that 40-60% of the water flows back into the geyser rather than flowing through the flume. There are holes in the ground close to the vent that also drained water back to the conduit (videos in electronic supplementary material, Munoz-Saez et al., 2015a). The volume measured flowing through the flume is still probably representative of the average net mass discharge from the system. Given the calculated mass flow rate, the net erupted mass is 66 kg. As this value is perhaps <60 % of the total amount of water erupted, we expect that total mass erupted is >110 kg per cycle. The mean net mass flow rate for a geyser cycle is 0.83 kg/s (total erupted mass divided by IBE).

1.1.1.5. Ground deformation

Figure 2.6a shows water pressure in the conduit, and Figures 2.6b and c show the corresponding tilt of the ground surface. We stacked tilt data of ~130 eruptions and calculated the average shown by black curves in Figures 2.6a and 2.6b. Both tilt vectors indicate that eruptions produce measurable ground deformation. Figure 2.6b shows a small tilt increase during the resting time and a large increase during the eruption, followed by a decrease at the end of eruption. Figure 2.6c for the tangential direction shows an increase of the tilt during the quiescent time; but it does not show a signal at the beginning of the eruption. We cannot exclude the possibility that the temporal tilt pattern could be a result of water ponding in the pool during the eruption rather than subsurface sources of pressure changes.

2.5.3 Measurements in the conduit

Because the temperature and pressure waveforms of all the eruptions are very similar (Figures 2.2 and 2.3), we stacked the waveforms of all 3,531 eruptions and calculated the average value of temperature and pressure throughout an "average" eruption (Figures 2.7 and 2.8).

We define the upper conduit as the part of the conduit without water during quiescent period, from the surface to the air-water interface right before an eruption (~0.6 m from surface). Once water at the air-water interface reaches T_{boil} (Figure 2.7c, points 3 to 4) the eruption starts, and boiling water moves rapidly upward through the conduit, reaching the upper sensors in the conduit (Figure 2.7ab, points 3 to 4), and the surface (Figure 2.5, points 3 to 4). After the ~35 second duration of the eruption (Figure 2.7ab points 3 to 5), temperature decreases continuously as the water level decreases.

The temperature at the top of the water column remains constant at T_{boil} for ~45 seconds (Figure 2.7c, points 3 to 7). Subsequently, the temperature drops ~15 ^{o}C as cooled erupted water from the surface, and air enter into the conduit (Figure 2.7c, points 7 to 1, video in electronic supplementary material, Munoz-Saez et al., 2015a). The high concentration of dissolved ions in the water does not increase the boiling point significantly (<0.15^{o}C for concentrations of 8 g/l of NaCl dissolved in water).

We define the lower conduit as the part of the conduit below the air-water interface before the eruption, to a depth of 1.52 m. We observe that before the eruption (points 1 to 3), the temperature of the water is almost constant at all depths, close to T_{boil}. Temperature in the lower conduit then increases (Figure 2.8, from points 3 to 5) once the geyser is erupting at the surface (Figures 2.5 and 2.7). Pressures at depths of 0.9 m and 1.2 m reach maximum values (Figures 2.8ab) during the first half of the surface eruption (Figures 2.5 and 2.7, from points 3 to 4). However, at a depth of 1.5 m, pressure between points 3 to 4 is almost constant, with a slightly noticeable maximum between these

points. Temperature increases 3±1°C. The very small change in pressure, and comparably larger change in temperature between points 3 and 4, suggest that heat is added, but with little additional mass.

Pressure decreases from points 4 to 7 (Figure 2.8abc), and temperature continues to increase until point 5. Water at a depth of 0.9 m reaches boiling conditions at point 5 (Figure 2.8a). Small changes in temperature and a large decrease in pressure around point 5 are consistent with adiabatic decompression of water in the conduit. Water at the deepest sensors reaches boiling conditions close to point 6 (Figure 2.8bc), suggesting a downward propagation of the boiling front into the conduit (Figure 2.5, 2.7, and 2.8). At a depth of 0.9 m, boiling conditions (Figure 2.8a, points 5 to 7) are maintained beyond the end of the eruption at the surface (Figures 2.5 and 2.7, point 2.6).

Figure 2.8 shows that from points 6 to 7, changes in pressure are small; the pressures at 0.9 m and 1.2 m decrease slightly but at a depth of 1.5 m pressure increases slightly. The temperature shows a marked decrease of about 1^{o}C at all sensors, suggesting heat loss or exchange with cooler water. After that, pressure and temperature from points 7 to 1 decrease and remain close to the boiling curve until the system returns to the initial conditions (close to T_{boil}).

Fluctuations in pressure from points 3 to 7 (Figure 2.3, 2.6, and 2.8) are coincident with T_{boil} at a depth of 0.6 m (Figure 2.7c). Considering the uncertainties in the temperature, there is no clear evidence of superheated fluid; if superheated fluid is present (points that are to the right of the boiling curve in Figure 2.8), superheating is not sustained in time.

2.6 Discussion

2.6.1 Modulation of the IBE

An important observation made at El Jefe was the consistent timing and evolution of the eruptions (at least within the week of measurements) despite the fact that a large amount of the erupted water cools at the surface and recharges the geyser system. Lengthening of geyser IBE, as a result of decreases in the air temperature, has been reported in pool geysers (Hurwitz et al., 2014, Merzhanov et al., 1990). This lengthening occurs because the large surface area of pool geysers enhances heat loss to the surroundings; thus, IBE increases as air temperature decreases and wind speed increases (Hurwitz et al., 2014). The extremely regular IBE and very weak correlation between the IBE and air temperature ($r^2 = 0.01$) suggest that there is no significant influence of air temperature on the geyser cycle. The constant value of IBE also implies that large variations in wind speed and hence evaporation (which we did not measure) may have negligible influence.

Stresses induced by barometric pressure changes (3×10^2 Pa) and solid Earth tides (10^3 Pa) can potentially produce poroelastic perturbations in the conduit and/or reservoir that interfere with bubble nucleation and growth, or change permeability, hence changing

the time to reach critical conditions for an eruption (Hutchinson et al., 1997; Vandemeulebrouck et al., 2013). Although one week of data may not be enough to establish a clear correlation, El Jefe Geyser does not show variation of the IBE related to external stress changes, consistent with measurements at geysers at Yellowstone (Hurwitz et al., 2014; White and Marler, 1972; Rojstaczer et al., 2003). Pressure perturbations greater than 3 x10^2 Pa may thus be required to affect the IBE of El Jefe.

The regularity of El Jefe's IBE and the weak modulation of its IBE by external conditions suggest that the behavior of some geysers is dominated by internal processes (Bloss and Barth, 1949; Marler, 1951; Rojstaczer et al., 2003; Hurwitz et al, 2014). The geometry and thermodynamic state of the reservoir and/or deeper conduit must dominate the periodicity of El Jefe geyser. The insensitivity to changes in ambient temperature implies that the erupted volume is smaller than the subsurface reservoir, or the amount of cooled water that flows back into the conduit is not significant compared with hotter water coming from below.

2.6.2 Duration of the eruption and the quiescent period

Steinberg et al. (1982) and Shteinberg (1999) developed a model to explain a relationship between the quiescent period and the duration of the previous eruption in which heat and water are provided by two sources: a cold reservoir with recharge controlled by pressure in the conduit, and a hot reservoir with a constant recharge to the system. A longer eruption would remove more heat and mass from the system, and thus the time needed for the next eruption would increase. In contrast, IBE shows no real variation, and we observed that the duration of an eruption and its subsequent quiescent period have a weak negative relationship (Figure 2.9, a), though the correlation coefficient is small and the distribution is nearly uniform (Figure 2.3b-d). The length of quiescent period before the eruption and the IBE are unrelated with the eruption duration (Figure 2.9: b, c). Temperature data do not indicate that accumulating heat is transferred to the near-surface conduit during the quiescent period, but rather, temperature is almost constant, suggesting that a single reservoir dominates recharge to the conduit. The addition of heat occurs at the end of recharge, which we attribute to steam coming from below over a short time interval, not at a constant rate.

2.6.3 Eruption stages

We apply idealized models to interpret pressure and temperature measurements, with the objective of constraining or inferring key processes and properties: the recharge from the reservoir into the conduit; hydrogeologic parameters of the conduit; steam mass fraction before and during the eruption; sound speed; and the possibility of choked flow at the vent.

Previous authors (e.g., Kieffer, 1984; Karlstrom et al., 2013, Namiki et al., 2014;

Adelstein et al., 2014) described a preparation stage preceding major eruptions called "pre-play", which is characterized by pulses of liquid and/or steam discharge. At El Jefe we also document a preparatory phase in the form of the oscillations preceding every eruption, but without surface discharge.

1.1.1.6. Recharge of the conduit

During the quiescent period, water level changes by ~0.25 m. The equivalent radius of a cylinder with volume >110 liters (our estimate of erupted volume) is >0.38 m, greater than the dimensions seen by the video camera (r < 0.15 m), implying that cavities and fractures imaged by the video camera that intersect the conduit (Figure 2.2) contain water that erupts.

Estimated mean net mass flow of 0.83 kg/s for El Jefe is similar to the estimate of 0.68 kg/s made at Old Faithful Geyser of Calistoga, California, USA (Rudolph et al., 2012). The mass flow rate is smaller than at Lone Star geyser in Yellowstone National Park, 1.9 kg/s (Karlstrom et al., 2013), and Old Faithful, 7.0 - 8.3 kg/s, using a measured discharge of 38 - 45 m^3 (Allen and Day, 1935).

We define the beginning of each cycle by the initiation of recharge of the conduit as documented by an increase in pressure (points 1 to 3). The rate of pressure increase decays exponentially during most of the refilling period (Figure 2.11d) and it is similar to models and measurements at other geysers (e.g., Steinberg et al., 1982; Kedar et al., 1998; Rudolph et al., 2012; Shteinberg et al., 2013). The water level in the conduit $Z_c(t)$, increases from the initial value Z_0 owing to the recharge of water. Taking the base of the conduit as a reference, the total water level $Z(t)$ increases (Figure 2.10) as

$$Z(t) = Z_c(t) + Z_0 \quad . \qquad (1)$$

The mass flow rate during the recharge of the conduit $G(t)$, assuming a constant water density (ρ) and a constant cross section of the conduit (S), changes the water level (Figure 2.10):

$$G(t) = \rho S \frac{dZ(t)}{dt} \quad . \qquad (2)$$

Even though we observe that the conduit width varies with depth, we assume that it is constant to simplify the equations.

Total pressure inside the conduit during the recharge, $P(t)$, can be determined assuming that it is close to hydrostatic conditions, i.e., $P(Z,t) = \rho g Z\,(t)$, with g being the gravitational acceleration.

Following previous approaches (Steinberg et al., 1982; Kedar et al., 1998; Rudolph et al., 2012; Shteinberg et al., 2013), we assume that recharge $G(t)$ into the conduit is linearly proportional to the pressure difference between the reservoir (P_∞) and the conduit (Figure 2.9),

$$G(t) = -\alpha\,(P(t) - P_\infty\,). \qquad (3)$$

This expression is analogous to Darcy's law if we neglect pressure diffusion in the system providing the recharge. By analogy to Darcy's law, the constant of proportionality, α, depends on the hydraulic conductivity *K*, the distance *L* to the reservoir, and the surface area, *A*, over which recharge occurs. Here, *A* is again assumed to be constant, and not dependent on water level. The constant α in equation (3) can be related to equivalent quantities in previous models (Steinberg et al., 1982; Kedar et al., 1998, Rudolph et al., 2012): $\alpha = \alpha_{Steinberg} = S\rho / \alpha_{Kedar} = \alpha_{Rudoph}/\rho$).

From equations (2) and (3), we obtain

$$\left(\frac{S}{g}\right)\frac{dP(t)}{dt} = -\alpha\,(P(t) - P_\infty). \qquad (4)$$

Integrating, and applying the initial condition P_0 at t = 0

$$P(t) = P_\infty + (P_0 - P_\infty)(e^{\frac{-t\alpha g}{S}}) \quad . \qquad (5)$$

The pressure measured at the sensor $P_{sen}(t)$ is related to the total pressure by

$$P_{sen}(t) = P(t) - P_{0\_in} \qquad (6)$$

where P_{0_in} is the difference of hydrostatic pressure between the reservoir and the sensor (Figure 2.10)

$$P_{sen}(t) = (P_\infty - P_{0\_in}) - (P_\infty - P_0)(e^{\frac{-t\alpha g}{S}}) \quad . (7)$$

Fitting the data from the sensor located at a depth of 1.5 m with equation (7), from points 1 to 2, we obtain

$$\left(P_\infty - P_{0_{in}}\right) = 6.97 \times 10^4 \pm 4 \times 10^2 \text{ Pa} \qquad (8)$$

$$(P_\infty - P_0) = 2.10 \times 10^3 \pm 2 \times 10^2 \text{ Pa} \qquad (9)$$

$$\frac{S}{\alpha g} = 43.00 \pm 4 \text{ s} \qquad (10)$$

Considering that $P_0 = P_{0\_sen} + P_{0\_in}$, from (8) and (9) we obtain

$$P_{0\_sen} = 6.76 \times 10^4 \pm 1 \times 10^2 \text{ Pa} \qquad (11)$$

The reasonable fit between the observed and modeled pressure suggest that recharge is dominated by the water level in the conduit. However, toward the end of recharge (Figure 2.11, points 2 to 3), the rate of pressure increase is greater than predicted by the model and deviates from the exponential fit. This misfit may be the result of the decrease in diameter of the upper conduit. Additionally, we calculated the exponential fit between points 2 and 3. Using equation 10, the new fitting (considering the same αg), we infer that the surface area between points 1 and 2 is 4.5 times greater than the surface area between points 2 and 3. By the end of the recharge period, water reaches the upper conduit where the radius was ~0.15 m, whereas the lower conduit is estimated to be ~0.32 m. From the total erupted volume, the equivalent radius was estimated to be ~0.38m. Assuming *S* for a conduit of constant radius (*r* ~ 0.38 m) (Figure 2.10), from equation (10) we calculate

$$\alpha = 3.40 \times 10^{-4} \quad . (12)$$

If we treat the rock around the conduit as a porous medium, the volumetric flow $Q(t)$ is given by

$$Q(t) = -K\frac{A}{L}(Z(t) - Z_0) \quad . \quad (13)$$

Then, equation (4) is written as

$$Q(t) = -g\alpha(Z(t) - Z_0) \quad (14)$$

$$\alpha = -\frac{K}{g}\left(\frac{A}{L}\right) \quad (15)$$

We can estimate the ratio $\frac{A}{L}$ as a function of permeability, $k = K\mu/\rho g$. If the recharging system has k >10^{-9} m^2, $\frac{A}{L}$< 0.1 m (using a viscosity of 0.335 x 10^{-3} Pas at T_{boil}), which implies a thin and long fracture. If k <10^{-11} m^2, $\frac{A}{L}$> 12 m, and a much thicker region provides recharge.

Previous models considering two sources of water suggested that hot water from below provides a constant heat input (Steinberg 1982; Kedar et al., 1998). Those models predict an exponential increase of temperature in the conduit during the recharge. To test those models, we consider a constant heat input $H(t)$ of liquid water coming from below with mass flow rate in the conduit $G = \frac{dM(t)}{dt}$, where M is the mass

$$H(t) = C_P\, G(t)\, (T(t) - T_0) \quad (16)$$

If the initial temperature (T_0) is constant

$$T(t) = T_0 + \frac{H(t)}{G(t)\, C_P} \quad . \quad (17)$$

From equations (3) and (7) we obtain the total mass flow $G(t) = G_0(e^{\frac{-t\alpha g}{s}})$, and with $H(t) = H$,

$$T(t) = T_0 + \frac{H}{(G_0 C_P)}\, e^{\frac{t\alpha g}{s}} \quad . (18)$$

Fitting an exponential curve to the temperature data (Figure 2.11e):

$$\frac{H}{(G_0 C_P)} = 0.014 \pm 0.003 \ ℃ \quad (19)$$

$$\frac{s}{\alpha g} = 20 \pm 5.2 \text{ s} \quad . (20)$$

The constant given in equation (20) is different from the equivalent one obtained from pressure data in equation (10). Temperature at a depth of 1.5 m is nearly constant, and increases only towards the end of the recharge period (Figure 2.11c). It is this increase that drives the fit in equation (18). We propose next that the discrepancy between the two

values implies that heat input is not constant, and that there is an additional source of heat provided by steam during the later stages of recharge.

1.1.1.7. Pre-eruptive pressure signal

The pressure difference between the sensors at 0.9 and 1.2 m between the beginning (point 1) and the end of the recharge period (point 3) decreases by 2.5 x10^2 Pa. This decrease implies that some liquid water is replaced by steam. Assuming that initially the conduit had only liquid water with a density of ~970 kg/m^3, by the end of recharge the density decrease is ~80 kg/m^3. This value would arise if ~ 8 volume % of the liquid is replaced by vapor, equivalent to a steam mass fraction of ~ 5x10^{-5}.

We observe a water pressure signal with a period of 1 to 2 s during a geyser cycle (Figure 2.12). One possible source of such periodic signals is resonance within the geyser conduit. Periodic signals were documented at other geysers (e.g. Kieffer, 1984; Lu and Kieffer, 2009) and seismic tremor is widely documented at magmatic volcanoes (e.g., Chouet, 1992; Johnson and Ripepe, 2011; Denlinger and Moran, 2014).

Resonance and damping of the perturbations are controlled by the geometry of the conduit, and the sound speed in the fluid U. In a pipe closed at one end, resonant frequencies f of a water column with height Z are (e.g., Kinsler et al., 1982)

$$f = \frac{nU}{4Z}, \quad (21)$$

where n is the mode (odd integer values, with n=1 being the fundamental mode and higher values being overtones), and we assume U constant. The equilibrium sound speed of water+steam mixtures with a vapor mass fraction of 5x10^{-5} is U~1 m/s (the non-equilibrium sound speed is >40 m/s; Karlstrom et al., 2013). The fundamental mode for a water column height of 0.85 m (approximate water level from the bottom of the conduit before eruption) is then ~3.4 s (0.3 Hz). Our estimate is highly uncertain (the mass steam fraction is uncertain and is not likely to be uniform inside the conduit), and the value only differs by a factor of 2 to 3 from the 0.5 to 1 Hz signal that we see. We do not favor a resonance origin, however, because we do not see any overtones, nor any frequency gliding that might arise from temporal changes in steam mass fraction or water depth. Kedar et al. (1998) did not find evidence for conduit resonance at Old Faithful, Yellowstone either.

A second possible source of the oscillations is bubbles of steam or warm water entering the conduit from below every 1-2 s. Cross-correlation of the pressure measurements (Figure 2.13) shows no time lag suggesting that all sensors are recording oscillations in the height of the water column. Several models of geysers describe "bubble traps" or cavities at depth, which are connected to the conduit and allow steam to accumulate and then be released into the geyser conduit (Mackenzie, 1811, Hutchinson et al., 1997; Belousov et al., 2013; Vandemeulebrouck et al., 2013; Adelstein et al., 2014). El Jefe's upper conduit ends at depth in a narrow crack, which may be connected to a

similar bubble trap. A slug of steam passing through the crack can increase the water level in the conduit (Kedar et al., 1998). Increasing the elevation of the water column by injecting steam may explain the faster increase in pressure at the end of the recharge, ~ 10 s before the eruption (Figure 2.11d). We visually observed a rapid increase of water level seconds before the eruption begins (down-hole video: electronic supplementary material Munoz-Saez et al., 2015a).

1.1.1.8. Eruption

Water below the air-water interface is near boiling temperatures during the entire cycle. An additional input of heat into the system increases the water temperature, and a large mass of water boils in the upper conduit (Figure 2.7c, point 3 to 4). Once the eruption begins, we see large pressure fluctuations, similar to those attributed by Kedar et al. (1998) to boiling and bubble collapse. The volume expansion of water when it boils will increase the pressure above the liquid surface and hence increase pressure at greater depths as well.

Once an explosive eruption begins at the surface, water is removed from the conduit (Figure 2.5 and 7 points 3 to 6), and the fluid in the conduit decompresses (Figure 2.8 points 4 to 6). Boiling conditions propagate downward (Figure 2.8 points 5 to 6). By the time the system at depth reaches the maximum temperature, the eruption of water ends at the surface (Figure 2.5 and 2.8, point 6). Temperature decreases at depth (Figure 2.8 points 6 to 7), suggesting that heat is lost, however boiling continues in the upper part of the water column because pressure continues to decrease (points 6 to 7 in figures 2.7c and 2.8a). However, in the deeper part of the conduit (Figure 2.8c) there is a slight increase of pressure that can be explained by lesser amounts of steam at depth. These observations suggest a non-uniform distribution of steam through the conduit. Water at depth stays below the boiling curve (Figure 2.8, points 6 to 7c). Refilling by erupted water cools the conduit and ends the cycle (Figure 2.7c, points 7 to 1).

Boiling conditions alone are not sufficient to cause an explosive eruption as boiling conditions persist after the eruption ends. The addition of steam from below the conduit, combined with a small enough volume of the cavity above the boiling surface, may be necessary to create pressures from boiling sufficient to initiate and sustain the eruption.

We performed a moving-window cross-correlation between pressure fluctuations recorded at different depths during the eruption. We find that pressure fluctuations propagate upward with a speed of 3 to 4 m/s (Figure 2.13). This measured speed is the sum of the upward propagation velocity of pressure waves and upward velocity of the fluid in the conduit. Speeds of a few m/s would empty the conduit very rapidly, so we assume that at depth the propagation speed is close to 3-4 m/s. Using the model for the sound speed of liquid+steam mixtures under conditions of thermodynamic equilibrium (Kieffer, 1984; Lu and Kieffer, 2009), the implied steam mass fraction during the

eruption is of the order of 1.2 x10^{-3} (U = 3 m/s) to 1.7 x10^{-3} (U = 4 m/s), using the formulation presented in Karlstrom et al. (2013); the equivalent volume fraction of steam is between 0.75 to 0.80 (using steam density of 0.4 kg/m^3 and liquid water density of 970 kg/m^3 for P_{air} and T_{boil}). These values suggest that the steam mass fraction during the eruption is two orders of magnitude higher than the amount of steam present in the conduit during recharge (inferred from the pressure changes described in the previous section).

The exit velocity v of the steam+liquid mixture can be estimated from the eruption height h by converting kinetic energy to potential energy, $v = \sqrt{2gh}$. The value of h varies during the eruption; using FLIR images and video recording we estimated the maximum h < 2 m (Figure 2.5), thus v < 6 m/s. This value is higher than, but still close to, the sound speed inferred from propagating pressure signals, suggesting that the flow may in fact be choked to the equilibrium sound speed at the vent. However, uncertainties on the mass fraction of steam are too large to make this inference robust. Considering v and the size of the geyser mouth (r~0.15 m), the exiting volume flux of liquid-steam mixture is 0.42 m^3/s, which is 3 orders of magnitude higher than discharge of liquid water measured at the surface.

During the eruption, the temperature at depth increases by ~ 3^{o}C (Figure 2.7, point 3 to 4). We calculated the heat added to the system that is needed to increase the temperature of the column water by 3^{o}C. Considering an average mass of the erupted water of >110 kg, we obtain ~1.4 x10^6 kJ, using $H_{erupted} = C_p mT$, and C_p=4.2 kJ/kg^{o}C. The amount of vapor condensation needed to heat this water is ~0.52 kg, using a latent heat of 2660 kJ/kg (for P_{air} and T_{boil}). The implied volume of steam required is ~1.24 m^3 (steam density 0.4 kg/m^3), equivalent to a cavity ~1 m in diameter. ~0.52 kg of steam in 110 kg of water is equivalent to a steam mass fraction of 4.7 x 10^{-3}, consistent with the previous estimates given the large uncertainty associated with the inferred sound speed (again, using the equilibrium sound speed).

The tilt data are noisy and likely influenced by the ponding and flow of water at the surface. However, when the tilt data are stacked, we do see a correlation with pressure in the conduit (Figure 2.6ab). At El Jefe we see deformation, as recorded by the tilt that tracks the pressure in the conduit. Large increases of the tilt occur at the beginning of the eruption. In contrast, previous studies of geysering wells documented rapid decrease of the tilt during the eruption and gradual recovery during the quiescent period associated with recharge of water (Nishimura et al., 2006, Rudolph et al., 2012). The nature of the conduit may explain the difference: the previous studies were conducted at the Onikobe geyser, Japan and Old Faithful Geyser of Calistoga, California, which are artificial geysers whose conduits are metal pipes that isolate processes within the conduit from ground deformation.

1.1.1.9. Relaxation

At the end of the eruption, the large amplitude pressure fluctuations end. Boiling ends, and colder erupted water enters the conduit. Pressure and temperature smoothly decrease until the cycle starts again.

1.1.1.10. Conceptual model

Figure 2.14 illustrates the conceptual model for all the key stages in the geyser cycle:

- Recharge: A single reservoir dominates recharge to the conduit. The pressure P_∞ in the reservoir is constant, and exceeds the pressure inside the conduit $P(t)$. The temperature of the reservoir is constant, T_∞. The filling process is adiabatic, and reaches boiling conditions at the top of the water column $T(t) \sim T_{boil}$. The rate of recharge $G(t)$ and pressure increase $P(t)$ inside the conduit decrease over time. Pressure in the conduit is close to hydrostatic and depends on the water level.
- Pre-eruptive stage: At the end of the recharge, steam bubbles from below (bubble trap) add latent heat to the system. $P(t)$ and $T(t)$ increase rapidly, and initiate explosive boiling at the top of the conduit.
- Eruption: During the eruption there is explosive discharge of water at the surface driven by rapid expansion of steam. The eruption column increases in height. Boiling conditions propagate downward in the conduit, as pressure decreases and temperature reaches a maximum value. The eruption at the surface ends but the column of water in the conduit is still at boiling conditions. Cooler erupted water enters the conduit, cooling the top of the water column (Figure 2.7c). Large amplitude pressure fluctuations are caused by some combination of boiling, cavitation, and bursting of steam bubbles at the liquid surface.
- Relaxation: Once the eruption stops, temperature and pressure inside the conduit continue decreasing, remaining close to the boiling curve until initial conditions are restored.

2.7 Conclusions

Our work at El Jefe Geyser provides a unique dataset, with a complete record of pressure and temperature inside a geyser conduit during complete geyser cycles over a large number of eruptions. We document the different stages of the geyser cycle, we calculate the fluid properties during an eruption, and we infer thermodynamic conditions at depth. Rapid boiling of a large mass of water occurs at the top of the water column.

Water is then removed from the conduit and the remaining water decompresses, causing the boiling front to propagate downward. Eruption terminates when the addition of steam has ceased.

In the introduction we highlighted a few outstanding questions that our measurements allow us to address:

- How is heat transported? Steam ascending from depth provides thermal energy used in boiling during the eruption at El Jefe geyser. A small mass fraction of steam (order of ~10^{-3}) is enough to produce an eruption. We infer sound speeds for liquid+steam mixtures between 3 to 5 m/s. There is a possibility that flow may be choked at the vent, but uncertainties are too large to be conclusive.
- What is the geometry of the subsurface and its role? The dynamics of the eruptions are dominated by geometrical and thermodynamic complexities in the conduit and reservoir system below the near-surface conduit, allowing the accumulation and periodic release of steam in a reservoir that acts as a "bubble trap".
- How do geysers respond to external influences? Data do not show modulation of the interval between eruption (IBE) by external perturbations, implying an internal control on the geyser cycle. It also suggests that the thermal reservoir is very large relative to the amount of water erupted for this geyser.

El Jefe Geyser had an extremely regular eruptive cycle at least during the week it was monitored, which contradicts the long-standing legend that the El Tatio geysers erupt when the sun rises.

2.8 Acknowledgments

This research was supported by National Science Foundation, and CEGA, University of Chile. We thank El Tatio team who provided essential help in the laboratory and in the field: Fred Murphy, Ameeta Patel, Angello Negri, Pablo Ortega, Alberto Ardid, Cyndi Kelly, Sarah Barrett. Eric King built the video camera system and took videos in the field. The fieldwork was performed with the permission of the Amayras Communities of Caspana and Toconce. We also thank Professor Lionel Wilson, Editor of Journal of Volcanology and Geothermal Research, the reviewers Dr. Atsushi Toramaru, Dr. Alexander Belousov, and Fred Murphy, internal reviewer for USGS. Any use of trade, firm, or product names is for descriptive purposes only and does not imply endorsement by the U.S. Government.

2.9 Tables and Figures

Table 2.1 Summary of parameters

Parameter	Value	Unit	Description
A	-	m^2	Cross-sectional area of flow of water from the aquifer to the conduit
α	-	m x s	Constant of proportionality between mass flow rate and pressure inside conduit
C_P	-	$\frac{J}{kg\ K}$	Heat capacity of water
f	-	Hz	Frequency of resonance
g	9.8	$\frac{m}{s^2}$	Acceleration of gravity
G_o		$\frac{kg}{s}$	Initial and constant mass flow rate of water coming from hypothesized reservoir or aquifer
$G(t)$	-	$\frac{kg}{s}$	Total mass flow rate of water during the recharge
h	-	m	Height of the eruptive column
$H(t)$	-	$\frac{J}{s}$	Heating rate during the recharge calculated from model
$H_{erupted}$	-	J	Heat needed to generate an eruption
k	-	m^2	Permeability of the conduit
K	-	$\frac{m}{s}$	Hydraulic conductivity
L	-	m	Distance over which water flows from the aquifer to the conduit
m	-	kg	Total mass of water erupted
$M(t)$	-	kg	Mass of water in the conduit during recharge
n	1	-	Fundamental mode of resonance
P_{air}	6.07×10^4 to 6.1×10^4	Pa	Atmospheric pressure measured at El Tatio, 4200 m of elevation
P_0	-	Pa	Initial hydrostatic pressure in the conduit
P_{0_in}	-	Pa	Initial hydrostatic pressure inside of the conduit, below the sensor.
P_{0_sen}	-	Pa	Initial hydrostatic pressure inside of the conduit, above the sensor.
$P(t) = P(Z,t)$	-	Pa	Total hydrostatic pressure
$P_c(t)$		Pa	Hydrostatic pressure above Z_0
$P_{sen}(t)$		Pa	Hydrostatic pressure above the sensor

P_∞	-	Pa	Pressure in the hypothesized reservoir
$Q(t)$	-	$\frac{m^3}{s}$	Volumetric flow rate into the conduit
r	0.15 – 0.38	m	Radius of the conduit, assuming a cylindrical shape
ρ	~970	$\frac{kg}{m^3}$	Density of water at T_{boil}
S	-	m^2	Cross section area of the conduit with radius r
t	-	s	Time
T_{air}	-5 to 25	℃	Measured atmospheric temperature
T_{boil}	86.2 - 86.4	℃	Boiling temperature at P_{air}
T_0	-	℃	Initial temperature at the bottom of conduit before recharge
$T(t)$	-	℃	Temperature inside the conduit during the recharge
T_∞	-	℃	Temperature in the hypothesized reservoir or aquifer
U	-	$\frac{m}{s}$	Sound speed of water
v	-	$\frac{m}{s}$	Exit velocity from the conduito the surface
μ	0.335 x 10^{-3}	Pa s	Dynamic viscosity of water at T_{boil}
Z_0		m	Initial water level into the conduit at the beginning of the recharge
Z_{0_in}	-	m	Initial water level into the conduit, below the sensor
Z_{0_sen}		m	Initial water level into the conduit, above the sensor
$Z(t)$	-	m	Water level in the conduit during the recharge
$Z_{sen}(t)$	-	m	Water level into the conduit during the recharge, above the sensor
$Z_c(t)$	-	m	Water level into the conduit during the recharge, above the Z_{0_sen}

Figure 2.1: El Tatio Geyser Field

(a) Map of South America showing the location of El Tatio in Northern Chile. (b) Aerial photograph of El Tatio Geyser Field (GLCF: Earth Science Data Interface); white boxes show the Upper, Middle, and Lower Geyser Basins. In the upper basin, El Jefe Geyser (UTM coordinates 601768 E; 7530174 S, WGS84, 19S) is marked by the white star. The blue line indicates the normal fault that bounds the El Tatio half-graben. El Jefe Geyser is located in the hanging wall of that fault. (c) El Jefe Geyser erupting.

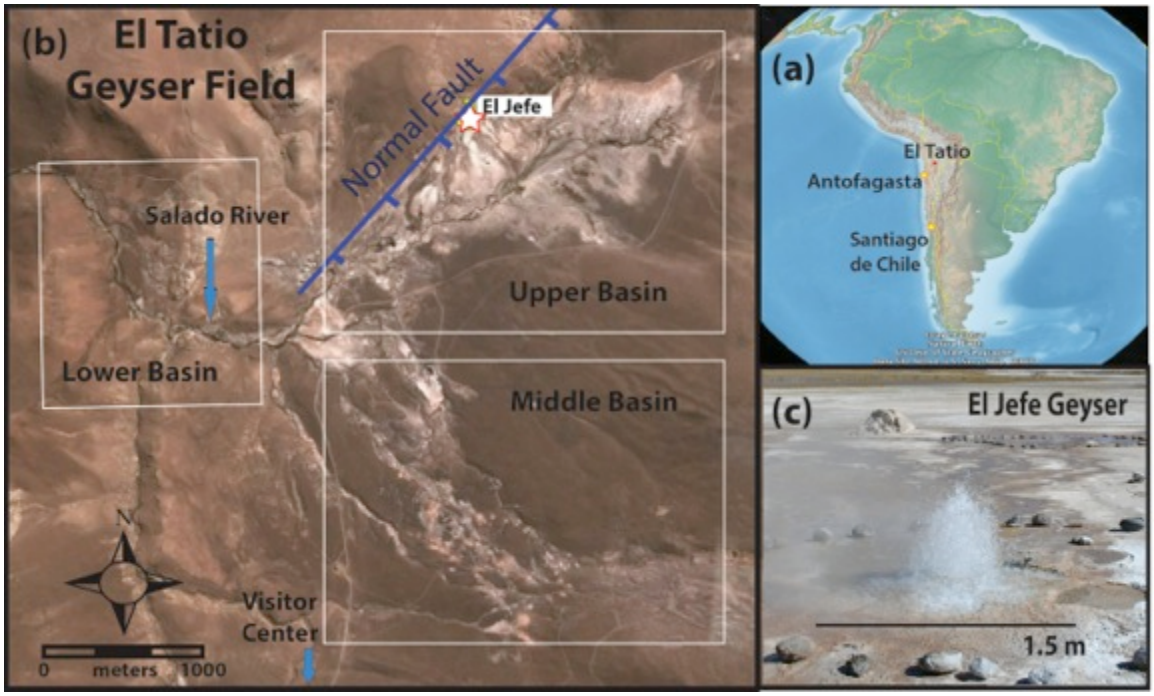

Figure 2.2: Geyser conduit

(a) Illustration of the conduit and the locations of the deployed temperature (T) and pressure (P) sensors. (b) Photograph of the conduit mouth, while the water level was decreasing, showing the string of sensors; distance between the red marks is 30 cm. (c) Photograph of the conduit at the air-water interface (0.6 m) showing the irregular conduit, with constrictions and cracks that intersect the conduit.

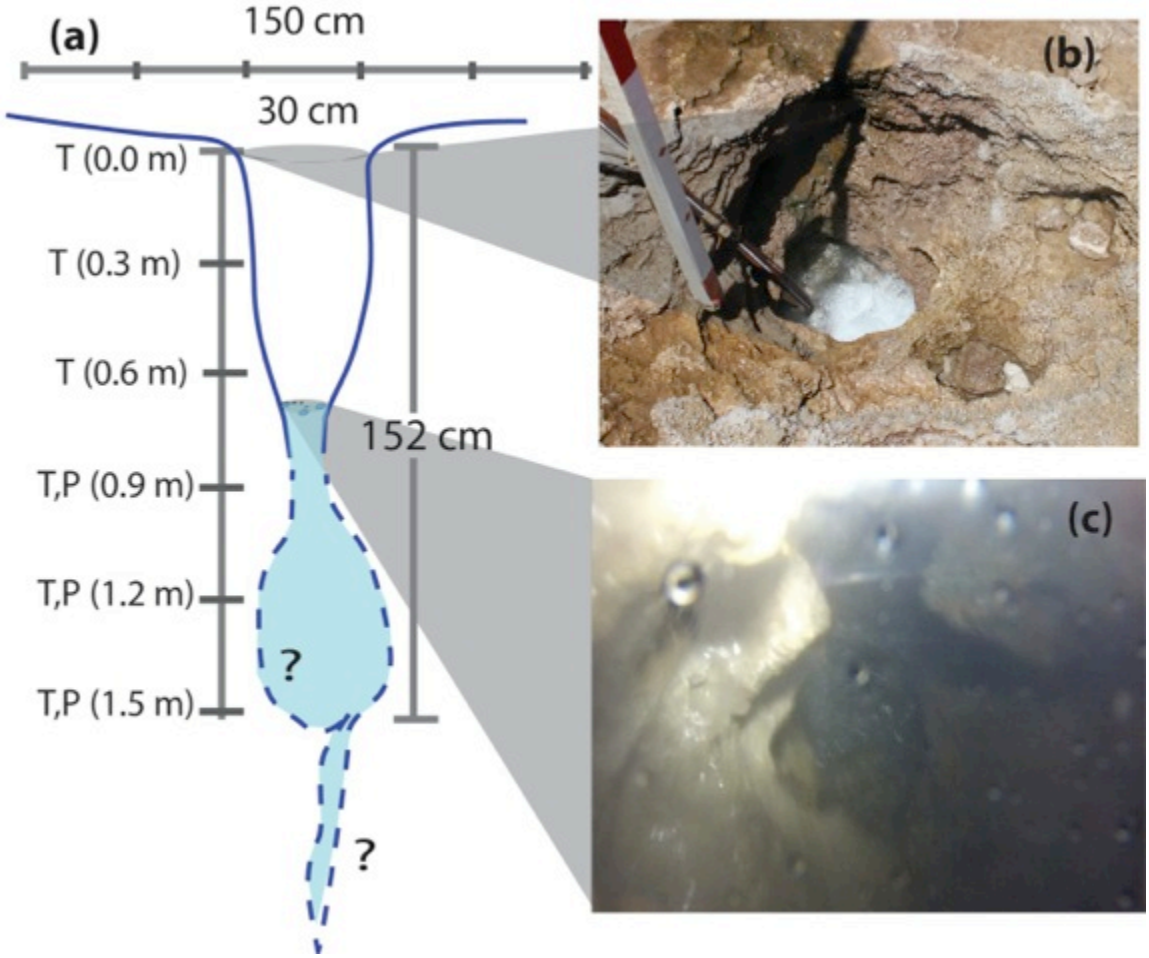

Figure 2.3: IBE and time series of pressure and temperature

a) Pressure and temperature time series for a subset of five eruption cycles, at a depth of 1.5m, on October 20th, 2012. Temperature (red) and pressure (blue) data are plotted on the y–axis, while time is on the x-axis. The box highlights a single cycle. Stars labeled from 1 to 7 identify key stages in the cycle. The green line shows mean boiling temperature (T_{boil} ~ 86.4°C) at average local atmospheric pressure. Lower panel shows histograms of the duration of stages of the eruption cycles: (b) eruption duration (points 3 to 7), (c) quiescent period (including relaxation stage, recharge, and pre-eruptive stage, points 7 to 3), (d) interval between eruptions (IBE)

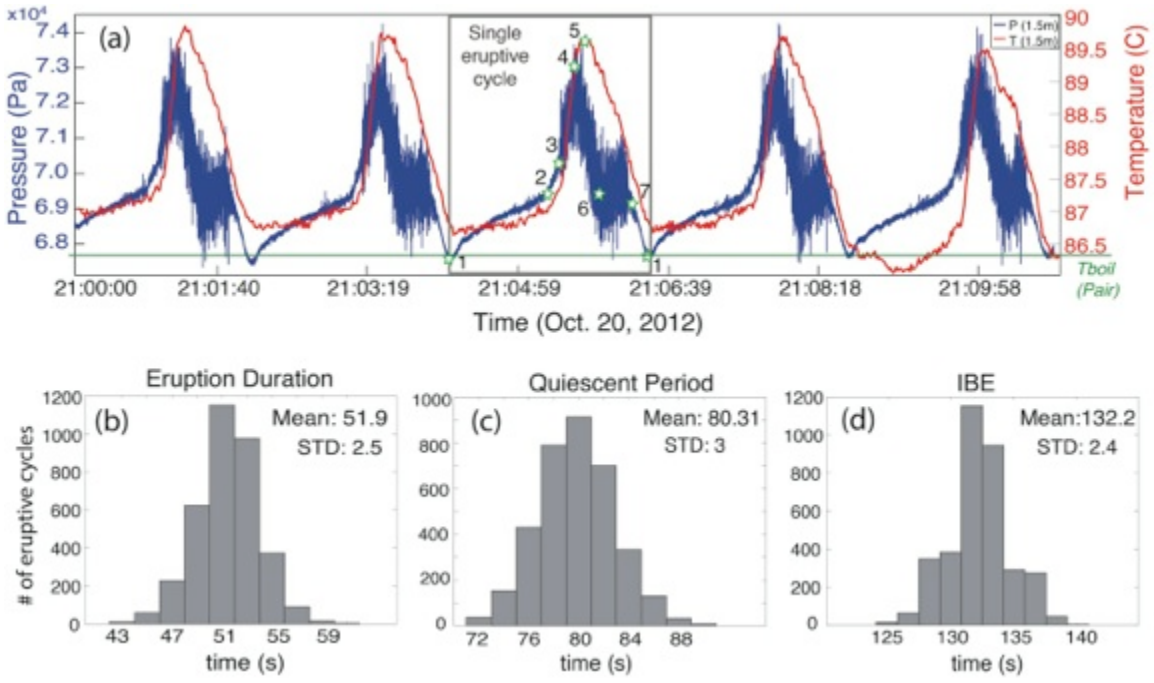

Figure 2.4: Effect of evironmental conditions

(a) Power spectra of pressure (blue) and temperature (red) inside the geyser (1.5m), and external periodic daily signals: air temperature (T_{air}), atmospheric pressure (P_{air}), and solid Earth tides (Tidal). Values on the y-axis were normalized to have the same scale. One-day period observed in the water temperature (1.5 m) data is an instrumental artifact and not a real signal. (b) Time series for 3.5 days showing daily variations of air temperature, atmospheric pressure and solid Earth tides. Values shown on y-axis were normalized ((Value-mean(Value))/Std(Value)). (c) and (d) are 2-D histograms: white dots show the data, and colors show number of dots plotting in that region (color bar). (c) IBE as a function of air temperature, the coefficient of correlation is $r^2 = 0.01$ (d) IBE as a function of atmospheric pressure, the coefficient of correlation is $r^2 = 0.02$.

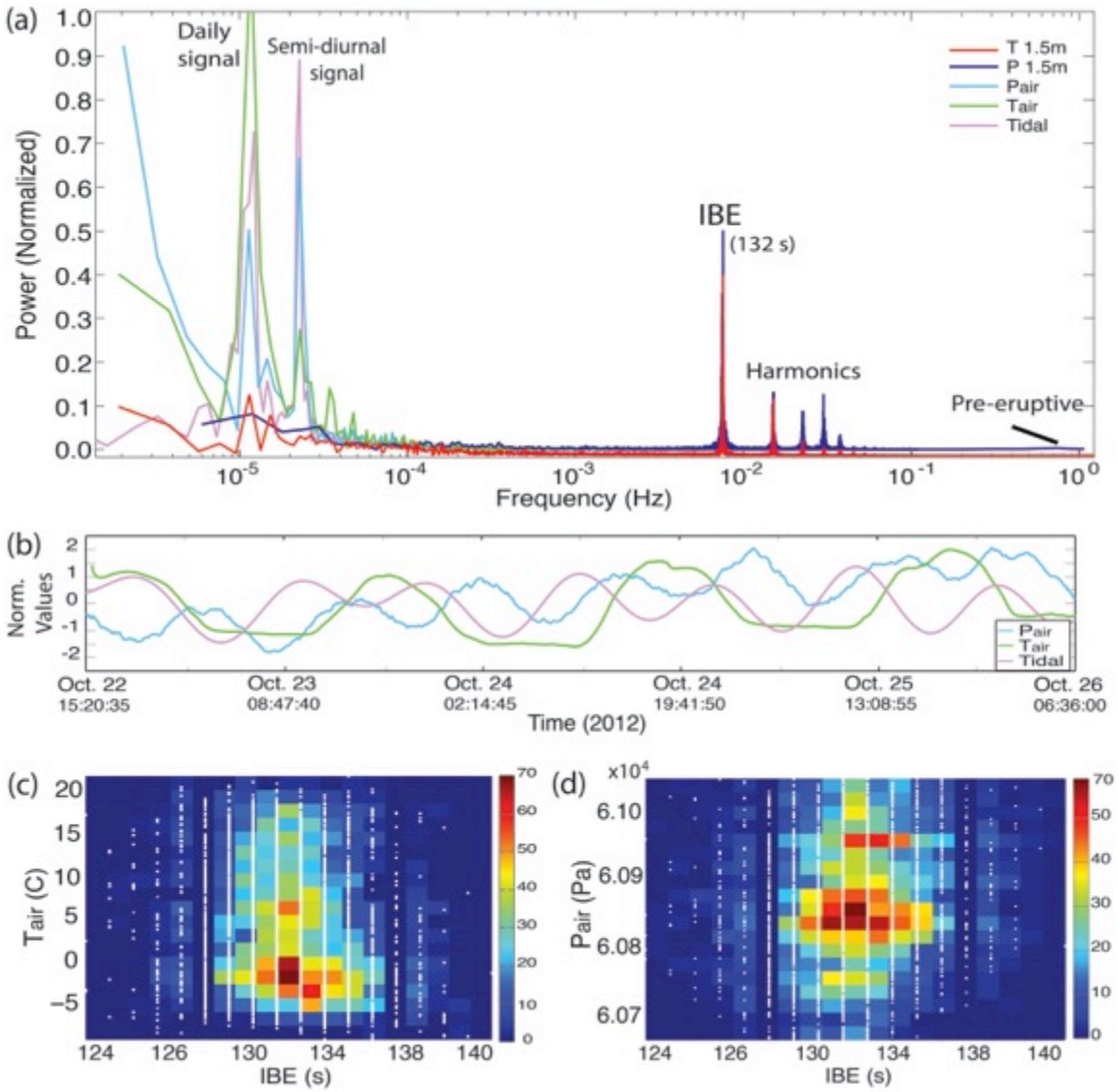

Figure 2.5: Eruption in the surface

(a) A sub-sample of the temperature time series for two sensors at the surface. Every peak represents an eruption. Sensor 1 is located at the geyser mouth. Sensor 2 is located 0.3 m above the conduit mouth. Sensors were in the air before eruptions occur. During the eruption, temperature increased because hot erupted water reached the sensors. (b) Zoom on 35 seconds of a single eruption (box). Stars with numbers are the key stages in the eruption cycle defined in Figure 2.3, but for a different eruption. Images (c) to (g) were taken with a FLIR camera (extracted from the video every ~6 seconds) during the same eruption. High temperature, in red, is related to boiling water coming out of the conduit during the eruption. Image (c) was taken shortly after the start of the eruption at point 3, and it shows the high temperature in the mouth of the conduit. Between points 4 and 6, temperature remains close to T_{boil}, the boiling point; subsequent images (d), (e), and (f) show a high volume of hot water coming out of the conduit. At point 6, temperature decreases (sensor in contact with air). The volume of hot water drops (image (g)) identifying the end of the eruption at the surface.

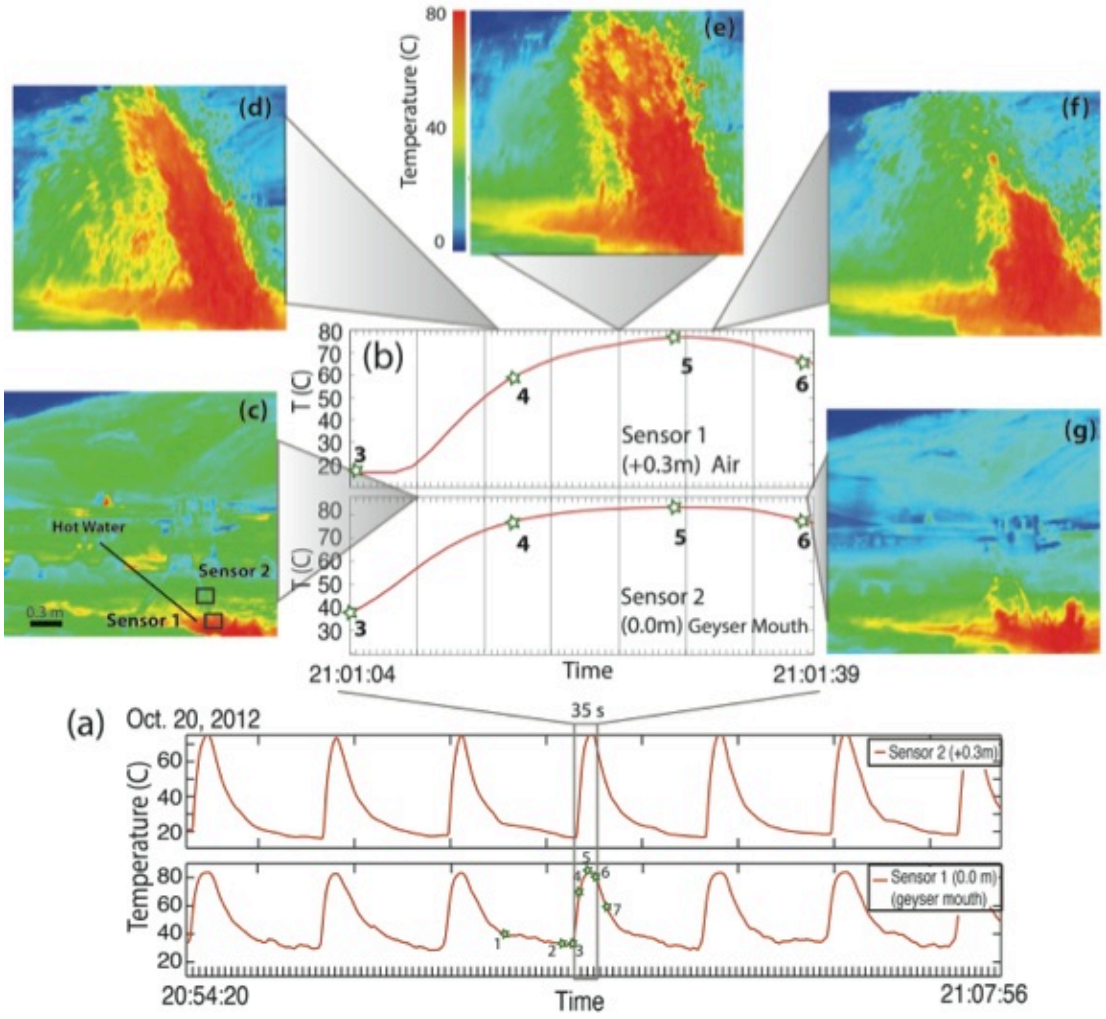

Figure 2.6: Ground deformation

(a) The pressure measured at depths of 1.5 m (dark blue) and 0.9 m (light blue). (b) and (c) show the ground deformation recorded by a tiltmeter, in the radial and tangential directions, respectively. A positive sign indicates that the ground rises in the direction of vent and to the north, respectively. Black curves are the averaged signals. Yellowish to bluish curves are for individual eruptions

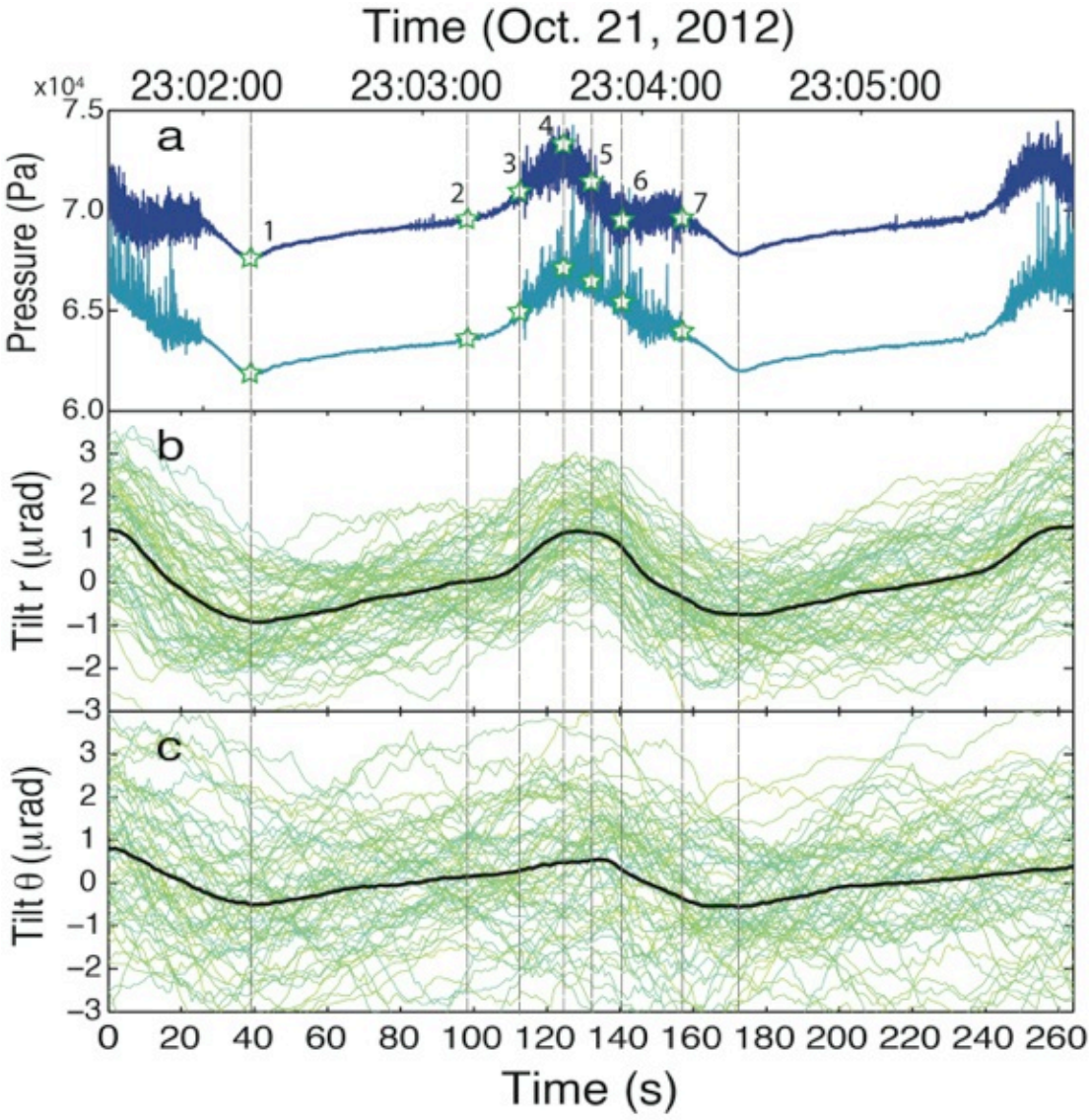

Figure 2.7: Temperature in the shallowest part of the conduit
Record of 3,531 geyser cycles at depths of: (a) 0.0 m, (b) 0.3 m, and (c) 0.6 m. The geyser cycles (red curves) are stacked and averaged (black curves). Range of time is the IBE (132 s). The green line shows the boiling temperature (T_{boil}) for the corresponding air pressure (P_{air}). From points 2 to 3, the temperature increases. After point 3, water reaches the boiling curve at 0.6 m, and the eruption starts. Between points 4 and 5, boiling water reaches the shallowest sensors at 0.3 m and 0.0 m. Between points 6 and 7, water continues to boil at 0.6 m, but boiling water does not reach the shallowest sensors and the eruption ends at the surface. At point 1, cooled erupted water returns to the conduit and the cycle starts again.

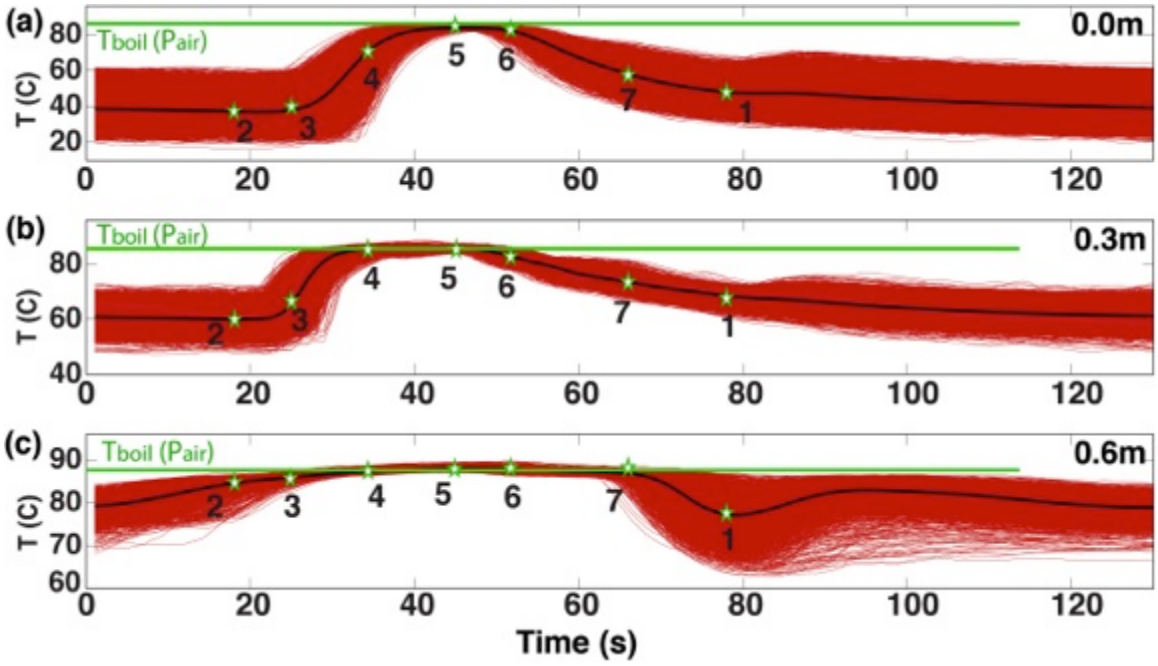

Figure 2.8: P,T cycle

Water pressure and temperature during the eruption cycles, for ~3,531 eruptions. Gray arrows show the evolution of pressure and temperature with respect to time (stars 1 through 7: $t_1 = 0$ s, $t_2 = 65 \pm 2s$, $t_3 = 70 \pm 2s$, $t_4 = 85 \pm 2s$, $t_5 = 100 \pm 2s$, $t_6 = 105 \pm 2s$, $t_7 = 120 \pm 2s$). Black curves show the average and the black bars show the standard deviation of the data. Green lines show the calculated boiling curve for pure water.

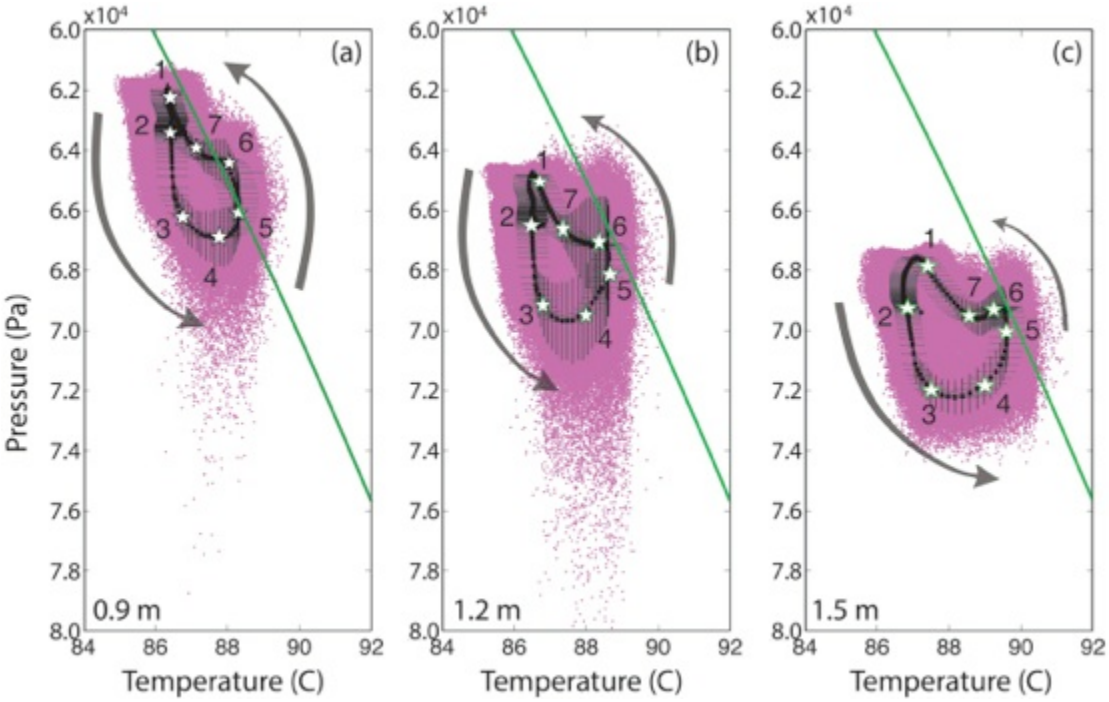

Figure 2.9: IBE relationships

2-D histograms of (a) relationship between eruption duration and duration of following quiescent period, the coefficient of correlation is $r^2 = 0.4$; (b) relationship between eruption duration and duration of previous quiescent period, the coefficient of correlation is $r^2 = 0.03$ (c) Relationship between eruption duration and IBE, the coefficient of correlation is $r^2 = 0.06$. IBE is defined for an entire geyser cycle: the period between the beginning of an eruption and the beginning of the next eruption (eruption duration plus the quiescent period after eruption). White dots show the data, and colors show number of observations plotting in that region (color bar).

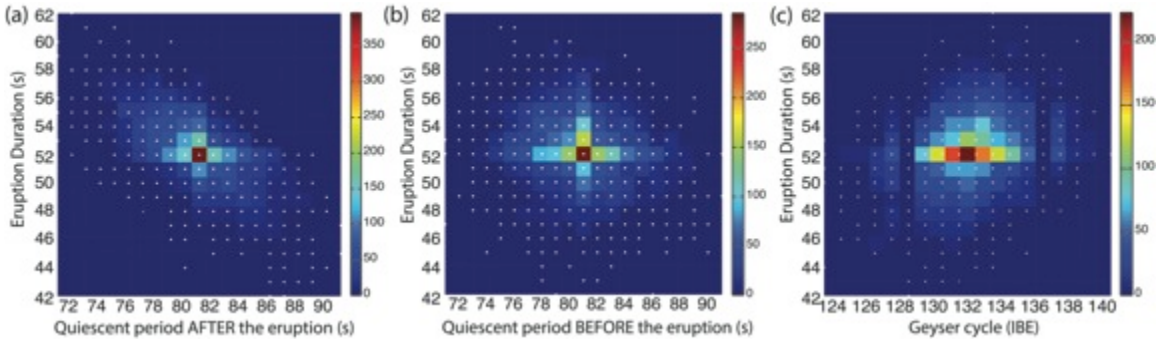

Figure 2.10: Geyser Model

Schematic illustration of the geyser subsurface showing parameters used in the recharge model.

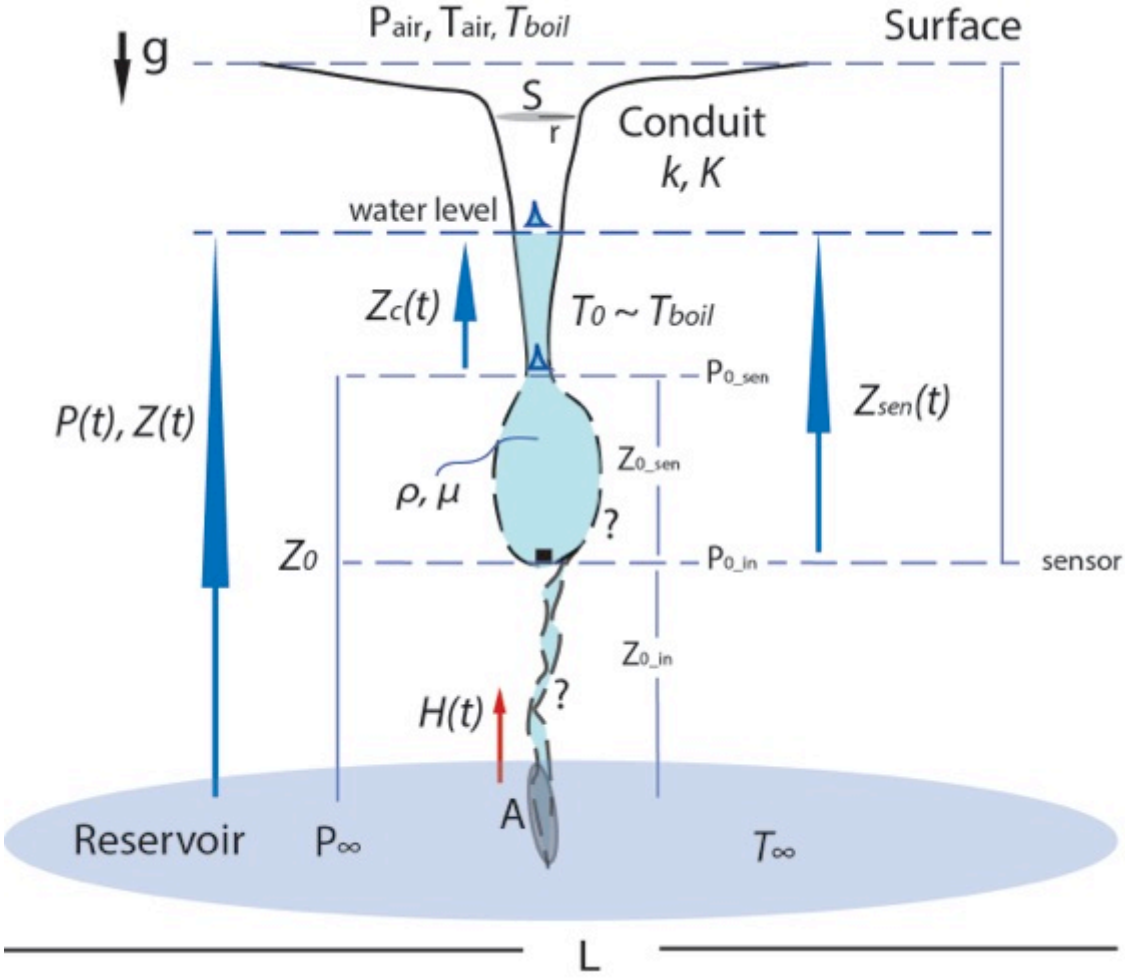

Figure 2.11: Recharge

Data from sensors located at (a) 0.9 m, (b) 1.2 m, and (c) 1.5 m. Pressure (blue) and temperature (red) data on the y-axes, and time for a single eruption cycle on the x-axis. Green line shows the boiling temperature at atmospheric conditions T_{boil} (86.4°C). Numbers 1, 2 and 3 are the same key points described in previous figures. (d) Shows the pressure during the resting time. Fitting curves of the data are the black lines, and vertical gray lines show ±1 standard deviation. (e) Temperature during the same period. Fitting curves are the black lines, and the red vertical lines show ±1 standard deviation.

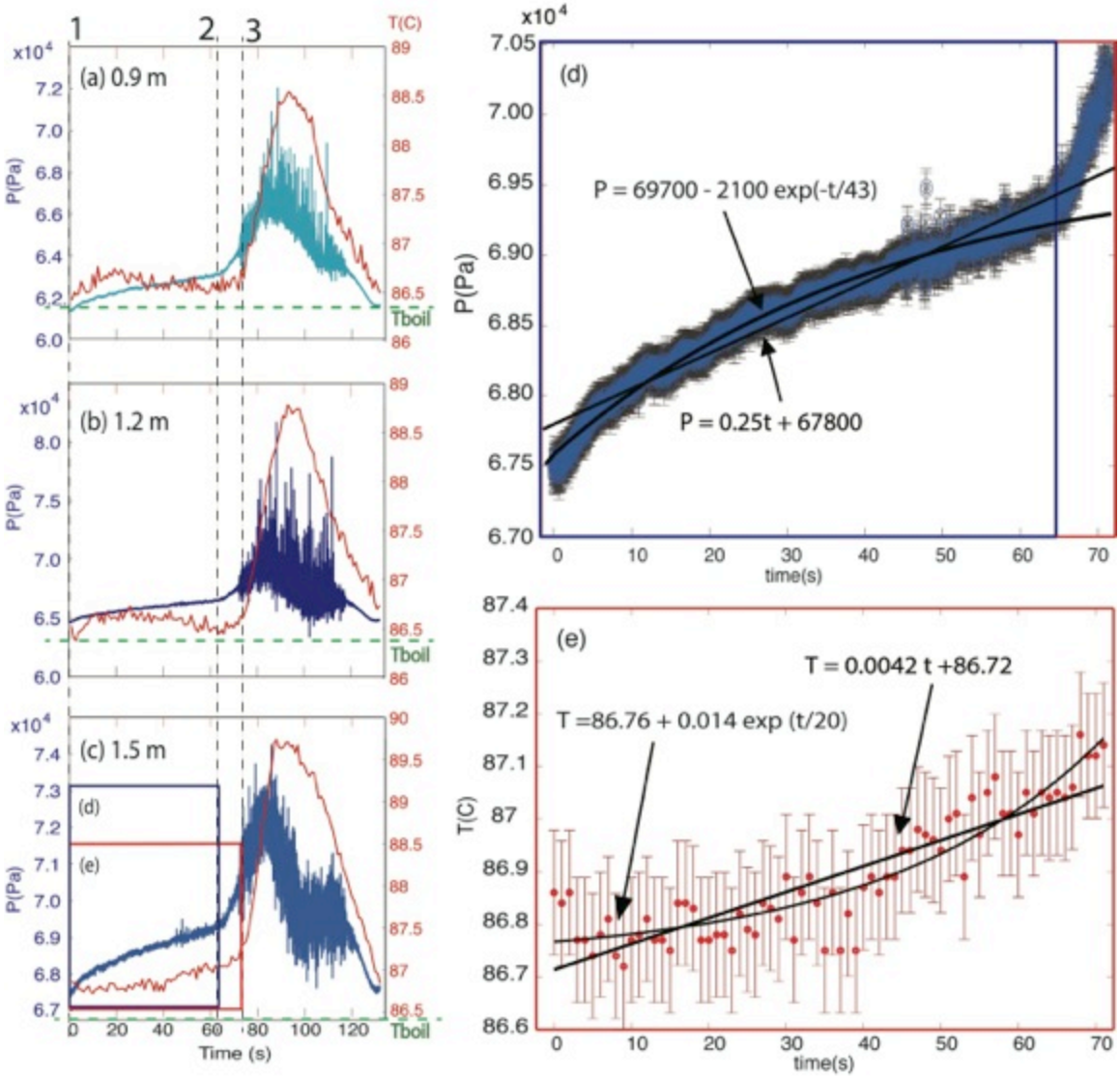

Figure 2.12: Pre-eruption signal

(a) Spectrogram of four eruption cycles (pressure sensor at 1.5 m). We observe the same pre-eruption signal in every cycle. (b) Time series of pressure during the resting time and beginning of the eruption. Spectrograms of pressure at (c) 1.2 m, and (d) 0.9 m show that main frequency in the pre-eruptive signal is 0.5 Hz. Plots below the spectrograms (dark green line) in (c) and (d) show the single-sided amplitude spectrum based on fast Fourier transform (FFT).

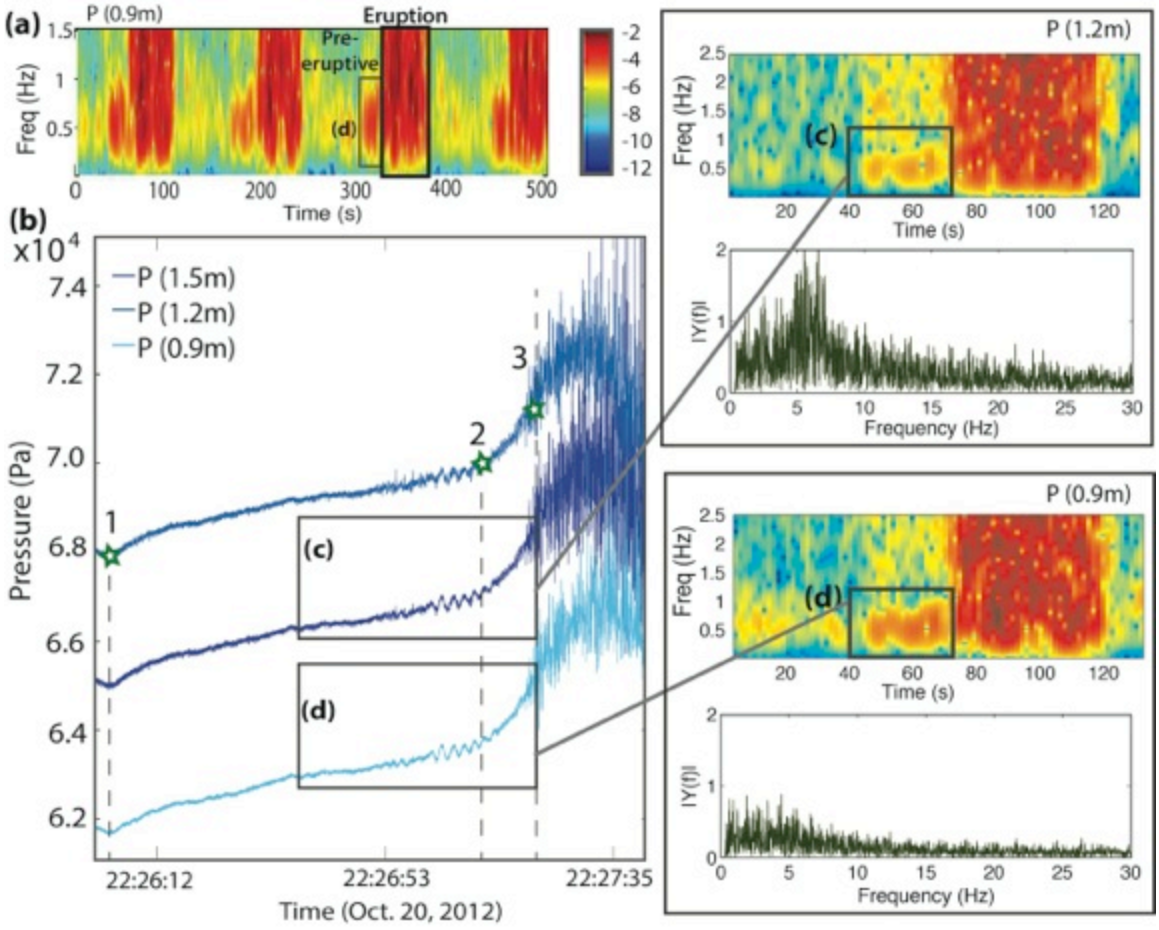

Figure 2.13: Pressure propagation

(a) Pressure data of a subsample of five eruptions from a sensor located at a depth of 1.5 m. Plots (b) and (c) show the cross-correlation between pressure data from different depths. Time is shown on the horizontal axis and the vertical axis shows the time lag (in seconds) for the cross- correlation. (b) Cross-correlation of sensors located at 1.2 m and 0.9 m, showing a strong cross-correlation at a time lag of -0.1 s (black box). The negative lag means that the signal arrives first at 1.2 m and then at 0.9 m, propagating upward with a speed of 3 m/s. (c) Cross-correlation between sensors located at 1.5 m and 0.9 m, showing a strong signal at -0.15 s (black box). The pressure signal is moving upward with a speed of 4 m/s. (d) Pressure data subsample of 2 s during the eruption.

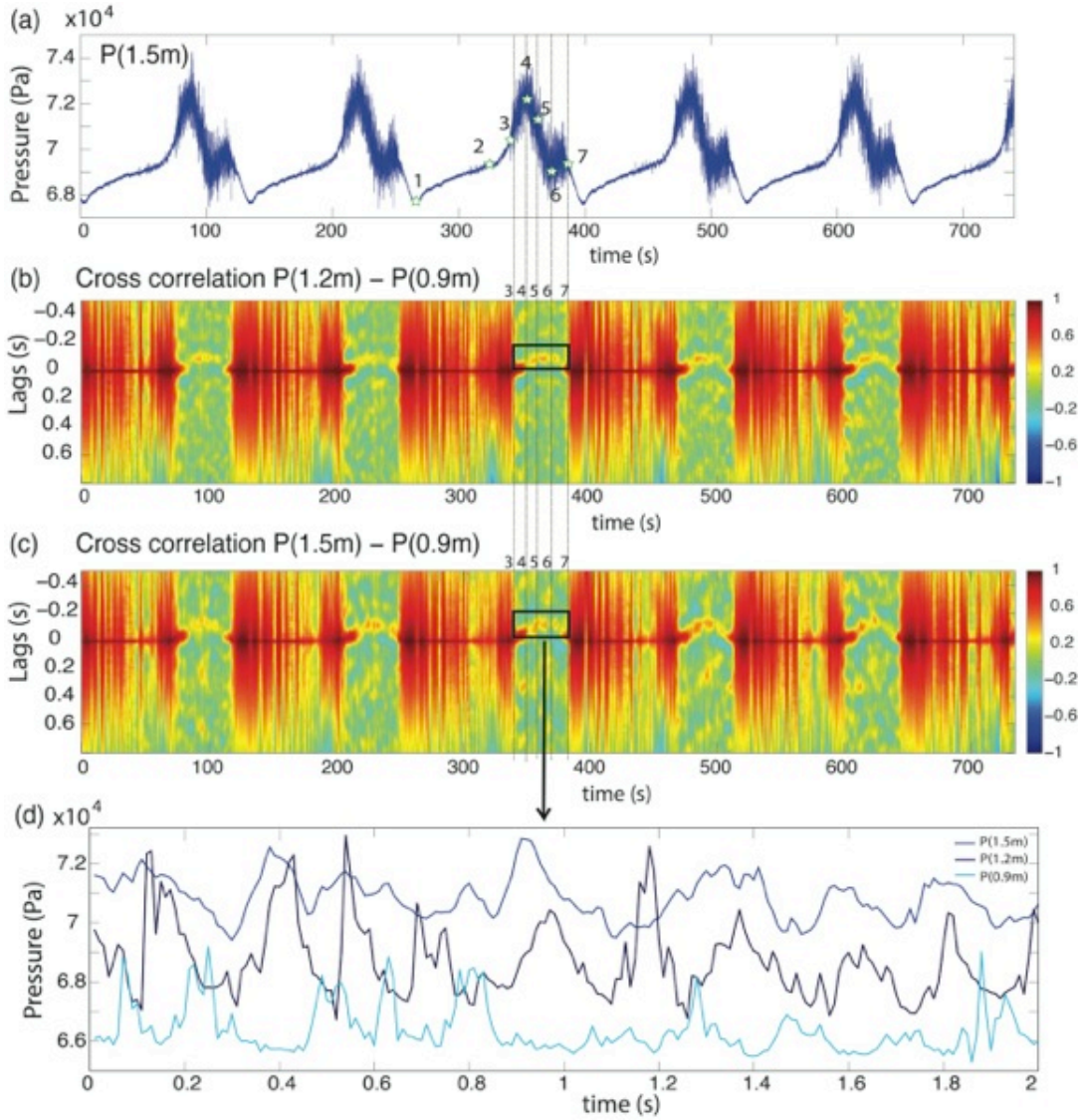

Figure 2.14: Conceptual model for geyser eruption

Conceptual model for El Jefe geyser showing the different stages of the eruption cycle: recharge, pre-eruption, eruption, and relaxation. The model includes a bubble trap or cavity adding steam to the conduit. Blue dots inside the conduit represent bubbles of steam. Blue background represents liquid water. Conditions of pressure (*P*), temperature (*T*), water level (*Z*), and mass flow (*G*) inside the conduit evolve with time. The progression from t_1 to t_7 correspond to the key stages in the cycle (Figure 2.3).

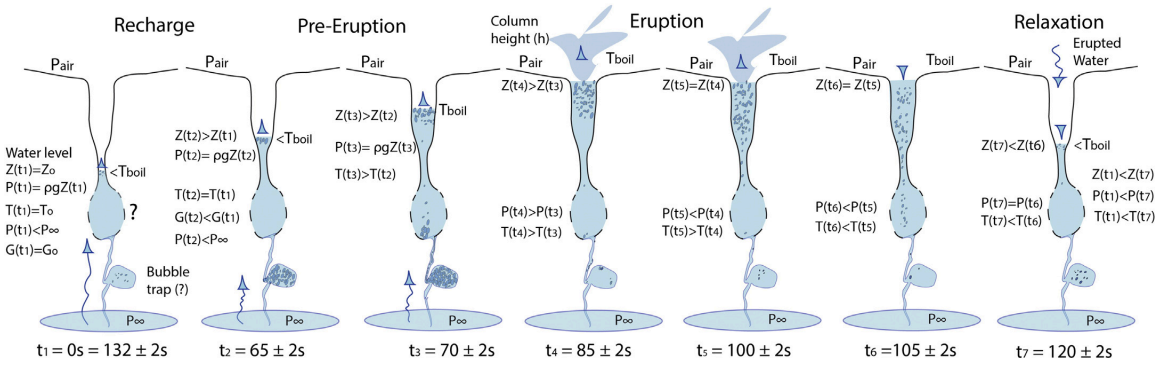

Chapter 3 Geyser eruption intervals and interactions: examples from El Tatio, Atacama, Chile.

The following chapter includes work previously published in:
Munoz‐Saez, C., Namiki, A. and Manga, M., 2015. Geyser eruption intervals and interactions: Examples from El Tatio, Atacama, Chile. Journal of Geophysical Research: Solid Earth, 120(11), pp.7490-7507.

3.1 Abstract

We compare and contrast data collected in 2012 and 2014 from the El Tatio geyser field, Chile. We identify geyser systems that evolve over time, including changes in the interval between eruptions (IBE), development of new thermal features, and interactions between geysers. We study three different cases: (a) an isolated geyser, which is periodic and has nearly identical eruptions every cycle; (b) a geyser and coupled non-eruptive pool, where the geyser has non-regular cycles and several pre-play eruptions before the main eruption; (c) two geysers and a mud volcano, which have non-regular cycles and are all interacting. Though geysers erupt with different styles, we recognize some common features: the conduit recharges with liquid during the quiescent period, bubbles enter the conduit before eruptions, and eruptions occur when water boils in the upper part of the conduit. The episodic addition of heat may govern the periodicity, while the depth where heat is added dictates the eruption style: conduits with deeper heat input are more likely to show pre-play or minor eruptions. The interactions between thermal features can be explained by pressure transmission in subsurface permeable layers between geyser conduits.

3.2 Introduction

Geysers are eruptive hot springs that episodically discharge steam, liquid water, and non-condensable gases. Most geysers on Earth are concentrated in Yellowstone National Park (United States), Geyser Valley (Russia), and El Tatio (Chile). Formation of geysers in these areas is due to particular combinations of water supply, heat sources, and

fractures and/or porous rocks (e.g., White, 1967; Fournier, 1969; Kieffer, 1989; Ingebritsen and Rojstaczer, 1993, 1996; Kedar et al., 1998; Kiryukhin et al., 2012).

Subsurface geometry and fluid flow pathways may govern eruption characteristics. Conduits and reservoirs in the geysers system may have a complex geometry (Hutchinson, et al., 1997). Cavities underneath geysers may act as "bubble traps", accumulating liquid and steam (Belousov et al., 2013). The episodic release of fluid from the cavities can be linked to the periodicity of eruptions (Mackenzie, 1811; Belousov et al., 2013; Vandemeulebrouck et al., 2013; Adelstein et al., 2014; Munoz-Saez et al., 2015a). Bubbles of steam can also transfer enough heat to warm water in the conduit and permit sustained eruptions (Kieffer, 1984, 1989; Adelstein et al., 2014). Geysers may also be hydraulically connected with other nearby thermal springs (e.g., Scott, 1992, 1994), and diffusion of fluid pressure changes may be responsible for the communication between geysers (Rojstaczer et al., 2003).

There remain open questions about the geometry beneath geysers and their interaction with other springs: How is the eruption cycle of a geyser influenced by other adjacent and distant thermal sources? Are hot springs and geysers connected through permeable pathways? Why do so few hot springs erupt as geysers?

We studied geysers whose eruption characteristics evolve over time and interact with those of other hot springs or geysers. During one week periods in October 2012 and October 2014, we made measurements at three different geysers that display differing degrees of complexity in their eruption cycles: (1) an isolated geyser that erupted regularly, called El Jefe (EJ), representing the simplest case; (2) a geyser that interacts with an adjacent thermal pool, called Vega Rinconada geyser (VRG) and Vega Rinconada pool (VRP), respectively; and (3) a geyser that in 2012 was an independent single system called El Cobreloa geyser (CL), but in 2014 was found interacting with a secondary geyser called El Cobresal (CS), and a mud volcano (MV). In 2012, we did not observe the secondary geyser (CS) erupting; however, sinter had accumulated around the vent, indicating that it was a pre-existing feature. The mud volcano (MV) was a small fumarole in 2012. Most of the 2012 data at El Cobreloa and El Jefe geysers were previously reported by Namiki et al. (2014) and Munoz-Saez et al. (2015a), respectively.

3.3 El Tatio Geyser Field

The El Tatio geyser field is located in the Altiplano area of the Atacama Desert in the north of Chile (Figure 3.1a). The elevation of the area is 4.2 to 4.3 km above sea level, where the boiling temperature of water is approximately 86.6°C. El Tatio is the third largest geyser field in the world and includes more than 80 active geysers (Glennon and Pfaff, 2003). The water supply for the geyser field is located 15 to 20 km to the east in the Bolivian Altiplano (Lahsen, 1976; Cusicanqui et al., 1976; Giggenbach, 1978; Munoz and Hamsa, 1993; Cortecci et al., 2005). The heat is provided by Holocene

andesitic stratovolcanoes (with non-historical eruptions) that surround the geyser field (Lahsen, 1976ab). Permeability is dominated by open fractures in the ignimbrite layers, according to data from geothermal wells (Cusicanqui et al., 1975, 1976).

A north-south trending half-graben structure generates the El Tatio basin, which is filled with ~ 1 km of sub-horizontal Miocene and Pliocene ignimbrites, tuffs and lavas, and covered by Holocene alluvial and glacial deposits (Healy, 1974; Lahsen and Trujillo, 1975). Wells indicate that the geothermal reservoir is located in the highly fractured Pliocene ignimbrite Puripicar (Cusicanqui et al., 1975, 1976), and the maximum temperature measured was 253^{o}C (Lahsen and Trujillo, 1976). Chemical and isotopic data from well and surface thermal waters suggest a complex mixing between magmatic, meteoric and hydrothermal sources (Cusicanqui et al., 1975; Giggenbach, 1978; Tassi et al., 2005; Tassi et al., 2010).

The El Jefe isolated geyser (EJ) (Figure 3.1b) has a sinter-lined conduit with a diameter of ~0.3 m near the surface, and the conduit narrows below a depth of 0.8 m; the maximum reachable depth was ~1.7 m in 2014. In the Vega Rinconada geyser-pool system (Figure 3.1c), the geyser (VRG) has a conduit ~10 cm in diameter that opens to a flared vent with a diameter of ~1 m and depth of 0.3 m. At depth the conduit narrows. Measurements with rods suggest that the conduit tilts ~30° from vertical, and our sensors extended down ~8 m (~7 m vertical depth). The pool (VRP) is a non-eruptive hot spring with a diameter of ~0.5 m and is located 2 m away from the geyser. In the geyser-geyser-mud volcano system (Figure 3.1c), the primary geyser El Cobreloa (CL) has a small cone ~0.5 m high connected to the surface by a crack-lined vent. The maximum depth we could reach with instruments is ~1 m, at which point the conduit narrowed and twisted. The secondary geyser, El Cobresal (CS), is located ~8 m east of the primary geyser (CL), and has a conduit ~1.5 m deep and ~0.4 m in diameter. The mud volcano (MV) is located ~5 m north of the primary geyser (CL), and it lies in a surface depression ~2 m in diameter.

3.4 Field measurements and methodology

From 21-28 October 2012, and 2-9 October 2014, we obtained time series of video, ground deformation, temperature, and pressure. We synchronized the instruments and the data loggers with GPS clocks (GlobalSat BU-353 USB GPS Receiver, and Scimolex SC-GPSCLK). For down-conduit measurements, we attached the sensors to a rigid metal rod to keep them in place.

3.4.1 Single geyser (EJ)

In 2012 at EJ we recorded surficial visible and infrared video and measured discharge, tilt and surficial temperature. In the conduit, we recorded video, temperature,

and pressure to a depth of 1.5 m (Munoz-Saez et al., 2015a). In 2014, we measured temperature at the top of the conduit and at depths of 0.7 m, 1.2 m, and 1.7 m, using pre-calibrated K-type thermocouples connected to a QuadTemp 2000 (MadgeTech). The uncertainty in the temperature measurements is < 1.1^{o}C (Omega Thermocouple Home Page). At 1.7 m depth we recorded pressure with a Honeywell pressure sensor (19C030PA4K) connected to a CR-850 (Campbell Scientific) data logger. The accuracy of the sensor is <0.25% of its range of 100mV (Honeywell Sensing and Control), corresponding to ~95 Pa, for a temperature between 0 °C and 82 °C. All instruments recorded at 1 Hz frequency.

3.4.2 Geyser (VRG) - pool (VRP)

In 2012 at VRG, temperature and pressure measurements were made inside the conduit. Eight evenly spaced sensors measured temperature from the surface to a depth of 7 m. Considering the conduit tilt, the corrected vertical depths are: 0.0 m, 0.9 m, 1.7 m, 2.6 m, 3.5 m, 4.3 m, 5.2 m, and 6.1 m. We measured pressure during two eruptions at vertical depths of 4.3 m and 6.1 m. At VRP we recorded temperature and pressure at a depth of 3 m for 3 days. We did not record pressure at VRP and VRG simultaneously.

In 2014, we installed a similar temperature array for two days, adding one pressure sensor at a vertical depth of 4.3 m. For the next five days we recorded temperature 0.3 m above the surface (in the air) and at vertical depths of 0.9 m, 2.2 m, 3.5 m, 4.8 m, 5.6 m, and 6.3 m, with one pressure sensor added at 6.3 m. At VRP, we recorded pressure and temperature at a depth of 2 m for the entire period.

For temperature measurements, we used pre-calibrated K-type thermocouples connected to QuadTemp 2000 (MadgeTech) data loggers measuring at 1 Hz frequency. For pressure, we used Honeywell transducers (models 19C050PA4K and 19C030PA4K) mounted in watertight housings. In 2012, we connected the pressure sensors of VRG to a 24-bit Nanometrics Taurus logger recording with a frequency of 100 Hz. In 2014 the sensors were connected the sensors to a CR-1000x (Campbell Scientific) data logger recording with 1 Hz frequency. The pressure sensor in VRP was connected to a CR-1000x (Campbell Scientific), recording with a frequency of 1 Hz.

3.4.3 Primary geyser (CL), secondary geyser (CS), and mud volcano (MV)

In 2012 at CL we recorded surficial video and made surficial acoustic and temperature measurements (Namiki et al., 2014). In 2014, we recorded ground deformation with a tiltmeter located 3.5 m northwest of the vent. Pressure and temperature were measured in the geyser conduit at ~1 m depth, which is above water level while the geyser is quiescent. The temperature of water at the ground surface was measured 0.5 m northwest, and 3.5 m west of the vent. At the CS geyser, we recorded video and measured temperature inside the conduit at depths of 0.0 m, 0.4 m, 0.8 m and 1.2 m. At the MV we recorded video on 8 Oct. 2014 and measured temperature at the

surface on 9 Oct. 2014.

The instrumentation consisted of two digital video cameras with resolutions of 1920 × 1440 and 1920 × 1080 pixels recording 30 frames per second. The tiltmeter was calibrated to a resolution of 0.23μ rad mV^{-1} (Applied Geomechanics Inc. Surface Mount Tiltmeter Model No. 701-2). At CL, pressure sensor XPM10 (the accuracy of the sensor is <0.25% of its range, corresponding to 100 Pa), K-type thermocouples and the tiltmeter were connected to a HIOKI 8430 data logger recording at 100 Hz, though the response times of K-type thermocouples and the tiltmeter were longer than 10 ms. The temperature at CS was recorded every 1 s with a QuadTemp 2000 (MadgeTech) data logger. The pressure sensor located in the CS conduit leaked, and no data could be collected.

3.5 Results: Time series

3.5.1 Isolated geyser (EJ)

The evolution of both pressure and temperature at EJ are very similar between eruptions, and the interval between eruptions (IBE) is extremely regular (Figure 3.2ab). Data from 2012 (Munoz-Saez et al., 2015a) showed that the eruption cycle at EJ has a mean IBE of 132.2 ± 2.4 s for 3,531 eruptions (Figure 3.2a). In 2014 (Figure 3.2bde), the mean IBE decreased ~20%, to 105.0 ± 3.2 s for 4,150 eruptions. This reduction reflected mostly the quiescent period, which decreased from 80 ± 3 s in 2012 (Munoz-Saez et al., 2015a) to 63 ± 4 s in 2014.

Based on 2012 data (Figure 3.2c), seven reference points in time identified different key stages in the eruption (Munoz-Saez et al., 2015a) and are also applicable to data from 2014 (Figure 3.2cde). Point 1 indicates the beginning of the geyser cycle; it coincides with the minimum water level and pressure inside the conduit (Figure 3.2ce). The lower part of the conduit was under-water the entire cycle (Figure 3.2e). Pressure increases from point 1 at 1.7 m, documenting refilling of the conduit. Point 2 marks the beginning of a rapid pressure increase (Figure 3.2ce), which coincides with a rapid 2.5 to 3°C increase of temperature (Figure 3.2e). This change is detectable only at 1.7 m, and was not observed in 2012 when measurements were restricted to depth less than 1.5 m. Temperature also starts increasing at 0.6 m (Figure 3.2d) when hot water reaches the sensor as the water level rises in the conduit. Point 3 indicates a sudden increase in pressure with large fluctuations (Figure 3.2ce), and temperature increases in the entire conduit (Figure 3.2cde). Between points 3 and 4, water at 0.6 m reaches boiling conditions and the fountaining begins at the surface. Point 4 indicates the maximum pressure in the conduit (Figure 3.2ce); after this point, pressure decreases at an approximately constant rate. Immediately after point 4, the temperature at 1.7 m has a second peak (Figure 3.2e), which occurs earlier than in the rest of the conduit and (again) was not detected in 2012 (Figure 3.2c). Point 5 indicates the maximum water temperature at 1.2 m, coincident with data from 2012, while pressure and temperature at 1.7 m are

still decreasing. After this point, temperature at depths of 1.7 m, 1.2 m and 0.6 m decreases at an approximately constant rate. At Point 6 the rate of pressure decrease changes, and this corresponds to the end of fountaining at the surface, which produces a rapid drop in the temperature in the upper part of the conduit, first at 0.0 m and then at 0.6 m (Figure 3.2d). Point 7 identifies the end of the pressure fluctuations, an increase in the rate of pressure decrease, and the end of the geyser cycle. After this point, erupted water returns to the conduit, increasing temperature in the upper part of the conduit, first at 0.0 m and then at 0.6 m (Figure 3.2d).

3.5.2 Geyser (VRG) - pool (VRP)

The IBE analysis shows that the duration of eruption cycles changed from 2012 to 2014 (Figure 3.3), at least during the periods of measurements. However, the features of the cycles in both years are similar (Figure 3.4). In 2012, we measured 117 eruption cycles. The IBE varied from ~0.69 h to ~2.08 h, with a bimodal distribution centered at 1.4 h and 2 h for the major and minor peaks respectively (Figure 3.3a), and a mean IBE of 1.4 $\pm$ 0.4 h (standard deviation). In 2014, we measured 118 eruption cycles. The IBE had less variability, from 0.75 h to 1.80 h. IBE values showed an asymmetric distribution centered at 1.4 h (Figure 3.3b), and the mean IBE was 1.5 $\pm$ 0.2 h. We calculated IBE using the local maximum of smoothed temperature measurements at 6.1 m depth as the beginning of an eruption and the local minimum at 0.9 m as the end of the eruption.

In both 2012 and 2014, pressures at different depths in the geyser conduit vary in the same way as pressure in the pool (Figure 3.4cd). The temperature in the geyser changes at different depths, and over time (Figure 3.4bc), while the temperature in the pool remains constant and below boiling (~85^{o}C) (Figure 3.4d). Cycles have different durations (Figure 3.3), but they have the same stages: a main eruption (Figure 3.4 letter A) and a quiescent period that can be divided in two stages; minor discharges of water (Figure 3.4 letter B) and water level changes at the conduit surface (Figure 3.4a).

During the main eruption (Figure 3.4 letter A), temperature increases in the deepest accessible part of the geyser conduit from ~90.5^{o}C to 94^{o}C (Figure 3.4b) and decreases in the middle part (3 to 5 m depth) from ~90.5^{o}C to 89^{o}C (Figure 3.4bc). Pressure decreases at the beginning of the main eruption, levels out in the middle of the eruption, and then decreases again at the end of the eruption (Figure 3.4cd). Both pressure drops produce large splashes of water at the surface (Figure 3.4ac).

After the main eruption (Figure 3.4 letter B), during the first part of quiescent period, pressure increases irregularly, with two marked pressure drops of ~0.5 x 10^4 Pa (Figure 3.4c) that coincide with small splashes or eruption of water at the surface (Figure 3.4ac). Shorter eruption cycles have one or no pressure peaks during this period. In general, temperature tends to increase at an approximately steady rate of ~ 3.6^{o}C/h throughout the conduit. In the deepest part of the conduit (Figure 3.4b) temperature shows some small peaks coincident with the pressure peaks. In the middle part of the

conduit (3 to 4 m depth) the temperature drops somewhat, following the changes in pressure (Figure 3.4bc), and this region remains slightly colder than the rest of the conduit (Figure 3.4b).

During the second half of the quiescent period (Figure 3.4 letter C), pressure at depth increases and becomes constant (Figure 3.4c) while the conduit overflows at the surface (Figure 3.4a). At the same time, temperature in the deepest part of the conduit increases ~2^{o}C (Figure 3.4b), followed by an increase of temperature in the rest of the conduit. After that, pressure drops again, ~0.2 x 10^4 Pa, water level drops at the surface, and temperature decreases in the middle of the conduit (Figure 3.4abc). Next, pressure increases as water level increases, and pressure becomes constant once the conduit overflows again. Temperature increases in the middle of the conduit until a new main eruption occurs.

3.5.3 Primary geyser (CL), secondary geyser (CS), and mud volcano (MV)

The CL geyser in 2012 was characterized by a main eruption every ~4.66 h, preceded by several minor eruptions every ~0.23 h (Namiki et al., 2014). The main eruption lasted ~1 h, started as liquid-dominated, and evolved to steam-dominated. Minor eruptions splashed hot water intermittently. We did not observe other time dependent features: CS was not erupting, and MV was a fumarole.

In 2014, CS and MV had intermittent eruptions, and eruptions of CL, CS, and MV are correlated (Supplementary Material: Video # 1 Munoz-Saez et al., 2015b). Minor eruptions of CL and eruptions of CS, and MV occur at similar intervals. MV erupts just after the eruption of CS. During the steam-dominated eruption of CL, CS stops erupting. At the end of the first eruption of CS after the CL eruption, MV has a vigorous eruption that includes the ejection of pebbles.

We identified “main eruptions” from strong signals in the temperature, pressure, and tilt data. Compared with 2012, the main eruptions at CL were irregular and shorter, presenting a bimodal distribution of the IBE centered at 0.75 h and 2.75 h, the minor and major peaks respectively (Figure 3.5a) for the 35 eruptions we measured. The mean IBE is ~2.16 h $\pm$ 0.86 h. Discharge of fluid during the eruptions lasted ~0.25 h to ~1 h depending on the duration of the cycle. Within main eruptions, we recognize small peaks in the temperature record inside the conduit that correspond to minor eruptions. Minor eruptions occur almost regularly, every ~0.24 h. We use video observations to confirm that these signals are associated with minor eruptions at the surface. For the secondary geyser CS we measured 280 eruptions (Figure 3.5b). The IBE presents an asymmetric distribution centered at 0.2 h (Figure 3.5b), and the mean IBE was 0.26 $\pm$ 0.09 h. For the MV we did not record enough eruptions to establish meaningful statistics.

At CL, during a main eruption, the temperature at 1 m depth in the conduit (Figure 3.6ab) increases to 94^{o}C, with one or more pulses. High temperature is sustained for several minutes and then temperature decreases steadily to ~85^{o}C by the end of the

eruption. Temperature at the geyser surface also increases (Figure 3.6a), as erupted water reaches the sensors deployed around the vent. The pressure in the conduit increases correspondingly (Figure 3.6b). By the end of the eruption, pressure decreases to a value close to atmospheric (6.1×10^4 Pa), indicating that the conduit is almost empty. The sub-atmospheric values of pressure can be attributed to noise and other pressure fluctuations coming from the empty conduit. The tilt (Figure 3.6c) increases at the beginning of an eruption, but more slowly than the pressure signal. After the eruption, tilt in the radial direction decreases slowly. Throughout the minor eruptions (Figure 3.6bd), temperature in the conduit (Figure 3.6ab) increased to ~86.6^{o}C (boiling point at atmospheric pressure). Minor eruptions of CL become progressively more vigorous following a main eruption of CL (Figure 3.6b), as Namiki et al. (2014) previously described for 2012 data, but not as systematically in 2014. Pressure tends to increase as temperature increases. When the geyser is not erupting, temperature is lower than 85^{o}C, and pressure shows large amplitude and high frequency variations about the atmospheric value (Figure 3.6bd). There are no detectable tilt signals during minor eruptions (Figure 3.6c).

At CS geyser (Figure 3.7), we observe that when an eruption occurs the temperature increases sharply to 86 - 87^o C in the entire conduit, and maintains that value throughout the eruption. Once the eruption ends, the conduit empties and the temperature decreases below 50^{o}C as erupted water pours back in the conduit. The duration of the eruption is almost the same in each cycle, but the quiescent period varies (Figure 3.7b). Temperature in the deepest part of the conduit (Figure 3.7a, 1.2m) increases gradually as the conduit refills, and for longer quiescent periods the conduit refills more slowly before an eruption. The CS geyser stops erupting during the first maximum of temperature in the main eruption (Figure 3.6 and 3.7).

From temperature data (Figure 3.8), we observe that the temperature of MV is mostly maintained at a constant value close to the boiling point of water at the surface (86.6^o C). Temperature in the MV (Figure 3.8) decreases at beginning of the CS eruption and during minor eruptions of CL as liquid water flows to MV (Supplementary Material: Video # 1 Munoz-Saez et al., 2015b). We observed that the MV eruptions start at the end of the CS eruption (Supplementary Material: Video # 1 Munoz-Saez et al., 2015b) and the MV overflows during the main eruption of the CL (Figure 3.12).

3.6 Discussion

3.6.1 Eruption Cycle

The geyser systems we studied present cycles of different complexity: the isolated geyser EJ has a single eruption per cycle, while VRG and the primary geyser CL have several minor eruptions preceding the main eruption. However, we recognize in all cases similar behaviors and eruption stages: recharge, pre-eruption, and eruption. The recharge is characterized by an increase of the hydrostatic pressure in the conduit as we observed

at EJ (Figures 3.2 and 3.9, numbers 1 to 2) and VRG (Figures 3.4 and 3.9, B and C). A pre-eruptive signal is observed in the pressure data before every eruption in EJ and VRG (Figure 3.10).

In CL geyser, the pressure during the quiescent period (Figure 3.9) is close to atmospheric values with temperatures below boiling, indicating that the conduit is empty at ~1 m, and we do not observe the recharge and pre-eruption signal. For the secondary geyser (CS) we observe recharge during the quiescent period (Supplementary material: Video #2 Munoz-Saez et al., 2015b). During an eruption (Figure 3.9 and Munoz-Saez et al., 2015a), the temperature and pressure follow the boiling curve, with no clear evidence of superheated fluid. At EJ and CL, we recorded pressure in the shallow conduit, which increases at the beginning of the eruption.

At EJ, pressure increases as the conduit fills during the liquid dominated part of the eruption, and never exceeds the hydrostatic pressure. In contrast, at CL, pressure exceeds hydrostatic values, suggesting that there is high-pressure steam within the conduit. As the eruption progresses, pressure and temperature decrease and follow the boiling curve as steam escapes from the vent and the conduit empties.

At VRG we could reach depths well below the surface, providing insight into deeper parts of the geyser system. Pressure and temperature deeper than 4.3 m are below boiling during the entire cycle (Figure 3.9). This offset from the boiling curve occurs only at depth, given that the temperature in the upper part of the conduit is close to the boiling temperature at atmospheric pressure (~86^{o}C Figure 3.4b). At depth, pressure and temperature during the main eruption (Figure 3.9 path A) evolve parallel to the boiling curve. Eruptions are initiated with a sudden increase of temperature and decrease in pressure, which can be attributed to the addition of steam. Addition of steam produces movement of fluid, and decreases the density of the fluid above the sensor. Pressure in the pool VRP tracks that in the geyser VRG.

1.1.1.11. Recharge

From pressure data at EJ and VRG, we can estimate hydraulic parameters for the "aquifers" providing water to the conduit. During the quiescent period the water level in the conduit of the isolated geyser EJ increases, which corresponds to changes in the hydraulic head $H(t)$ in the conduit. We assume that water drains from a deeper reservoir of constant hydraulic head H_∞ to the conduit with $H(t) < H_\infty$. The volumetric rate of refilling $S\frac{dH}{dt}$ (S is the cross section of a constant-radius conduit) is proportional to the head difference between the conduit and the reservoir:

$$S\frac{dH}{dt} = -g\alpha\,(H(t) - (H_\infty))\,, \qquad (1)$$

where g is gravity, and α is the constant of proportionality that relates flow to head differences. By analogy to Darcy's law (Steinberg et al., 1982; Kedar et al., 1998,

Rudolph et al., 2012; Munoz-Saez et al., 2015a), α depends on the hydraulic parameters of the conduit and aquifer: hydraulic conductivity *K*, the distance *L* to the reservoir, and the surface area, *A*, over which recharge occurs. Hereafter, we define *H*=0 to be the local ground surface.

Integrating equation (1), and applying the initial condition H_0 at $t = 0$, we obtain

$$H(t) = H_\infty + (H_\infty - H_0)(e^{\frac{-t\alpha g}{s}}) \quad . \qquad (2)$$

Considering the depth of the sensor, and transforming the measured pressure to hydraulic head by subtracting the atmospheric pressure and dividing pressure by density times gravity (ρg), we fit the data during the quiescent period and obtain for EJ in 2014: $H_{\infty EJ} = -0.82 \pm 0.05$ m, $H_{\infty EJ} - H_{0EJ} = 0.25 \pm 0.03$ m, $\left(\frac{S_{EJ}}{\alpha_{EJ} g}\right) = 33.90 \pm 4\ s$. From the fit we obtain $H_{0EJ} = -1.07 \pm 0.04$ m, which is consistent with the value obtained from the measured minimum pressure $H_{0\_data} = -1.03 \pm 0.05$ m. Using for S_{EJ} the cross section area for a conduit of radius 0.2 m, $\alpha_{EJ} = (4.30 \pm 0.60) \times 10^{-4}$ m · s. From pressure data in 2012 (Munoz-Saez et al., 2015a), we obtain: $H_{\infty 2012} = -0.81 \pm 0.01$ m , $H_{0\_2012} = -1.02 \pm 0.01$ m , $\left(\frac{S_{2012}}{\alpha_{2012} g}\right) = 43.00 \pm 4.00$ s , and $\alpha_{2012} = (3.40 \pm 0.20) \times 10^{-4}$ ms. Parameters are similar in both years, indicating that the properties of the conduit and aquifer did not change significantly.

For VRG, the recharge of the conduit is interrupted by minor eruptions of water. Before every minor and main eruption, the pressure increases. Using equation (2) we can determine the evolution of hydraulic head documented by the pressure changes. We obtain $H_{\infty VR} = -0.02 \pm 0.07$ m. The parameter H_{0VR} increases from -1.06 ± 0.1 m to during the first part of the recharge (Figure 3.4, 3.9, 3.10a period B) to -0.15 ± 0.05 m during the second part (Figure 3.4, 3.9, 3.10a, period C), which is consistent with refilling of the conduit, and successively higher initial water levels. The last term $\left(\frac{S_{VR}}{\alpha_{VR} g}\right)$ varies, reflecting changes in the geometry of the conduit; the parameter changes from 147 ± 15 s during the first part, where the conduit is being recharged (period B), to 345 ± 20 s during the second part, when the conduit overflows (Figure 3.4a, period C), and water accumulates in a wider depression at the surface. Considering αg constant, the conduit cross section (*S*) at depth may be half of the cross section at the surface.

Values of H_∞ within a couple m of the local ground surface are similar to those inferred by active experiments performed at two geysers in Kamchatka (Shteinberg et al. 2013). High overpressures in a recharging reservoir thus do not appear necessary for geyser eruptions.

After the main eruption of CL, the radial component of the tilt decreases continuously, which requires continued subsurface movement of fluids. A porous conduit or a porous layer connecting different geyser conduits would permit circulation of fluids

below the surface. Geysering wells show a very different evolution of tilt (Nishimura et al., 2006; Rudolph et al., 2012), with the tilt gradually increasing during the quiescent period. Conduits for artificial geysers are isolated pipes, and the measured ground deformation records fluid flow at the depth where the well is recharged. This hypothesis can explain the fact that the magnitude of the tilt signal is one order of magnitude larger than values reported at other natural geysers (Munoz-Saez et.al, 2015) and geysering wells (Nishimura et al., 2006; Rudolph et al., 2012). The measured tilt near CL shows water recharge of shallow aquifers; in other instances, tilt reflects changes in deeper aquifers.

For the secondary geyser CS, during the recharge period (Supplementary Material: Video # 1 Munoz-Saez et al., 2015b) the water level increases, but in a discontinuous way, which we attribute to the influence of CL eruptions.

1.1.1.12. Pre-eruptive behavior

By the end of recharge in the isolated EJ geyser, we observe a peak in temperature at 1.7 m in the 2014 data (Figure 3.2 and Figure 3.9, points 2 to 3) that coincides with an increase in the rate of pressure change and with a 2 Hz pre-eruptive signal described in 2012 (Munoz-Saez et al., 2015a). Similarly, in the geyser conduit of VRG, we identified a 3.5 Hz pre-eruptive signal preceding the main eruption and a 3.5 to 2 Hz signal when the pressure reaches a local maximum before every minor eruption (Figure 3.10). Some of those pressure peaks overlap with small temperature peaks in the deepest part of the conduit. Temperature peaks overlapping with the pre-eruption pressure fluctuations at EJ and VRG support the interpretation that steam bubbles are flowing into the conduit (Mackenzie, 1811, Hutchinson et al., 1997; Belousov et al., 2013; Vandemeulebrouck et al., 2013; Adelstein et al., 2014; Munoz-Saez et al., 2015a). In down-conduit videos from CS (Supplementary Material: Video # 2 Munoz-Saez et al., 2015b) we observe sporadic addition of bubbles during the entire recharge period that intensified before the main eruption.

1.1.1.13. Liquid/steam distributions in the conduit during minor and main eruptions

The eruptions of the isolated geyser EJ (Figure 3.2ce) and the primary geyser (CL) (Figure 3.5) started with a sudden increase of temperature and pressure, and both temperature and pressure decrease as the eruption progress. At EJ, pressure shows large fluctuations during an eruption (Figure 3.2ce) that can be associated with boiling and bubble collapse (Kedar et al., 1998; Munoz-Saez et al., 2015a; Vandemeulebrouck et al., 2014). Pressure never rises above the hydrostatic value for a liquid-filled conduit.

During minor eruptions at CL, the temperature of the water is close to boiling conditions at atmospheric pressure, whereas during the main eruption, pressure and temperature increase significantly and continue to follow the boiling curve (Figure 3.9). Namiki et al. (2014) show that boiling in the reservoir releases steam and hot liquid water to the conduit, causing minor eruptions, and heating the conduit. Eventually the water becomes warm enough to boil, leading to a steam-dominated eruption that empties the conduit. During the field measurements in 2014, the sensor was located at a depth of 1 m. If the conduit was full of water, the hydrostatic pressure would be 10^4 Pa, greater than the atmospheric value. During the minor eruptions pressure increases to this value (Figure 3.9), consistent with the conduit filling with liquid during a liquid-dominated eruption. During the main eruption, pressure exceeds the hydrostatic value (Figure 3.9), which can be attributed to increased vent pressure as steam is forced through the vent. During the steam-dominated part of the main eruption, only steam exists at the vent. The tilt of the surface follows pressure in the conduit, suggesting that water is supplied to the shallow aquifer by the main eruption. Pressure increases inside the conduit, and the ground rises in the direction of the vent, consistent with tilt measurements at other natural geysers such as EJ (Munoz-Saez et al., 2015a). The very short, large amplitude tilt anomaly at the very beginning of each eruption is likely the poroelastic Noodbergum effect caused by faster propagation of mechanical deformation than hydraulic propagation of pressure changes, magnified where there are very compressible formations (Kim and Parizek, 1997).

Minor eruptions at VRG followed a single-step pressure drop in the conduit and a slight temperature increase at depth. The main eruption occurs during a two-step pressure drop that overlaps with a large peak in temperature in the deepest part of the conduit. We interpret the temperature increment in the deepest part of the conduit before and during an eruption as bubbles being released from a cavity or a boiling reservoir. Consequently, the pressure drops in the conduit due to liquid water moving down the conduit and fluid above the sensor becoming less dense owing to the addition of bubbles. The boiling temperature is reached in the upper part of the conduit (Figure 3.4b) where temperature is close to the local boiling temperature. According to the model fit during the recharge period (section 5.1.1) and visual observations (Figure 3.4), the conduit of VRG is full of water before the eruption begins, and then a large mass of water is removed from the conduit during the eruption and causes the decease of pressure. This also explains the opposite behavior of pressure in VRG, where pressure decreases at the beginning of an eruption. At EJ and CL the upper part of the conduit was empty before the eruption, and filled with water during an eruption, increasing the pressure.

The temperature in the middle of the conduit remains constant, suggesting that convection occurs in the conduit. Pressure decreases in the conduit would bring the upper part of the water column to boiling conditions if the water in the conduit were warm enough to boil at the surface. If bubble addition is sustained, a main eruption occurs and continues until steam is depleted. Otherwise, minor eruptions occur. Minor eruptions of

water during the recharge are analogous to the preparation stage "pre-play" that precedes the main eruptions characterized by pulses of liquid and/or steam discharge (e.g., Kieffer, 1984; Karlstrom et al., 2013, Namiki et al., 2014; Adelstein et al., 2014), which can heat the conduit before a main eruption (Namiki et al., 2014).

The magnitude of the pressure drops associated with minor eruptions (~0.5 x 10^4 Pa) is similar to each step in the main eruption, consistent with the idea of steam release from a bubble trap (eg. Belousov et al., 2013; Vandemeulebrouck et al., 2013; Adelstein et al., 2014; Munoz-Saez et al., 2015a) rather than fluid from a boiling reservoir (Ingebritsen and Rojstaczer, 1993, 1996; Namiki et al., 2014), and provides insight into the size of the cavity. Considering the range of temperature in the upper conduit and the pressure-dependence of the boiling temperature, water can boil from the surface to ~1 m depth during the minor eruptions and to ~2.5 m depth for main eruptions. In EJ, the eruption at the surface occurs between points 3 to 4 (Figure 3.2cde); then the conduit decompresses and the boiling front propagates downward (Figure 3.2cde, Figure 3.9 between point 5 to 6). At both VRG and EJ, boiling occurs at the top of the water columns and boiling conditions propagate downward.

Given the depth of the heat input in the conduit, the bubble trap connected to VRG may be deeper than that at EJ. The eruption cycle (IBE) at VRG is longer and more irregular than (EJ), because there is more water to warm up in the conduit, and multiple pre-play or minor eruptions are needed to heat the conduit before the main eruption.

3.6.2 IBE and Interactions between geysers

1.1.1.14. Evolution over time

At EJ geyser, we observed a difference of ~20 % in the IBE from 2012 to 2014 that is not associated with changes in recharge, but instead may be caused by changes in the supply of heat, changes in the bubble trap or changes in the permeability of the surroundings (e.g., Ingebritsen and Rojstaczer, 1996). In addition, changes in the IBE of CL from 2012 to 2014, the appearance of the two new two eruptive features (CS and MV), and the change from bimodal (2012) to unimodal (2014) IBEs at VRG (Figure 3.3) highlight the dynamism and complexity of hydrological pathways. However, we cannot establish whether changes in IBE are caused by discrete events or instead occur progressively over time. For example, in February 2013, heavy rain fell in the area of San Pedro de Atacama, 70 km SW of El Tatio (ONEMI, 2013) and on April 1st, 2014 a magnitude 8.2 earthquake occurred in Iquique, ~350 km NW of El Tatio (USGS). Both of these events could potentially have affected the geysers given their magnitudes and locations (e.g., Manga and Brodsky 2006; Hurwitz et al., 2014; Hurwitz and Lowenstern 2014). Numerical simulations show that geyser cycles can be sensitive to changes in porosity, length and permeability of conduit, permeability of surrounding rock, and the

rate of recharge (Ingebritsen and Rojstaczer, 1993, 1996). Dynamic stress from distant earthquakes can modify permeability (e.g., Manga et al., 2012) or the effective conduit length due to changes in the aperture of exiting fractures (Ingebritsen et al., 2006), and changes in recharge can be caused by climatic events. Depending on the orientation of fractures, re-opening fractures can create connective pathways between geysers such as the CL, CS and MV, reactivate a dormant geyser such as CS, and change the eruption behavior of a feature such as MV. Closing fractures can reduce the permeability and reduce the IBE, as documented at EJ. Switching from unimodal to bimodal eruption intervals has also been recognized at other geysers (e.g., Silver and Valette-Silver, 1992) and is not unexpected in hydrothermal systems where nonlinear relative permeability functions are sufficient to lead to switching (e.g., Ingebritsen and Rojstaczer, 1996).

VRG in 2012, and CL in 2014, have bimodal distributions of the IBE (Figure 3.3a and 3.5a). Changes in the IBE have been attributed to changes in the air temperature (Hurwitz et al., 2008, 2014; Merzhanov et al., 1990) and stresses induced by barometric pressure changes (3×10^2 Pa) and solid Earth tides (10^3 Pa) (Hutchinson et al., 1997; Vandemeulebrouck et al., 2013), which occur in daily cycles. In VRG and CL, long and short eruption cycles occur independent of the time of the day (Figure 3.11ac), indicating that the bimodality of those geysers is not the consequence of environmental perturbations. At VRG (Figure 3.11ab), several short eruptions can occur before a long eruption, and the IBE increases progressively until a long eruption occurs; after that, IBE decreases progressively. Pre-play or minor eruptions are absent during the recharge as cycles become shorter. In CL, short and long eruptions cycles usually alternate (Figure 3.11cd). Short cycles may be heating the conduit before a long eruption, and could be considered very large pre-play events.

1.1.1.15. Geyser-Geyser Interaction

The time series (Figure 3.6, 3.7, 3.8) and surface observations (Figure 3.12, and Supplementary material: Video #1 Munoz-Saez et al., 2015b) document the interaction between three eruptive features (CL, CS, and MV), suggesting that a permeable "aquifer" connects all three. As we discussed in Section 5.1.3, pressures inside the conduits fluctuate, which leads to water transport between eruptive features. Here we summarize possible mechanisms for the observed interaction.

As pressure increases in the CL conduit by water recharge, water in a shallow aquifer is sent to the other features. The shallow water is below boiling, suppressing the eruption of the secondary geyser CS (Figure 3.12 and the longer quiescent period in 13 b) and overflowing the MV (Figure 3.12). As the CL conduit fills with steam, the pressure below the vent in the deeper conduit decreases, and water in the aquifer may flow back toward the CL conduit.

Pressure in the conduit of CS may increase at the beginning of the eruption when the conduit fills with water, as occurs at EJ, sending some liquid back to CL and to the MV.

This liquid can produce temporarily liquid-dominated stages during the main eruption of CL (Figure 3.13ab), and decreases the temperature of the MV (Figure 3.8), suppressing its eruption. By the end of the CS eruption, pressure in the conduit becomes low, allowing liquid to flow back to CS and allowing MV to erupt (Figure 3.8, and Supplementary material: Video #1 Munoz-Saez et al., 2015b). The aquifer connecting the geysers must be deep enough (at least a few tens of cm) that it does not sense diurnal variations in temperature. But it must be shallow enough to sense pressure changes in the geyser conduits. The fluid supply from the deeper sources may also be influenced by pressures in the geyser conduits. Some combination of all these factors control the complex interaction among the three eruptive features.

The periodic eruptions and variations in the pressure in the conduit will lead to periodic variations in pore pressure in the porous materials surrounding the geyser. These pressure variations decay exponentially in magnitude with increasing distance from the geyser, decreasing by a factor of e over distance $L_c \sim \sqrt{DT}$, where D is the hydraulic diffusivity and T is the interval between eruption. We infer that the separation of thermal features d is small enough compared to L_c that pressure fluctuations can influence eruptions, that is $d < O(L_c)$. The hydraulic diffusivity $D = \frac{k}{\mu(\beta_1 + \phi\beta_2)}$, depends on the permeability (k), viscosity of water ($\mu = 0.335 \times 10^{-3}$ Pas, near the boiling temperature), compressibility of the rock (β_1) and liquid water (β_2) and porosity (ϕ); $\beta_1 + \emptyset\beta_2$ is $\sim 10^{-10}$ Pa^{-1}. Given the mean IBE of CL ~ 2.16 h, and that the separation of CS and CL is ~8 m, a permeability $k > 10^{-16}$ m^2 should allow pressure fluctuations from one geyser to be sensed at the other. The isolated geyser EJ is located 165 m from CL, so that a permeability $k > 10^{-13}$ m^2 would be needed for an interaction between those geysers. EJ seems to be unresponsive to the other geysers, thus bounding permeability.

1.1.1.16. Geyser-Pool Interaction

Similar changes in pressure in VRG and VRP indicate strong hydrologic connections between the pool and the geyser though a permeable zone. The temperature evolves differently between the pool and the geyser: in VRP the temperature remains constant, while in VRG it varies throughout the geyser cycle, suggesting that the heat source is only directly connected to the geyser conduit. A temperature decrease in the upper part of the geyser conduit, after the pressure decreases, can be attributed to the permeable zone draining colder water into the geyser conduit. The addition of colder water could contribute to ending the eruption. We do not observe warmer water flowing from the geyser to the pool during the eruption, indicating that flux between eruptions is a small fraction of the pool volume.

3.6.3 Conceptual Model

For the single geyser (EJ), episodic addition of heat from below (e.g., a bubble trap) increases the temperature in the upper part of conduit (Figure 3.14). When the water reaches boiling conditions the geyser erupts. Eruptions are frequent (~2 min) and without pre-play.

The geyser (VRG) and the pool (VRP) are hydraulically well-connected. However, addition of heat occurs only in the deepest part of the conduit (Figure 3.14). The bubble trap may be deeper compared to EJ geyser, the IBE is longer, and multiple pre-plays or minor eruptions heat the conduit before the main eruption. During the main eruption, the bubble trap empties, causing flow of liquid water into the cavity, which deceases pressure in the conduit and the pool.

The two geysers (CL, CS) and the mud volcano (MV) are hydraulically connected through a permeable aquifer (Figure 3.14). These all may be connected to a deeper heat source. The main geyser (CL) and the secondary geyser (CS) interact, and both control the periodicity of the MV.

3.7 Conclusion

Our field measurements document that geyser systems evolve over time, including changes in interval between eruption (IBE) and development of new thermal features. These measurements allow us to answer some of the questions highlighted in the introduction:

- How is the eruption cycle of a geyser influenced by other adjacent and distant thermal sources? Are hot springs and geysers connected through permeable pathways? Geysers can be connected through permeable pathways to other nearby hot springs and geysers. Distances must be small enough that pressure changes in one geyser can be sensed at the other geysers. At El Tatio, reasonable permeabilities are inferred based on the separation distance of interacting and non-interacting geysers.
- Why do so few hot springs erupt as geysers? Given enough heat and water, the right subsurface geometry may be necessary. Geysers with deeper bubble traps and greater volume are more likely to have pre-play or minor eruptions. Complexity in the underground geometry determines the features of the eruption cycles.

3.8 Acknowledgments

This research was supported by: National Science Foundation (EAR1114184), CEGA-University of Chile, Conicyt-Chile, Center for Latin American Studies-University of California Berkeley, and the Judy Webb Chair. We thank the El Tatio team who provided essential help in the laboratory and in the field: Fred Murphy, Shaul Hurwitz,

Max Rudolph, Chi-Yuen Wang, Ameeta Patel, Eric King, Angello Negri, Pablo Ortega, Alberto Ardid, Camilo Sanchez, Martin Reich, Cyndi Kelly, Sarah Barrett. The fieldwork was performed with the permission of the Amayras Communities of Caspana and Toconce. Takeshi Matsushima, Jun Oikawa, and Atsushi Watanabe helped us with the tilt measurements. We thank the editors and reviewers for helping to clarify the results and interpretations. Both the data and input files necessary to reproduce the figures are available from the authors upon request (carolimunoz@berkeley.edu; mmanga@berkeley.edu; namiki@hiroshima-u.ac.jp). Any use of trade, firm, or product names is for descriptive purposes only and does not imply endorsement by the University of California or the authors.

3.9 Figures

Figure 3.1: El Tatio Geyser Field
(a) Location (Google Eath, 2015); green stars indicate the positions of the studied geysers and the blue line indicates the normal fault that bounds the El Tatio half-graben, showing that geysers are located in the hanging wall of that fault. (b) El Jefe geyser (EJ) erupting in 2012, (c) Vega Rinconada geyser (VRG) and Vega Rinconada pool (VRP) in 2014, (d) El Cobreloa geyser (CL) is erupting in front, El Cobresal geyser (CS) and the mud pool (MP) steaming in the background in 2014.

Figure 3.2: Eruption cycle of El Jefe geyser (EJ)
(a) Histogram of interval between eruptions (IBE) for data collected in 2012 (Munoz-Saez et al., 2015a), showing a normal distribution with a mean of 132.2 s and standard deviation of 2.4 s. (b) IBE for 2014 with a mean of 105.5 s and standard deviation of 3.2 s. (c) Example of pressure and temperature evolution in 2012 at a depth of 1.5 m (Munoz-Saez et al., 2015a); stars numbered 1 to 7 identify key stages in the cycle. (d) Time series of temperature at depths of 1.7 m (red), 1.2 m (orange), 0.6 m (light blue), and 0.0 m (pink) from 2014; subset of four eruption cycles. (e) Temperature at 1.7 m (red) and 1.2 m (orange), and pressure at 1.7 m (blue), during the same four cycles. The box at right highlights a single eruption cycle, identifying key stages in the cycle defined for 2012 data (panel c).

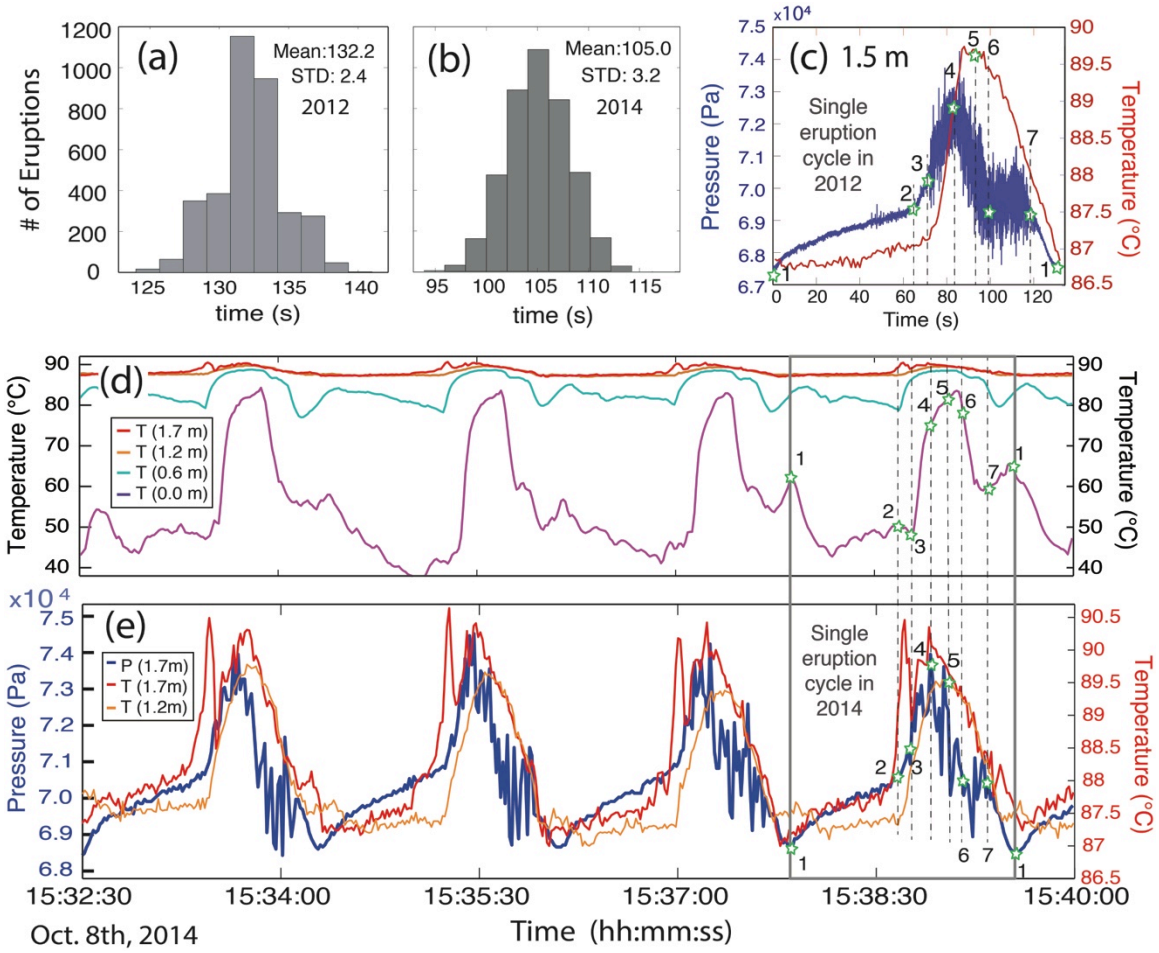

Figure 3.3: Interval between eruptions (IBE) for Vega Rinconada geyser (VRG) (a) Oct. 2012, showing a bimodal distribution centered at 1.4 h and 2.0 h; the mean IBE is 1.4 h and the standard deviation 0.4 h and (b) Oct. 2014, showing an asymmetric distribution, centered at 1.4 h; the mean IBE is 1.5 h and the standard deviation 0.2 h.

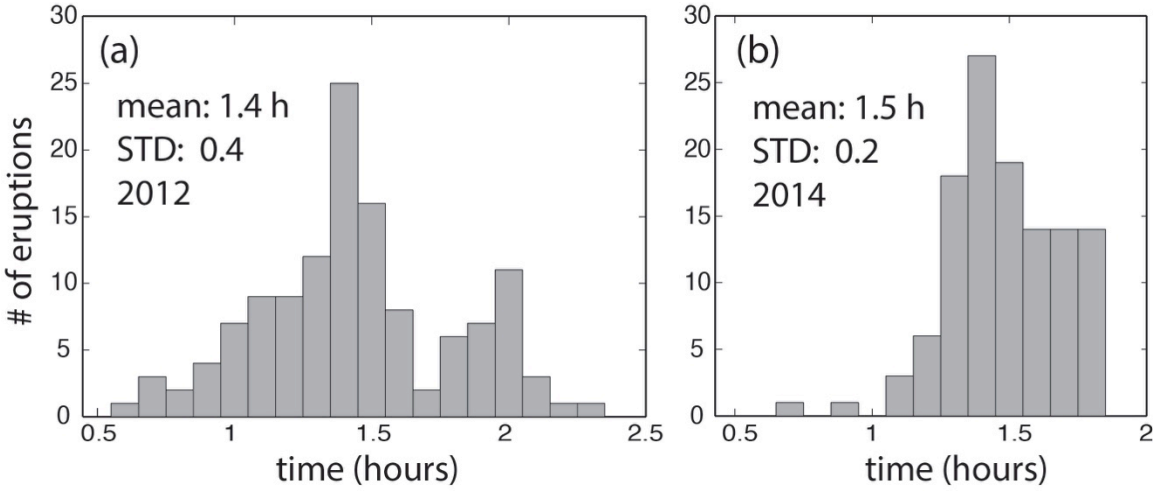

Figure 3.4: Vega Rinconada geyser (VRG) and pool (VRP) in 2014
(a) Right side shows a picture of the geyser surface, where we extract the central pixel for all heights (vertical pink line) for images taken every 1 s to obtain the surface time series shown on the left. White curve shows the liquid water height above the vent. Time interval "A" corresponds to the period of the main eruption, "B" to small discharges of water, and "C" to the increase of water level at the conduit surface measured from the image sequence. (b) 2D color plot of temperature inside the geyser conduit (temperature sensors were located at depths of: 0.0 m, 0.9 m, 1.7 m, 2.6 m, 3.5 m, 4.3 m, 5.2 m, and 6.1 m) and temperature is interpolated between the measurement depths. (c) Time series of pressure (black) and temperature (green) at 4.3 m and 6.1 m (red) depths in the geyser conduit. (d) Time series of pressure (black) and temperature (blue) at 2 m depth in the pool. Time shown for all figures begins on Oct. 5th 2014, 13:22:00 UTC.

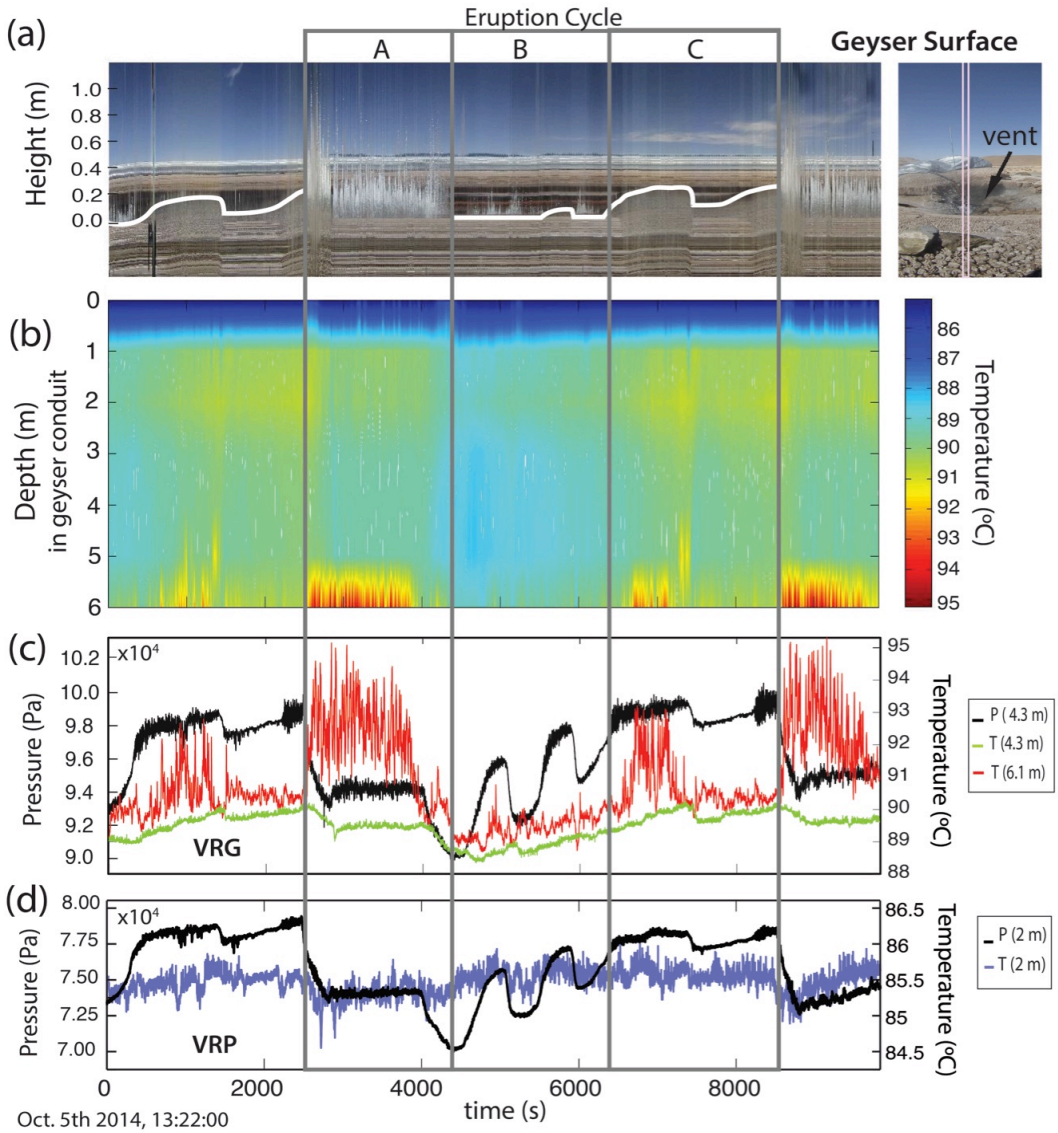

Figure 3.5: Interval between eruptions (IBE) of El Cobreloa geyser (CL) and El Cobresal geyser (CS) during Oct. 2014

(a) For main eruptions in the CL, the IBE distribution is bimodal with peaks at 0.75 h and 2.75 h, the mean IBE is 2.16 h, and the standard deviation is 0.86 h. The IBE is calculated from signals in pressure, temperature and tilt data. (b) The IBE of the CS shows an asymmetric distribution centered at 0.20 h; the mean IBE is 0.26 h and the standard deviation is 0.09 h. IBE is calculated from temperature measurements.

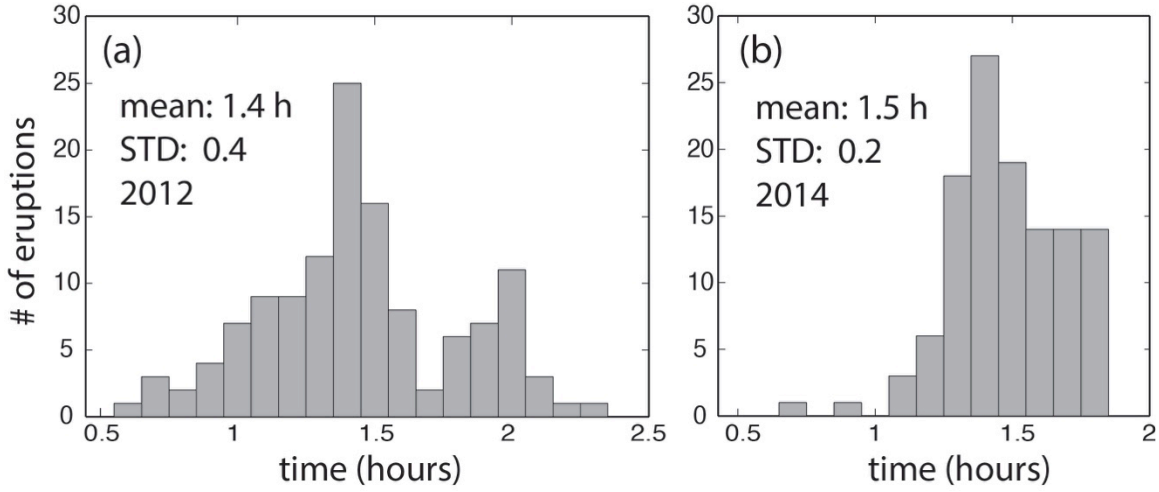

Figure 3.6: El Cobreloa (CL) showing an example of three eruption cycles measured on Oct. 8th, 2014

(a) Temperature at a depth of 1 m in the conduit (red) and horizontal distances of 0.5 m from the vent (purple), and 2.5 m from the vent. (b) Pressure (grey) and temperature (red) from sensors located at a depth of 1 m in the conduit. The black line indicates atmospheric pressure. (c) Ground deformation: tangential component (light blue), and radial component (dark blue). (d) Image sequence taken every 1 s above the geyser conduit, which corresponds to the part of the time series presented in (a) and (b); y-axis indicates the height above the conduit. We observe water coming out of the conduit during minor eruptions (white arrows), and main eruptions (black arrow), also identified in (b).

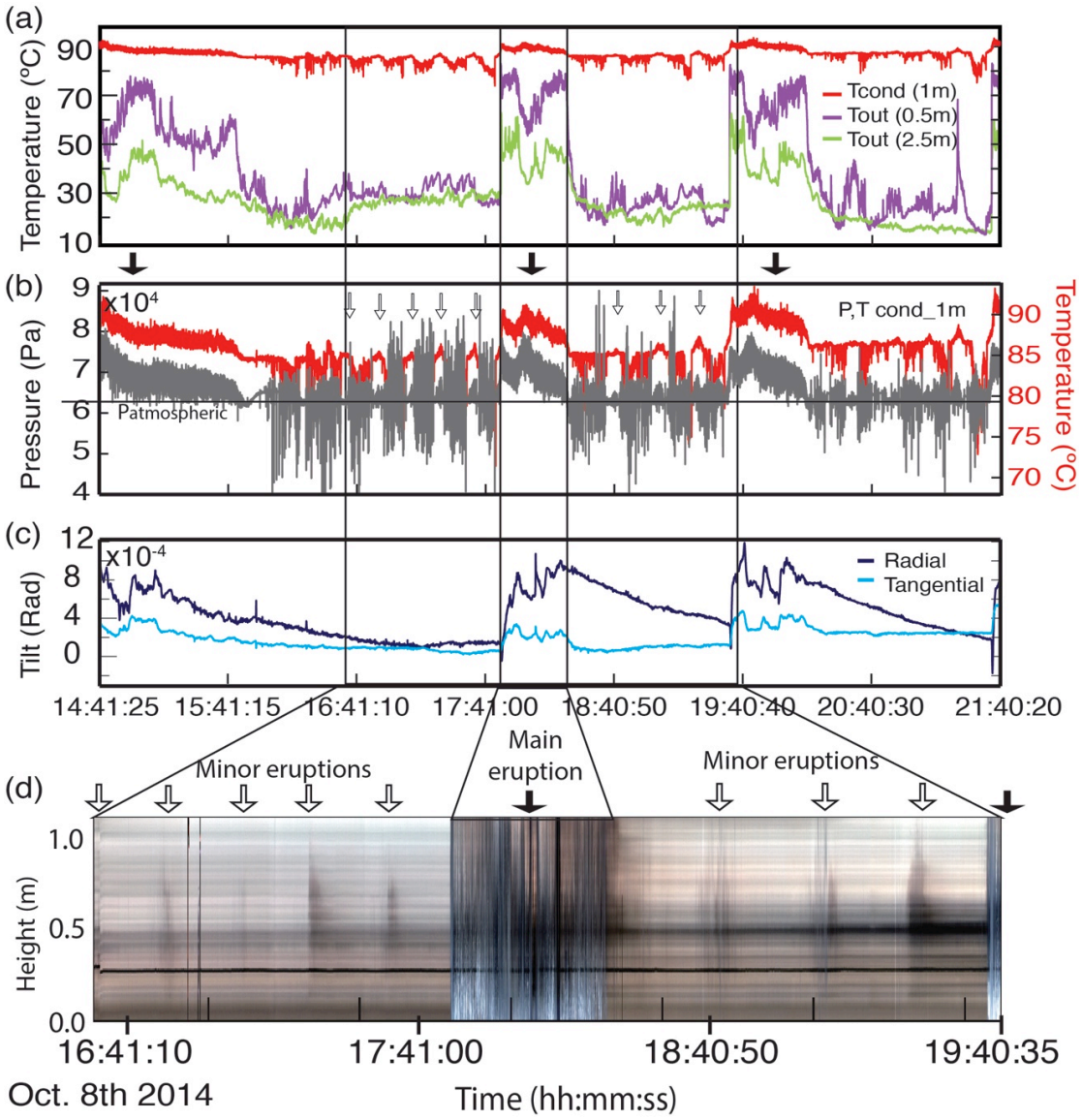

Figure 3.7: El Cobresal (CS) time series in 2014

(a) Temperature in the conduit at depths of 0.0 m (green), 0.4 m (magenta), 0.8 m (yellow), and 1.2 m (red). (b) Images sequence taken every 1 s above the geyser conduit showing five consecutive eruptions (black arrow), followed by a quiet period, and then five more eruptions. Same interval as Figure 3.6.

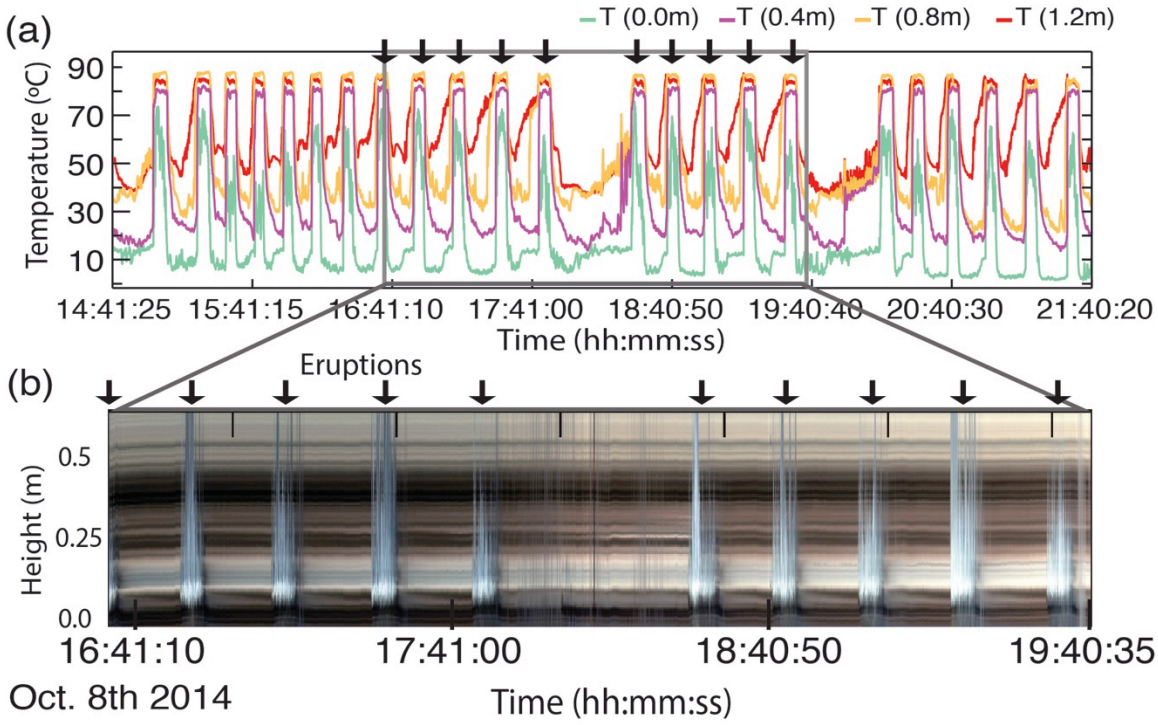

Figure 3.8: Temperature time series from 9 Oct. 2014
Measurements at a depth of 1 m in the crater of the Mud Volcano (MV) shown in green and a depth of 1.2 m in El Cobresal conduit (CS) shown in red.

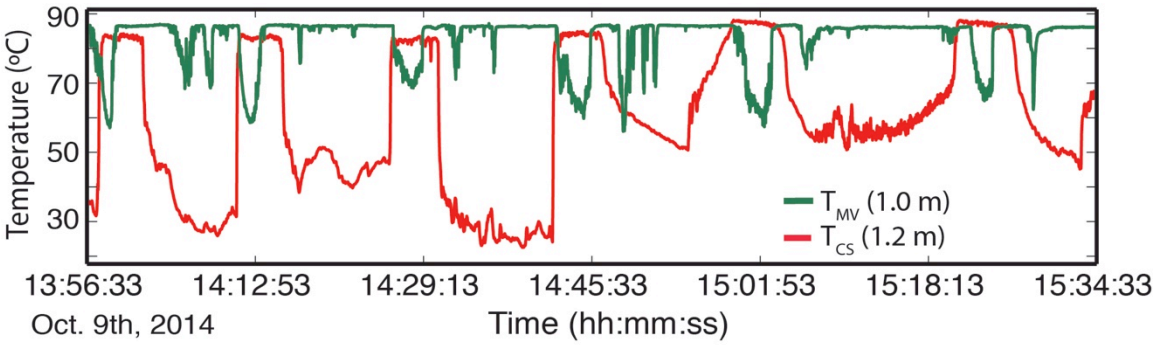

Figure 3.9: Temperature and pressure evolution within the geysers

T, P with the theoretical boiling curve for pure water (red curve). The y-axis has two scales at the left side we express pressure in Pa and at the right side in mm of H_2O. In the purple box we plot data from 4,150 eruptions of el Jefe (EJ) in 2014 at a depth of 1.7 m (pink dots), the black curve is the average during an eruption cycle, and numbers 1 to 7 indicate key points in the eruption cycle. In the green box we plot data from 35 eruptions in 2014 at the primary geyser (CL) at a depth of 1 m (green circles); black ellipses show the quiescent period and the eruptions. Arrows on the left show the values of atmospheric pressure, and the theoretical maximum hydrostatic pressure measured in CL and EJ if the conduit is full of water. The green box shows that the pressure at CL exceeds the hydrostatic value during the main eruptions, but this does not occur for EJ. In the blue boxes we plot data from Vega Rinconada geyser (VRG). In 2014 we measured 118 eruptions, and the sensors were located at depths of 4.3 m and 6.1 m. In 2012 we measured one eruption, and the sensors were located at depths of 4.3 m and 5.9 m. The black curve superimposed on the data shows the average pressure and temperature during one cycle. The letter A shows the evolution during main eruptions, B identifies the first part of the recharge period, and C shows the second half of the recharge period (as observed in Figure 3.4). In the grey box we plot data of Vega Rinconada pool (VRP) from 2012 (light grey) and 2014 (dark grey).

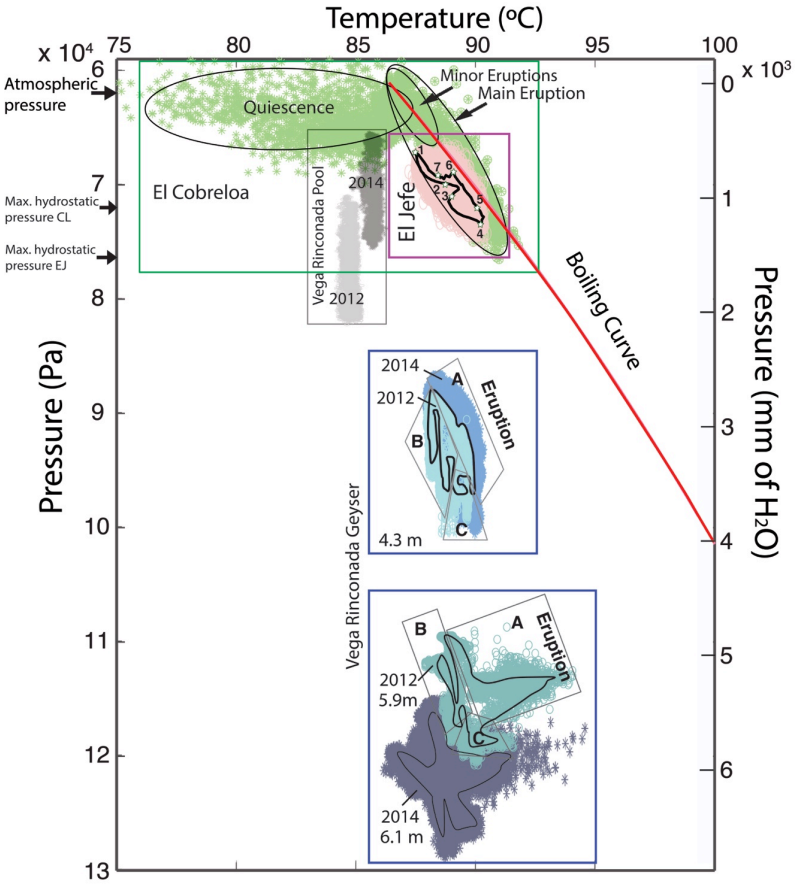

Figure 3.10: Eruption cycle of Vega Rinconada geyser (VRG)
(a) Temperature (red) and pressure (blue) at a 5.9 m depth. Sampling frequency is 1 Hz for temperature, and 100 Hz for pressure. A corresponds to the main eruption, B and C to the recharge. (b) Spectrogram of the pressure during the same period of time. A 3.5 Hz signal occurs before every main eruption, and during every local maximum of pressure during the recharge period. Time shown begins on Oct. 27th 2012, 21:59:50 UTC.

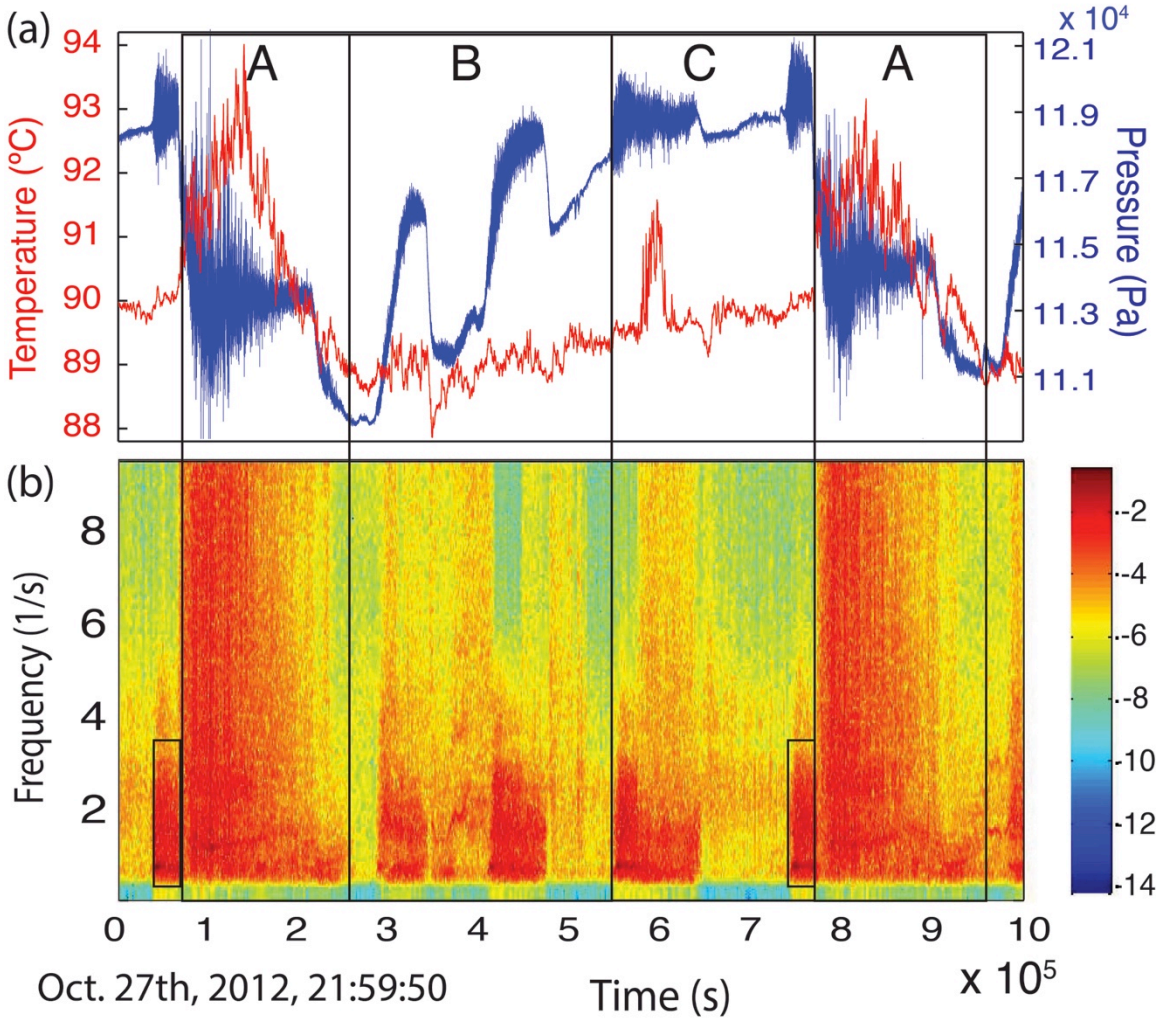

Figure 3.11: Interval Between Eruption (IBE) at Vega Rinconada geyser (VRG) and El Cobreloa geyser (CL)

(a) IBE at different times of the day at VRG. Data from Oct 21st to Oct 29th 2012 are shown with different colors. (b) Temperature in VRG at depths of 0.9 m (dark magenta), 2.6 m (blue), 4.3 m (yellow) and 6.1 m (red). Boxes show five eruption cycles on Oct. 23rd 2012. Numbers from 1 to 4 and the long arrow on the red line ((a) Oct. 23rd) shows the IBE increasing with time as in (b). From 4 to 5 the IBE decreases (short arrow). (c) IBE during the day for CL, data from Oct 6th to Oct 9th 2014. (d) Pressure (blue) and temperature (red) at a depth of 1 m in CL on Oct. 7th 2014. From 1 to 2, and 3 to 4, the arrows in (c) and (d) show a long eruption cycle followed by a short eruption cycle.

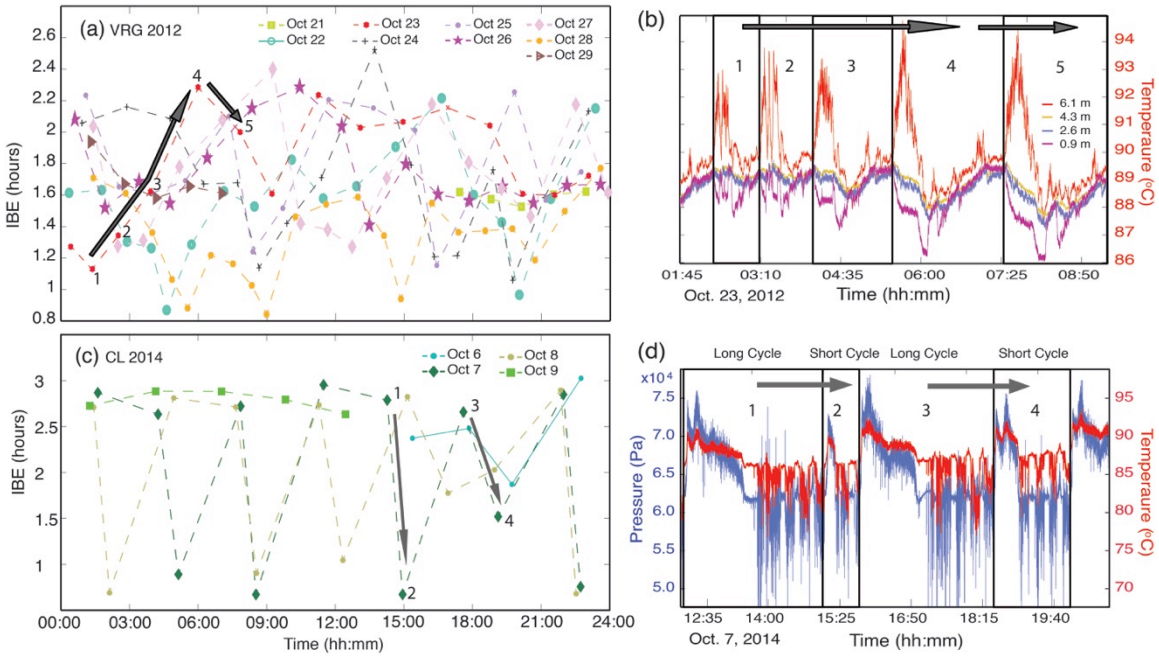

Figure 3.12: Image sequence

Same time period shown in Figures 3.6 and 3.7. (a) El Cobreloa (CL), (b) El Cobresal (CS), (c) Mud volcano (MV). For (a) and (b) pictures were taken facing the water column; in (c) the pictures were taken facing toward the MV vent. Red arrows indicate the eruptions, and the triangle in (c) shows the MV overflowing.

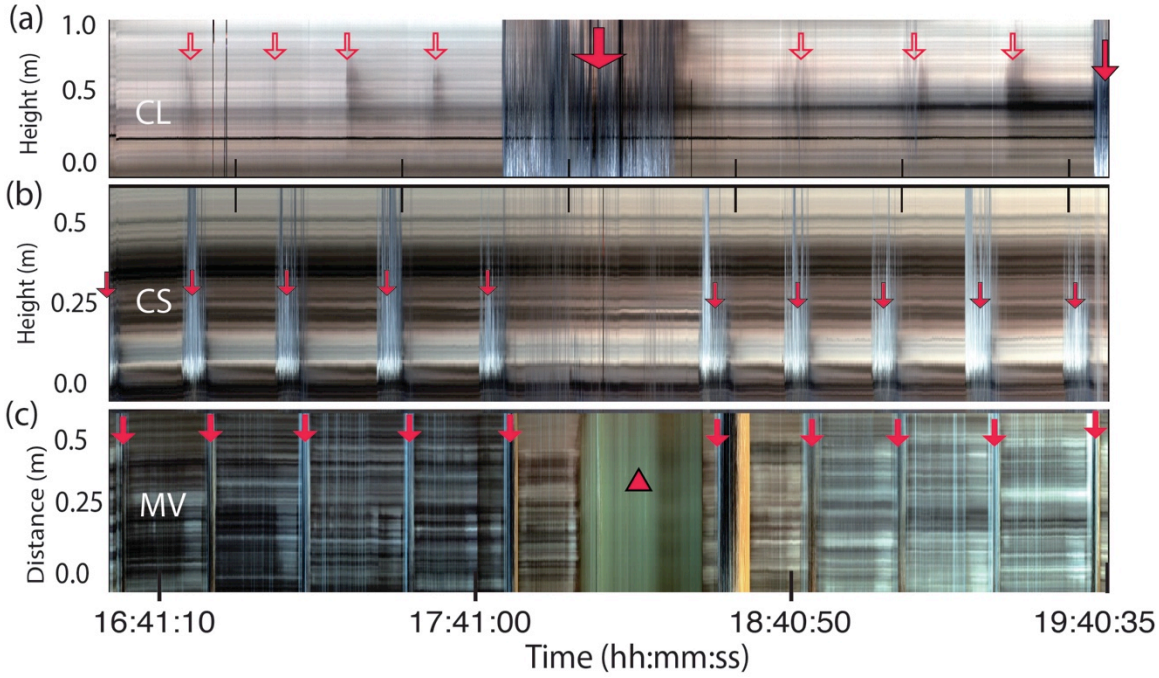

Figure 3.13: Interaction between El Cobreloa geyser (CL) and El Cobresal geyser (CS)

(a) Time series of surface expression of eruptions showing three main eruptions at CL. (b) Time series of temperature (light blue), pressure (grey) of CL at 1 m depth, and temperature in CS at 1.2 m depth (red) during the same time period of (a). Main eruptions of CL are characterized by a large increase of temperature and pressure that correlate with water height in (a). In the time series of CS we numbered each eruption interval sequentially. Number 1 has a large IBE that coincides with a main eruption of the CL. (c) IBE of eruptions at CS geyser during one cycle of the CL as we observe in (b). We observe that the IBE of CS decreases at the beginning of the CL eruption cycle, and then increases over time. (d) IBE of eruptions at CS geyser before the main eruption of CL; number 1 corresponds to the longest cycle, and previous eruptions are numbered sequentially.

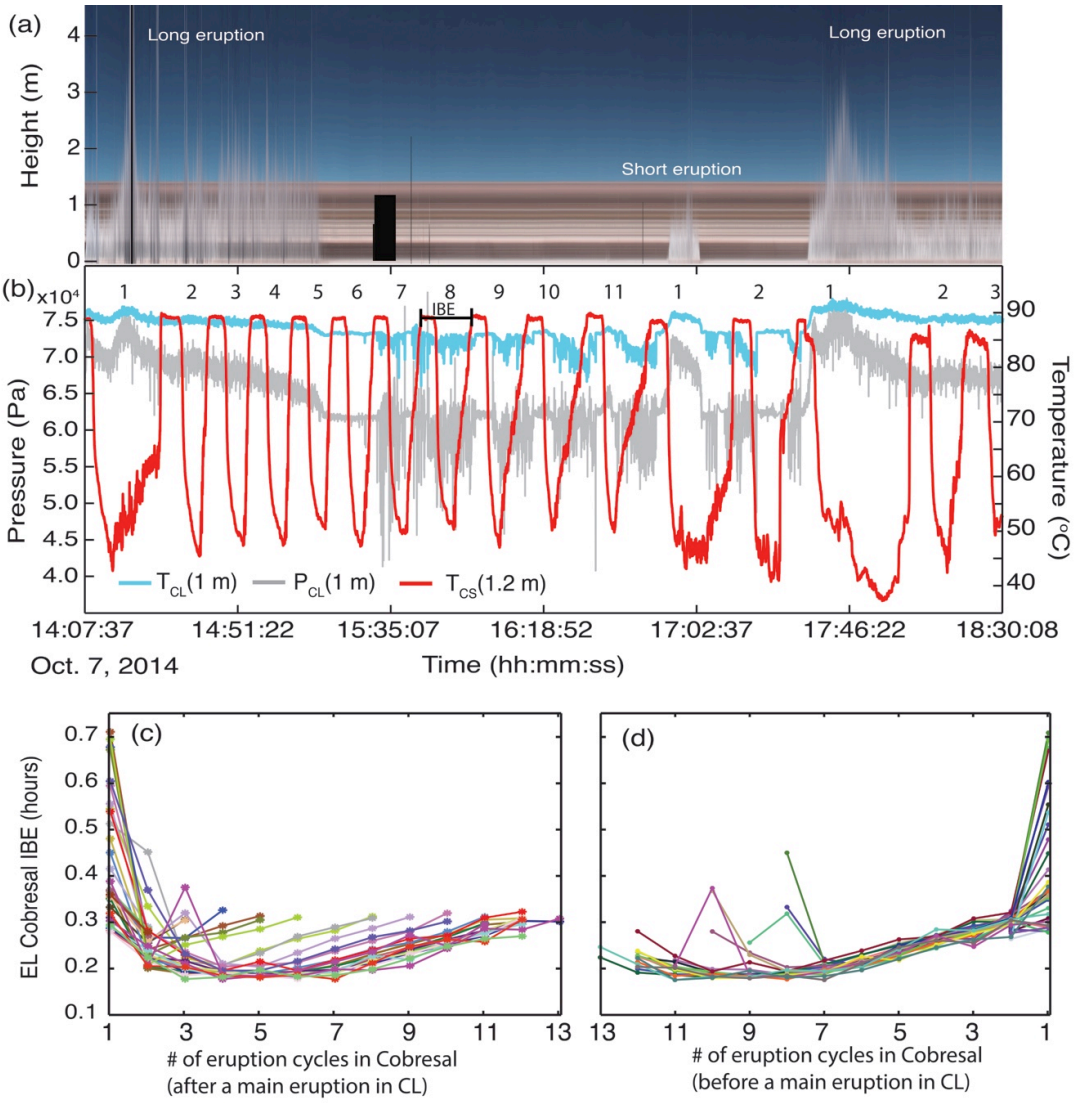
(a)
Height (m)
Long eruption
Long eruption
Short eruption
(b)
x10⁴
Pressure (Pa)
Temperature (°C)
IBE
T_CL(1 m)
P_CL(1 m)
T_CS(1.2 m)
14:07:37
14:51:22
15:35:07
16:18:52
17:02:37
17:46:22
18:30:08
Oct. 7, 2014
Time (hh:mm:ss)
(c)
EL Cobresal IBE (hours)
# of eruption cycles in Cobresal
(after a main eruption in CL)
(d)
# of eruption cycles in Cobresal
(before a main eruption in CL)

Figure 3.14: Conceptual model for the three geyser systems
(a) The isolated geyser, El Jefe (EJ) has a single conduit connected to the bubble trap. Bubbles moving toward the conduit indicated by the arrows generate the eruption. (b) Vega Rinconada, the geyser (VRG) - pool (VRP) system, has two connected conduits, but only the geyser is connected to the bubble trap. Arrows show the direction of fluid flow. (c) El Cobreloa (CL), El Cobresal (CS) and the Mud Volcano (MV) are three conduits connected through a permeable layer or aquifer.

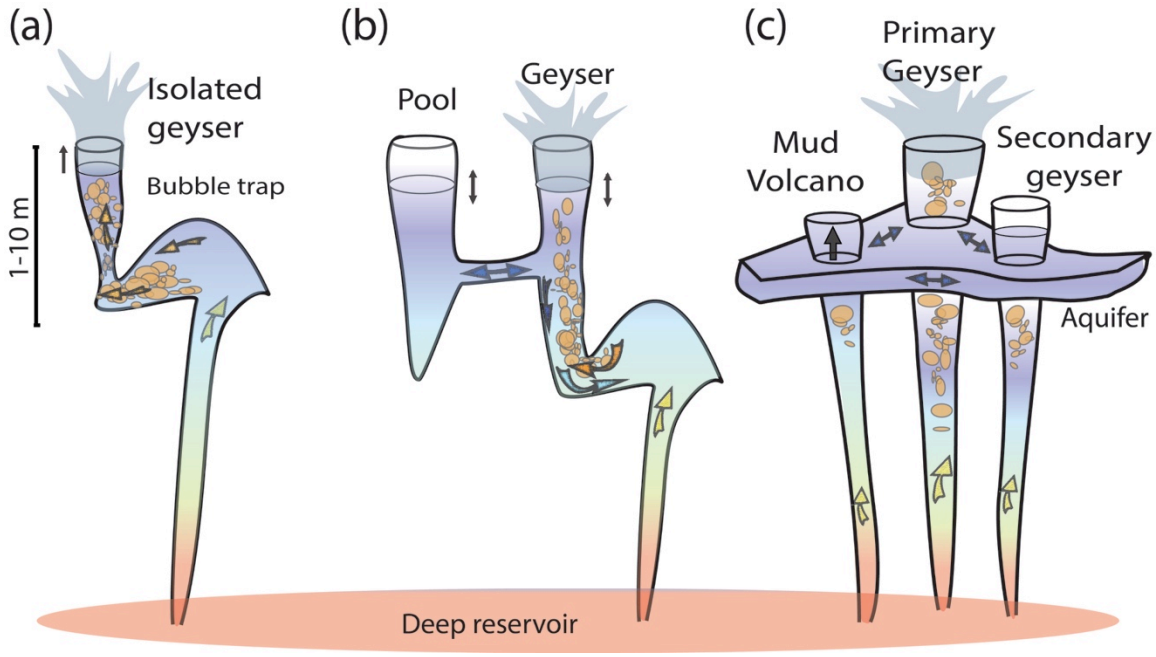

Chapter 4 Physical and hydraulic properties of modern sinter deposits: El Tatio, Atacama

The following chapter includes work previously published in:
Munoz-Saez, C., Saltiel, S., Manga, M., Nguyen, C. and Gonnermann, H., 2016. Physical and hydraulic properties of modern sinter deposits: El Tatio, Atacama. Journal of Volcanology and Geothermal Research, 325, pp.156-168.

4.1 Abstract

Sinters are siliceous, sedimentary deposits that form in geothermal areas. Formation occurs in two steps. Hot water circulates in the subsurface and dissolves silica from the host rock, usually rhyolites. Silica then precipitates after hot water is discharged and cools. Extensive sinter formations are linked to up-flow areas of fluids originating from high temperature (>175°C) deep reservoirs. Fluid geochemistry, microbial communities, and environmental conditions of deposition determine the texture of sinter and pore framework. Porosity strongly influences physical and hydraulic properties of rocks. To better understand the properties controlling the transport of fluids, and interpret geophysical observations in geothermal systems, we studied 17 samples of modern geyserite sinter deposits (<10 ka) from the active El Tatio geothermal field in northern Chile. We measured the physical properties (hydraulic, seismic, and electrical), and internal microstructure (using μX-Ray computed tomography). We find that the pore structure, and thus hydraulic and physical properties, is controlled by the distribution of microbial matter. Based on velocity-porosity relationships, permeability-porosity scaling, and image analysis of the 3D pore structure; we find that the physical and hydraulic properties of sinter more closely resemble those of vesicular volcanic rocks and other material formed by precipitation in geothermal settings (i.e., travertine) than clastic sedimentary rocks.

4.2 Introduction

Sinters are terrestrial, siliceous, sedimentary deposits that are common in geothermal areas with near-neutral alkali chloride springs and typically originate from deep reservoirs with temperatures >175^{o}C (Fournier and Rowe, 1996). Silica can be also deposited from acid-sulfate-chloride waters (e.g. Jones et al., 2000; Mountain et al, 2003; Rodgers et al., 2004; Schinteie et al., 2007). Sinter deposits are located at the surface of geothermal systems; near-vent deposits called geyserite form a thin unit that can reach up

to ~15 m thicknesses, while the thickness of sinter terraces and aprons varies from 10 to 100 m (e.g., Campbell et al., 2015a).

Geophysical methods commonly used to image geothermal settings include seismic, electrical, and radar and hence require knowledge of the seismic velocity, density, and electrical conductivity of sinter to interpret geophysical data. Few studies report physical properties of sinter (e.g., Herdianita et al., 2000; Rodgers et al., 2004; Lynne et al., 2005, 2008), none of which report geophysical properties.

Physical and hydraulic properties of rocks are strongly influenced by their porosity and pore structure. The origin and evolution of sinter porosity have received more attention in the literature; primary porosity can be modified by post-depositional events including burial, compaction, secondary fluid circulation and precipitation of silica in pores, diagenetic transformation of silica, and dissolution via acid steam condensate (e.g., Fernandez-Turiel et al., 2005; Campbell et al., 2015b; Lynne et al., 2008). The evolution of porosity in some cases appears to be independent of mineral maturity (Lynne et al., 2005, 2008). The shape and size of the pores/voids preserved in the sinter layers provide information about the regime of water discharge in channels (Lynne, 2012). Primary porosity in microbial textures occurs in the matrix and inside silicified organisms (Jones and Renaut, 1997; Fernandez-Turiel et al., 2005; Campbell et al., 2015b). Abundant fenestral porosity has been observed in laminae and palisade micro textures (e.g., Konhauser et al., 2001; Fernandez-Turiel et al., 2005). Gas bubbles (<15mm) released by photosynthetic bacteria can be trapped in microbial mats prior to silicification of microbes (e.g., White et al., 1964; Hinman and Lindstrom, 1996; Lynne, 2012). Microbes can overgrow surfaces faster than the deposition rate of silica and produce macro-scale sinter textures of multiple curved laminations with oval or lenticular voids (Lynne, 2012).

To better understand the properties of modern sinter, interpret geophysical surveys and to provide estimates of properties that control the transport of fluids, we analyzed a set of young sinter samples from an active geothermal field located in north of Chile called El Tatio. We sampled proximal to middle facies of modern sinter deposits, and we examined the microstructure, porosity and distribution of microbial filaments in the samples by using optical (thin sections) and μX-Ray Computed Tomography methods. We measured the hydraulic, seismic, and electrical properties of the samples in the laboratory, and compared the measured relation between microstructure and physical properties with commonly used effective medium models and empirical relationships.

4.3 Importance of studying sinter

Depending on the distance from the geothermal vent and the flow regime, proximal, middle and distal deposits have distinctive sinter facies, including cones, mounds, channels, terraces, aprons, and marsh (e.g., Cady and Farmer, 1996; Braunstein and Lowe, 2001; Campbell et al., 2015a). Geyserite is a type of proximal sinter deposit

characterized by dense and fine lamination that is generated by intermittent discharge from hydrothermal vents (White et al., 1964). Proximal deposits are associated with high temperature water, ranging from 75 to 100°C (e.g., White et al, 1964; Walter, 1976a; Campbell et al., 2015a). Sinter, especially proximal deposits, provides a guide for identifying ore epithermal deposits and geothermal systems, These deposits indicate the location of up flow zones, and the position of vents/fractures connected to deep geothermal reservoirs (e.g., Sillitoe, 1993, 2015; Guido and Campbell, 2009; Lynne 2012).

Sinter textures preserve information about the fluid geochemistry, discharge, microbial communities, and environmental conditions of deposition (e.g., Walter, 1976ab; Cady and Farmer, 1996; Hinman and Lindstrom, 1996; Konhauser and Ferris, 1996; Jones and Renaut, 1997, 2004; Campbell et al., 2001; Konhauser et al., 2001; Lowe et al., 2001; Jones et al., 2003; Guidry and Chafetz, 2003; Lynne and Campbell, 2003; Handley et al., 2005; Schinteie et al., 2007; Nicolau et al., 2014). Hot springs settings are inhabited by microbial communities; hence studying sinter can provide insights into the development of early life on Earth under extreme environmental conditions (e.g., Walter, 1972; Konhauser, et al., 2003; Westall et al., 2015). Opaline silica deposits have been identified on Mars (e.g., Squyres et al., 2008; Ruff et al., 2011), and they are of astrobiological interest because terrestrial opaline sinters preserve signatures of microbial life. Microbial textures tend to remain longer than microfossils as fingerprints of organisms, which tend to disappear in ancient sinters (e.g., Guidry and Chafetz, 2003; Lynne et al., 2005). A few pre-Quaternary sinters with microbial fossils have been found in the geological record e.g., Devonian Drummond in Australia (e.g., Walter et al., 1996), Devonian Rhynie cherts in Scotland (e.g., Rice et. al, 2012), Late Jurassic Deseado Massif in Argentina (Guido and Campbell, 2014; Campbell et al., 2015a).

Palisade texture is commonly preserved in the geological record, and it is associated with low-temperature (<40^{o}C) relatively calm water that accumulates in shallow terraces, large pools and distal apron-slope (e.g., Weed, 1889; Walter et al. 1996; Cassie, 1989; Cady and Farmer, 1996; Lynne and Campbell, 2003; Guido and Campbell, 2014; Campbell et al., 2015b). Palisade texture typically has thin laminated layers (1-5 mm thick) that are rich in microbial filaments; these layers alternate with solid silica horizons (e.g., Campbell et al., 2001, 2015b). Filaments arrange into closely packed, vertically-oriented, micropillar structures (e.g., Cassie, 1989; Cady and Farmer, 1996; Lynne and Campbell, 2003). Silicified stacks of filamentous palisade layers can form stromatolitic structures (e.g., Campbell et al., 2001, 2015b). These microbial filaments commonly correspond to photosynthetic cyanobacterias of the genus *Calothrix spp*., which are characterized by individual filaments of >10μm diameter and 4mm length (Watanabe and Kurogi, 1975). Microbial filaments form felted mats. Mid-temperature (~40-60^{o}C) hot spring aprons and discharge channels are inhabited by thin <5μm diameter sheathed filamentous cyanobacteria *Leptolyngbya ssp*. (e.g., Walter, 1976a; Cady and Farmer, 1996; Lowe et al., 2001). High-temperature (60-75°C) proximal slopes and channels are

inhabited by filamentous microbes of <1μm diameter, which are in the limit of photosynthetic bacteria (Pierson and Castenholz, 1974). In near vent environments (>75^{o}C), sinter is deposited under subaqueous conditions and intermittently wetted by splash, waves, surging, or airborne eruptions (e.g., Lowe et al., 2001; Lynne, 2012). Biofilms of non-photosynthetic bacteria and archaea have been recognized in alkaline waters >75 °C (e.g., Bott and Brock, 1969; Huber et al., 1998; Blank et al., 2002; Cady, 2008).

Studying the properties of modern sinters offers insights to discriminate between depositional processes and later overprints. Mineralogical and textural changes in sinter occur gradually over time as a result of burial and diagenesis (e.g., Cady and Farmer, 1996; Herdianita et al. 2000; Lynne et al., 2012). However sinter diagenesis is mostly controlled by burial, circulation of secondary fluids and condensation of acid steam (e.g., Lynne and Campbell 2013; Lynne et al., 2005, 2008). The main phase in fresh sinter is non-crystalline opal A, a hydrated amorphous form of silica. Micro-spheres of opal-A progressively change to nanospheres of opal-A/CT, lose water and crystallize to para-crystalline opal-CT, opal-C, and eventually to quartz (e.g., Chaika and Dvorkin, 1997; Herdianita, et al., 2000; Rodgers and Cressey, 2001; Lynne et al., 2008).

4.4 El Tatio: geological setting and characteristics of sinter deposits

El Tatio is an active geothermal area located in the Atacama Desert, northern Chile (elevation >4,000 m). The heat of the system is provided by Holocene dominantly andesitic stratovolcanoes with no historical local eruptions (Lahsen, 1976ab). Based on chemical and isotopic characteristics, the thermal waters are inferred to originate from mixing between magmatic, meteoric and hydrothermal sources (Cusicanqui et al., 1976; Giggenbach, 1978; Cortecci et al., 2005; Tassi et al., 2010). The thermal water has pH from 6 to 8, conductivity of ~20 mS/cm, high concentrations of Cl^- (>6000 mg/l), Na^+ (>3500 mg/l), SiO_2 (>220 mg/l), and As^{3-}(>30 mg/l), and low SO^{4-} (<50 mg/l) (e.g., Cusicanqui et al., 1976; Giggenbach, 1978; Fernandez-Turiel et al., 2005; Cortecci et al., 2005 ; Tassi et al., 2010; Nicolau et al., 2014).

Most thermal manifestations are located in an area ~10 km^2, and the distribution of the thermal features is bounded by a N-S trending half-graben (Figure 1). The basin is filled with ~1000 m of sub-horizontal ignimbrites, tuffs and lavas and covered by Holocene alluvial, glacial (Healy, 1974; Lahsen and Trujillo, 1975) and sinter deposits. Diverse thermal features have been reported, including geysers, springs, perpetual spouters, mud pools, mud volcanoes, and fumaroles (Glennon and Pfaff, 2003). Sinter deposits form an array of mounds, geyser cones, pool-rim dams, and complex sinter aprons characterized by shallow terraced pools (Jones and Renaut, 1997). The absolute age of the sinter deposits is unknown, a bound of <10 ka can be constrained by the time of the last glacier retreat considering the glacial deposits below the sinter units (Lahsen,

1976ab). However, considering the rates of silica precipitation and the size of the deposit, deposition would likely have begun ~1 to 4 ka (Nicolau et al., 2014).
A precipitation rate of silica between 1.3 to 3.4 kg/m^2 per year was measured in-situ for sub-aerial sinter that accumulated during 10 months along different portions of the discharge channel of a hot spring (Nicolau et al., 2014). This rate is lower than in Waiotapu, New Zealand, where the sub-aerial precipitation is 1 to 10 kg/m^2 (Handley et al., 2005), but relatively high considering that the silica content of the water in the measured springs of El Tatio (147 ppm) is lower than in Waiotapu (430ppm). Silica deposition is governed by environmental conditions leading to high evaporation rate and high cooling rate (Nicolau et al., 2014).

Previous studies of sinter at El Tatio explained some petrographic, chemical, and textural characteristic of sinter, describing opal-A as the dominant silica phase, with halite and gypsum as accessory minerals (e.g., Jones and Renaut 1997; Rodgers et al., 2002; Glennon and Pfaff, 2003; Fernandez-Turiel et al., 2005; García-Valles et al., 2008; Lynne, 2012; Nicolau et al., 2014). Mineralogically mature opal-C is mostly located in older distal depositional environments and near active fumaroles (García-Valles et al., 2008). Sinter deposits preserve microbial communities of cyanobacteria, green bacteria, diatoms, and particles of silicified pollen and plants in their layering (Fernandez-Turiel et al. 2005; García-Valles et al., 2008; Nicolau et al., 2014). The high elevation of El Tatio lowers the boiling point of water to ~86.4^{o}C, and leads to higher UV radiation than at other sinter areas, e.g., Yellowstone in the USA, hot springs in New Zealand and Iceland. Precipitation of silica offers cyanobacteria protection against UV radiation (Phoenix et al., 2006). Compared to low the altitude hot springs in New Zealand, the El Tatio microbial mats have similar color and texture, but slightly higher temperatures (Lynne et al., 2012). Proximal to geysers (70 to 86^{o}C) are green bacteria that were observed at Yellowstone in waters below 75^{o}C (Fernandez-Turiel et al., 2005). Ranges of temperature for hyperthermic and mid-temperature microbes at El Tatio were not strictly defined (e.g., Phoenix et al., 2006; Nicolau et al., 2014). Hyperthermophilic bacteria (1μm diameter) and mid-temperature microbes (>5μm diameter) coexist with boiling-related textures and proximal environments of >60^{o}C (Nicolau et al., 2014). Filamentous cyanobacteria *Lyngbya ssp.* (<5μm diameter), *Calothrix ssp.* (>10μm diameter), and *Phormidium ssp.* (2-12μm diameter), were identified from microbial mats collected in outflow channels and terraces of <40^{o}C (Phoenix et al., 2006).

At El Tatio, geysers and spouting springs discharge from tube-shaped vents that can be surrounded by steep-sided mounds or cones up to ~3 m high and ~3 m in basal diameter, or by pools (few cm up to 5m diameter) filled with hot water, and bounded by pool-rim dams (Jones and Renaut, 1997). Deposits present irregular shapes and discontinuous laminations, smooth knobs and ridges, columns, erected spicules, and oncoids (Jones and Renaut, 1997; Fernandez-Turiel et al., 2005; García-Valles et al., 2008; Nicolau et al., 2014). Strong daily variations in temperatures produced freezing-related textures: platelets, micro columns and ridges (Nicolau et al., 2014).

Microscopically, silica spheres can be randomly aggregated forming layers or botryoidal crusts; massive silica forms smooth-dense layers; and biogenic silica forms porous sinter laminations (Fernandez-Turiel et al., 2005; García-Valles et al., 2008; Nicolau et al., 2014). Middle facies associated with discharge channels, elevated sinter terraces around springs and geysers, and mid-apron have macro-scale textures characterized by laminated spicules and oncoids of varied shape (Jones and Renaut, 1997; Fernandez-Turiel et al., 2005; García-Valles et al., 2008). Micro-scale textures show fine laminations alternating with palisade textures (Jones and Renaut, 1997; Fernandez-Turiel et al., 2005).

4.5 Methodology

We collected samples from three locations: TAT-002, TAT-005 and TAT-006 (Figure 4.1). TAT-002 is a sinter terrace formed by the discharge of an active geyser located 5 m from the sample site. This sample was still saturated with water, and the temperature was ~40 °C when collected. TAT-005 and TAT-006 are abandoned geyser cones, and samples were dry. TAT-005 is located in an area without discharge of thermal fluids, while at TAT-006 vapor was still emanating from the center of the cone. Cores derived from samples collected from different stratigraphic levels were sampled systematically from the bottom of the cone to the top every 5 to 10 cm, and labeled alphabetically in the same order. We assume that samples from the bottom were older than samples from the top. Measurements were performed only in samples of fine-layered sinter (1 to 5 mm laminations).

For the petrography, we analyzed thin sections of the three sampled sites with a petrographic microscope. We analyzed 2.5 mm diameter cores from sample TAT-002 with μX-ray computed micro-tomography (μXRT), which is a non-destructive technique that creates a high-resolution three-dimensional image of rock density (resolution of 1.3 μm/voxel). μXRT was performed at the Advanced Light Source (ALS) beamline 8.3.2, Lawrence Berkeley National Laboratory (LBNL). We used 22 keV monochromatic X-rays. We reconstructed and visualized the 3-D internal structure of the sample using Octopus, Image-J and Avizo software.

For X-ray diffraction (XRD), considering that sinter diagenesis can be patchy spatially and layers can be heterogeneous in composition, we powdered different sinter layers from the hand sample, mixed them and analyzed a few milligrams. We used a PANalytical X'Pert Pro diffractometer equipped with a Co X-ray tube and a fast X'Celerator detector. Minerals produce characteristic X-ray patterns that can be compared with a database of known phases using the analytical software XPERT-PRO.
For hydraulic, seismic and electrical properties analysis, we drilled 17 cores 2.5 cm in diameter. Some of the cores were perpendicular, and others orthogonal, to the lamination. The connected porosity was determined in the lab using a Micromeritics AccuPyc II 1340 (Nguyen et al., 2014) that measures the change of helium pressure within the calibrated

volume and Boyle's law. Powdered samples were also measured using the AccuPyc II 1340© to determine the density of the skeleton (solid plus any isolated vesicles that are not somehow connected to the sample surface). We computed the total porosity by dividing the difference between the volume of skeleton and the volume of the cylindrical core by the total volume of the core. Bulk density of the core was determined from the ratio between the total mass and volume of the core.

For Darcian permeability measurements we used a Capillary Flow Porometer (Model CFP-1100AXL-AC, Porous Media, Inc.). We jacketed the cores with impermeable epoxy resin, except at the two flat ends. The inlet air pressure varied from $1.1x10^5$ Pa up to $6x10^5$ Pa while the outlet pressure was atmospheric. We measured each sample with 2-3 interchangeable flow meters to improve accuracy. The pressure gradient across the sample length varied between 0 and $5x10^5$ Pa m^{-1}, and the measured volumetric flow rate of air was between $3x10^{-3}$ and $5x10^{-7}$ m^3 s^{-1}, with an accuracy ~ $5x10^{-8}$ m^3 s^{-1} (~ 1% of the minimum measured flow rate).

For the measurement of seismic velocities we used ultrasonic waves. We used Source/Receiver NER P and S wave transducers and an oscilloscope, Tektronix TDS 210. A sonic pulse is generated at one side of the sample and we measure the arrival time of the wave in the other end of the sample. We obtained the acoustic velocities by measuring the travel time (minus the 'face to face' time in the transducers themselves) along the sample axis divided by the sample length. When the signal exceeded a threshold, we manually selected this point as the arrival time of the wave. We calculate P-wave velocity (V_P) in dry and saturated samples, given that the deposition of the sinter occurs in an aqueous environment, and the pore space in geothermal reservoirs is saturated. Saturation also minimizes the effect of small cracks in the rocks that may affect the measurements. We used two methods to saturate the sample: vacuum chamber and boiling; we obtained >80% of saturation in every sample. S-wave velocity (V_S) was only measured in dry samples, since the fluid should not affect the shear modulus of the samples. To test the anisotropy of the samples, we measured the S-wave velocity in two perpendicular directions of polarization. For V_P and V_S we used MHz frequencies, and the error in velocity is < 3%. Some samples were too attenuating at these frequencies to make an accurate measurement; they were excluded from this study. The elastic moduli of the rocks were calculated with the seismic velocities and the bulk density of the samples. There are no laboratory standards for the seismic properties of opal-A in sinter rocks in the literature. As a reference, we used standard values of opal measured in the lab on marine chalks with opal-A as the main mineral phase, and less than 50% of opal A/CT (Chaika and Dvorkin, 1997; Chaika, 1998).

We measured the electrical resistance of the saturated samples by connecting an electrode to each end of the core and applying an oscillating electrical current. The resistivity was calculated by measuring the voltage across the sample of a measured length, given the applied current with a range of frequencies from 0.1 to 1000 Hz. The measured resistivity varied at the lower frequencies (due to surface conduction effects)

but became constant at higher frequencies; we report the latter value. We used an IET RS-200W, with an accuracy, after subtracting the residual impedance, of ~0.2%. We measured the resistivity of the samples saturated (R_{rock}) with two brines of different resistivity, R_{w1}=41.35 Ωm, R_{w2}=15.81 Ωm. We expected the lower resistivity of the second brine to lessen the effect of partial saturation because aqueous conduction should dominate over mineral surface conduction, which is more sensitive to saturation. Also the resistivity of R_{w2} is close to the corresponding values of conductivity and salinity of water reported in the field (e.g., Giggenbach, 1978; Cortecci et al., 2005). The resistivity of the brines was used to determine the resistivity index or formation factor (F_R) that corresponds to the ratio between the resistivity of the saturated sample and the resistivity of the water saturating the rock ($F_R = R_{rock}/R_{water}$) (Archie, 1942).

4.6 Results

4.6.1 Observations of sinter layers and pores structure

In thin sections, we observe that El Tatio samples are composed of diverse silica layers, with a variable pore concentration, size, and shape (Figure 4.2). Sample TAT-002 has a palisade texture, with elongated pores perpendicular to the lamination (Figure 4.2abc). In older cones (TAT-005 and TAT-006), we observe palisade-like textures, with a similar orientation of the pores, but they have a smaller amount of voids, and these voids are much more rounded (Figure 4.2eg). We find layers of different textures, including palisade-like textures (Figure 4.2e), massive silica (Figure 4.2h), and porous silica (Figure 4.2di). The boundaries between layers vary: in places we observe sharp changes in texture (Figure 4.2dh) and in others we find transitional changes (Figure 4.2bi). Dark lines delimit different layers (e.g., Figure 4.2g), and fragments of volcanic rocks or glass shards (Figure 4.2f) were deposited between layers. Fragments of sub-angular glass shards provide evidence of subaerial exposure between depositional periods, evidence of geyser quiescence.

We find filamentous microbes in the palisade texture described above for the young sample TAT-002. From the thin sections and 3D reconstructions from μX-ray computed tomography (Figure 4.3), we observe that filaments have diameters ~10 μm. Filaments tend to be oriented perpendicular to the lamination. Some filaments are long and cross through the entire core diameter (2.5 mm). The pores are also elongated in the same direction as the filaments. Using our 3D image volumes, we calculate that the filamentous bacteria surpass 20% of the volume of the rock.

Additionally, in the older samples we observe oncoid structures of ~2 mm diameter, surrounded by porous silica (TAT-005I, Figure 4.4a). Oncoids have concentric massive layers of silica, while the surrounding porous silica have a palisade texture. The dark regions around the pores can be attributed to microbial filaments. In sample TAT-006Q we find wavy laminated textures (Figure 4.4b) with fenestral porosity between the

laminae. From detailed observations inside the pores of sample TAT-006H, we can establish that glassy silica precipitated from the border to the center of the pores (Figure 4.4c). Crystals of hornblende ($Ca_2(Mg, Fe, Al)_5(Al, Si)_8O_{22}(OH)_2$) infill pores (Figure 4.4d).

XRD from different levels of TAT-006 (Figure 4.4e) indicate the predominance of non-crystalline opal-A, and the peaks show the presence of detritial accessory minerals. TAT-006A present several small diffraction peaks, the one at 31° is associated with quartz (SiO_2), and the one at 32.7° with plagioclase, probably albite ($Na(Si_3Al)O_8$). TAT-006I shows diffraction peaks at 25.6° and 33.3° from cristobalite (polymorph of quartz), 31° and 42.9° from quartz, and 32.5° and 32.7° from plagioclase. TAT-006M has the same peaks for cristobalite, quartz, plagioclase, and peaks at 31.5° and 41.6° from zircon ($ZrSiO_4$).

Using μXRT-3D image analysis (Figure 4.5), we estimate that the porosity varies among cores from ~20% to 50%, with slightly lower values for the smaller cores because we did not sample the larger voids. The size distribution analysis of individual pores (diameter >5 μm) show that more 85% of the pores had a volume $<10^5$ μm^3, but their contribution to the total porosity is <5%. Pores with volume between 10^5 and 10^6 μm^3 account for ~ 10% of the pores, and ~15% of the total porosity. The rest of the pores with volume $>10^6$ μm^3 correspond to 0.5% of the number of pores and ~80% of the total porosity.

4.6.2 Hydraulic, seismic, and electrical properties

Table 1 summarizes the measurements of bulk density (ρ), porosity (ϕ), permeability (k), seismic velocities (V_P and V_S) and formation resistivity factor (F_R) of the sinter samples. The propagation velocities of P-waves in dry and saturated samples are denoted V_{PDry} and V_{PSat}, respectively. The two polarization directions of S-waves are denoted as V_{S1} and V_{S2}. The formation resistivity factors (F_{R1} and F_{R2}) were measured with two brines. The cores are also labeled according to whether they were oriented parallel (//) or orthogonal (⊥) to the lamination.

4.6.3 Relationships between porosity (ϕ) and permeability (k)

The total porosity (ϕ_{Tot}) ranges between 25.8 and 54.1%, and the mean porosity is 39.4%, with most of the porosity connected (ϕ_{Conn}) (Figure 4.6a). The values of permeability (k) range between 10^{-15} to 10^{-12} m^2, with a mean k of 10^{-13} m^2 (Figure 4.6b), showing a slight positive correlation with porosity. The highest value of k was measured in a core parallel to the layering (TAT-006LC). Some samples were cored parallel and perpendicular to the layering. k in the parallel cores was 1 to 2 orders of magnitude higher (TAT-006I and TAT-006L) than in the orthogonal cores. In other samples, two

orthogonal cores were analyzed, and *k* varied up to 2 orders of magnitude (TAT-006M) (Table 1).

4.6.4 Anisotropy of S-wave propagation (V_S)

We analyzed the anisotropy of S-wave velocity with the ratio V_{S1}/V_{S2}, where the faster direction is 1 such that the ratio was always greater than or equal to 1 (Figure 4.7a). For samples oriented parallel to the lamination, the two polarizations were different relative to the layering. High V_{S1}/V_{S2} indicates that the layers have different seismic properties, or are seismically anisotropic. For orthogonal samples, both polarizations sample the same layers. High V_{S1}/V_{S2} suggests that the layers themselves are anisotropic. For most of the samples V_{S1}/V_{S2} is close to 1, indicating that most of the samples are isotropic. For those samples where V_{S1}/V_{S2} is far from 1, there is no clear relationship with respect to orientation of the samples.

4.6.5 Relationships between seismic velocities V_P, V_S, porosity (ϕ), and bulk density (ρ)

Seismic velocities show large scatter, with low to medium coefficients of correlation in typical linear empirical relationships (Figure 4.7bcde). This may be due to highly compliant open cracks or grain boundaries (Mavko et al, 1998), which are more prevalent in some of the samples.

P-wave velocities measured in dry samples (V_{PDry}) are more variable than water-saturated samples, and V_{PSat} shows a better correlation coefficient with total porosity (ϕ) (Figure 4.7b). S-wave velocities show large scatter, and poor correlation with total porosity (ϕ) (Figure 4.7c). The relation between the seismic velocities in dry samples, V_{PDry} and V_S (Figure 4.7d), show a moderate correlation. V_{PSat} and bulk density (ρ) are also moderately correlated (Figure 4.7e).

4.6.6 Critical porosity (ϕ_C)

Most porous materials have a critical porosity (ϕ_C) that separates their behavior in two domains: (1) $\phi_{Tot} < \phi_C$ is the load-bearing domain where the solid supports the rock, (2) $\phi_{Tot} > \phi_C$ is the suspension domain, where the solids are in suspension. In the load-bearing domain, seismic velocities range between the mineral (zero porosity) and the suspension value at ϕ_C, and this dependence can be characterized by the relationship between ρV^2 and ϕ (Nur et al., 1991, 1995, 1998). From our sinter samples, we

estimated ϕ_C~71% (Figure 4.8a). When $\phi_0 = 0$, the values ρV_P^2 and ρV_S^2 correspond to the elastic moduli of the mineral: P-wave modulus (*M*) and S-wave or shear modulus (*G*), respectively. From the linear regression of ρV_{PSat}^2 vs. ϕ_{Tot}, we obtain that *M* is 41.6 GPa for the saturated rock and 34.5 GPa for the dry rock, and *G* is 13.6 GPa. Given the great scatter of the seismic velocities, the values of *M* and *G* have large uncertainties.

4.6.7 Effective medium model and the effects of inclusion shape

Effective medium models describe the macroscopic properties, such as elastic moduli, of a solid with inclusions of a different phase. Through a self-consistent approximation, the model uses the analytical solution for a single inclusion, then iteratively solves for the moduli of the background mixture, incorporating interactions between inclusions (O'Connell and Budiansky, 1974). The model of Kuster and Toksoz (1974) uses this self-consistent approximation to calculate V_P and V_S for a range of porosities (density of inclusions) depending on the shape of the inclusions (Appendix). We identify inclusions as pores filled with water. Using ellipsoidal penny-shaped cracks (Berryman, 1980), we estimate a range of possible of pore shapes (parameterized by aspect ratio α = semi-minor axis/semi-major axis) that fit our sinter data. We calculate the model considering the properties for the two extremes cases of minerals in sinter: opal and quartz (Figure 4.8c, and Appendix). For opal, the implied aspect ratio (α) ranges between 0.2 and 0.8. For quartz, the aspect ratio is lower and has a smaller range of possibilities (from 0.09 to 0.11).

4.6.8 Empirical relation between resistivity (F_R) and porosity (ϕ)

The formation factor is an intrinsic property of the rock (independent of the conductivity of the fluid), related to the efficiency of water-filled paths in conducting electrical currents through the medium. Electrical properties of a rock depend on the pore geometry and fluid distribution. Archie (1942) found an empirical power law relationship between the electrical properties (F_R), and the porosity (ϕ) of the rocks in sandstone reservoirs ($F_R = a\,\phi^{-m}$), where the *m* is the cementation exponent and is usually close to 2 for consolidated rocks, and *a* is the tortuosity factor generally close to 1, assuming fully saturated conditions. For the sinter, both measurements of F_R roughly show a power law relationship with porosity (Figure 4.9). For the fit with the more resistive brine, the F_{R1}, the cementation exponent *m* is -1.9 and the tortuosity factor a is 0.71, while for the less resistive brine, F_{R2}, the fit of the exponent and factor increases to -2.44 and 0.79 respectively. Considering the data from both brines, the cementation exponent *m* is -2.16 and the tortuosity factor a is 0.75.

4.7 Discussion

In our samples, we observe silica around filamentous material forming palisade fabric, and porous and massive silica layers without biogenic components (Figures 4.2, 4.3 and 4.4) similar to sinter textures described previously in El Tatio (Jones and Renaut, 1997; Fernandez-Turiel et al., 2005; García-Valles et al., 2008; Nicolau et al., 2014). In sample TAT-002, we observe that silica and pores are elongated parallel to the bacteria (Figure 4.3). Some levels of the older cones TAT-005 and TAT-006 preserve similar pore structures, even though direct evidence of bacteria are unclear (Figures 4.2 and 4.4), probably due to the complete replacement of cellular material by silica (Westall et al., 1995, 2000). Similar pore frameworks have been described for palisade textures in low temperature environments and near vent-sinter (e.g., Lowe et al., 2001; Fernandez-Turiel et al., 2005; Campbell et al., 2001). We conjecture that bacterial filaments determine the pore structure in the rock, however the presence of biological material does not determine the origin of the silica precipitation. Microorganisms can provide a favorable substrate for opaline silica precipitation (e.g., Cady and Farmer, 1996; Jones and Renaut, 1996, 1997; Renaut et al., 1999). Thus silicification around microbial material produces a structural fabric that characterizes some sinter textures (Campbell et al., 2015ab). However, some studies indicate that silica precipitation is largely abiogenic due to cooling and evaporation (e.g., Walter, 1976a; Braunstein and Lowe, 2001; Guidry and Chafetz, 2003), and cyanobacterial surfaces have a negligible effect on silica nucleation (e.g., Yee et al. 2003; Benning et al., 2004; Handley et al. 2005). μX-Ray allow us to isolate and quantify the volume and shape of the silica matrix, bacterial material not replaced by silica, and isolated pores (Figures 4.3 and 4.4). Sinter textures, including pore framework, can survive beyond fossilization, and can potentially be explored with this method.

Even though our measurements were restricted to the finer and most homogeneous sinter layers, we find that the physical properties and empirical relationships have large scatter. Observed microstructures show heterogeneities in different layers and within single layers, with respect to pore size and shape, and the extent to which pores have been infilled. The total porosity of our samples varied between 25 to 56%. Previous studies on young sinter, phase opal-A dominant, reported a similar porosity range of 10 to 60% for samples from New Zealand estimated to be < 2 ka (Herdianita et al., 2000), and lower values < 20% of porosity for samples from Opal Mouth, USA dated by ^{14}C at ~1.9 ka (Lynne et al., 2005), and < 25% at Steamboat, USA, whose youngest ^{14}C age was ~6,283 $\pm$ 60 years BP (Lynne et al., 2008). Even though, the absolute age of El Tatio samples is unknown, the youngest sample (TAT-002) has the highest porosity compared with the samples collected closest to the bottom of extinct cones (TAT-005D and TAT-006A). The shape of the individual pores changed from elongated in the younger sample (TAT-002) to more rounded in the older samples (TAT-

005 and TAT-006). There was no extensive evidence of dissolution, burial, compaction or diagenesis. For samples exposed longer at the surface, the reduction of porosity and shape change can be attributed to secondary precipitation of silica within the pores.

Petro-physical properties of the rocks depend on the lithology and the texture of the rock, including grain sorting and shape of voids (Mavko et al., 1998). Bulk density of the rock (ρ) is closely related to porosity by $\rho = (1 - \phi)\rho_o + \phi\rho_{fl}$, where ρ_o is the density of the mineral, and ρ_{fl} is the density of the fluid (water). Here we infer a mineral density of 2.18 g/cm^3. The measured density of opal-A particles in sinter range between 1.5 and 2.2 g/cm^3 (Herdianita et al., 2000; Lynne et al., 2005, 2008), and in chalk reached 2 g/cm^3 (Chaika, 1998). Denser accessory minerals like quartz (2.65 g/cm^3) and cristobalite (2.33 g/cm^3) (e.g., McSkimin et al., 1965; Mavko et al., 1998) could have slightly increased the bulk density, and the mineral density estimated from our data should be considered as an upper bound on opal-A density.

Primary microbial porosity in sinter produced by gas released by photosynthesis produces bubble-like individual pores in sinter (e.g., Lynne, 2012). Effective medium models for the measured seismic velocity of opal are consistent with moderate aspect ratio (0.2 and 0.8) penny-shaped cracks (Figure 4.8c). Thin sections and 3-D analysis of individual pores (Figures 4.2, 4.3, 4.4) also show sub-spherical to sub-ellipsoidal shapes.

In Table 4.2, we compare our results with laboratory measurements on other types of rocks. Quartz sandstone is a sedimentary clastic rock. Primary porosity in sandstone corresponds to the space between grains. For consolidated sandstone, porosity and permeability (Mavko et al., 1998; Bear, 1972, 2012) are lower than sinter. Seismic velocities of sandstone have a wide range (Mavko et al., 1998), and they can be higher than sinter at low porosity. Travertine is an analogue to sinter, but it is formed by precipitation of carbonate from water in low temperature geothermal settings. Images from μX-Ray tomography in travertine (Soete et al., 2015), show a cuboid and rod-like pore shape, while our sinter samples show more spherical to ellipsoidal pores. Furthermore, porosity in travertine is smaller (Table 4.2), permeability spans a wider range, and seismic velocities are higher than in sinter (Soete et al., 2015; Török and Vásárhelyi, 2010). Opaline chalk is a sedimentary rock composed of biogenetic clasts, siliceous shells of microorganisms that were deposited in the deep ocean. Primary porosity in chalk is given by the space inside of the shells (e.g., Compton, 1991; Chaika and Dvorkin, 1997), thus the total porosity is high, similar to sinter, but the permeability is lower (e.g., Mallon et al., 2005; Fabricius, 2007). Pumice is a vesicular volcanic rock made of volcanic glass containing bubbles. Bubbles in volcanic rocks are formed by the exsolution and expansion of gases. Values of porosity reported in effusive (e.g., Saar and Manga, 1999) and explosive volcanic rocks (Wright et al., 2009; Nguyen et al., 2014) span a wider range than in sinter. Nevertheless the permeability of vesicular volcanic rocks from 10^{-10} to 10^{-15} m^2 (e.g., Saar and Manga, 1999; Wright et al., 2009) has a similar range to that of sinter. Seismic velocities of pyroclastic rocks (Vanorio et al., 2002) range within the sinter values.

The permeability (k) of sinter shows a directional dependence with higher values in the direction parallel to the layering than in the orthogonal direction (TAT-006I and TAT-006M), similar to other layered sedimentary rocks. Values of k can vary by up to 2 orders of magnitude in the same layer (TAT-006M), reflecting the heterogeneity in individual layers. Field observations suggest higher values of permeability. For example, geysers interact with each other through the subsurface (Rojstaczer et al., 2003), presumably through permeable pathways, requiring an average permeability of the host rock of the order of 10^{-10} m^2 (Munoz-Saez et al., 2015ab). The permeability measured on centimeter-size cores represents a lower bound on field values, which are likely controlled by fractures, conduits and other high-permeability structures that increase permeability at the field scale.

Seismic velocities V_P and V_S varied linearly with porosity (ϕ). Linear regressions of V_P and V_S versus porosity (ϕ) (Figure 4.7c) show predictions of seismic velocities at zero porosity that are higher than opal, but less than quartz. Likewise, extrapolating the linear fit of ρV_S^2 to zero porosity we obtained values of G slightly higher than that for opal (Figure 4.8a). These results might be due to the high scatter in the seismic velocities. However, accessory minerals can slightly increase density and elastic modulii. From XRD we identify accessory minerals quartz, cristobalite, and zircon. Previous studies in the area also reported trydimite (polymorph of quartz) and halite (García-Valles et al., 2008; Nicolau et al., 2014). In thin sections we find other accessory minerals, including hornblende.

The formation factor shows large scatter (Figure 4.9), which can be attributed to heterogeneities in the rock structure. Nevertheless, the cementation exponent m is close to 2, as expected for Archie's Law. The tortuosity factor a depend on the pore structure, grain size, rock texture and compaction of a rock. The value $a = 0.75$ estimated for sinter falls within the expected range of 0.5 to 1.5 (Bassiouni, 1994).

4.8 Conclusions

To study the petro-physical properties of fine-layered sinters we used multiple approaches (optical microscopy, X-ray diffraction, X-ray computed tomography, and measurements of porosity, permeability, seismic velocity, and electrical resistivity). The physical properties are scattered and empirical relationships have moderate correlation coefficients, as a consequence of heterogeneities between different layers and within single layers.

Sinters are porous rocks, with more than 90% of their porosity connected. In palisade fabric, the presence of microbial filaments is found to determine pore shape and size distribution. Porosity is higher in fresh samples, decreasing over time as silica precipitates in the pore space, yet preserving the structure seen in the younger, microbial-influenced samples.

Petro-physical properties of sinter depend on lithology and texture. Opal-A is the main phase along with some accessory minerals including quartz, cristobalite, plagioclase, zircon and hornblende. Those accessory minerals, derived from the volcanic country rock, can slightly modify physical properties. Individual pores resemble spherical to elongated bubbles, consistent with effective medium models for the measured seismic velocity of opal containing moderate aspect ratio penny-shaped cracks. Porosity and permeability in sinter are different than clastic sedimentary rocks, and more similar to vesicular volcanic rocks (e.g., pumice). However, permeability shows a directional dependence with higher values in the direction parallel to the layering than in the orthogonal direction, similar to other layered sedimentary rocks.

For large-scale interpretation of geophysical surveys, and modeling of hydrogeological processes within geysers, our measurements can be considered a lower bound for permeability and resistivity and an upper bound for seismic velocity given that they do not include the effect of fractures and large-scale faulting.

4.9 Acknowledgments

This research was supported by: National Science Foundation (EAR1114184), CEGA-University of Chile, Conicyt-Chile, Center for Latin American Studies-University of California Berkeley, and the Judy Webb Chair. We thank people who provided essential help in the laboratory and in the field: Tim Teague, Dula Parkinson, Yuxin Wu, Seiji Nakagawa, Jonathan Ajo-Franklin, Atsuko Namiki, Shaul Hurwitz, Max Rudolph, Angello Negri, Pablo Ortega. We thank the editor and reviewers of JVGR for their valuable comments. The fieldwork was performed with the permission of the Amayras Communities of Caspana and Toconce.

4.10 Appendix

The effective medium model described by Kuster and Toskoz (1974) and Berryman (1980) calculates the effect of the shape of inclusions in a solid on seismic velocities. The general expressions for K_{KT} (bulk modulus) and μ_{KT} (shear modulus) (Kuster and Toskoz, 1974) are:

$$(K_{KT} - K_m)\frac{(K_m + \frac{4\mu_m}{3})}{(K_{KT} + \frac{4\mu_m}{3})} = \sum_{i=1}^{N} x_i (K_i - K_m) P^{mi} \qquad (1)$$

$$(\mu_{KT} - \mu_m)\frac{(\mu_m + \xi_m)}{(\mu_{KT} + \xi_m)} = \sum_{i=1}^{N} x_i (\mu_i - \mu_m) Q^{mi} \qquad (2)$$

where, $\xi_m = \frac{\mu_m (9K_m+8\mu_m)}{6(K_m+2\mu_m)}$

The subscripts represent the moduli of inclusion (i) and matrix (m); x_i is the volume of the inclusion (porosity in our case), P^{mi} and Q^{mi} quantify the effect of the inclusions compared to the matrix; there are different expressions for different inclusion shapes.

From Berryman (1980), for penny-shaped cracks, the values of P^{mi} and Q^{mi} are defined as:

$$P^{mi} = \frac{(K_m+\frac{4\mu_i}{3})}{(K_i+\frac{4\mu_i}{3}+\pi\alpha\beta_m)} \quad (3)$$

$$Q^{mi} = \frac{1}{5}\left(1+\frac{8\mu_m}{4\mu_i+\pi\alpha(\mu_m+2\beta_m}+2\frac{K_i+\frac{2(\mu_i+\mu_m)}{3}}{K_i+\frac{4}{3}\mu_i+\pi\alpha\beta_m}\right) \quad (4)$$

where, $\beta_m = \mu_m(\frac{3K_m+\mu_m}{3K_m+4\mu_m})$, and α is the aspect ratio (semi-minor axis/semi-major axis) of the inclusion.

The effect on seismic velocities (V_P, V_S), are calculated by inserting the effective moduli into the equations:

$$V_P = \sqrt{\frac{K_{KT}+\frac{4}{3}\mu_{KT}}{\rho}} \quad (5)$$

$$V_S = \sqrt{\frac{\mu_{KT}}{\rho}} \quad (6)$$

To simplify the equations, we considered a single material forming the rock (either opal-A/CT (e.g., Chaika, 1998; Herdianita, et al., 2000; Rodgers and Cressey, 2001; Lynne et al., 2008): μ_{mOpal} = 12.6 x10^9 Pa, K_{mOpal} = 14.2 x10^9 Pa, ρ_{mOpal}= 2 g/cm^3 or quartz (e.g., McSkimin et al., 1965; Mavko et al., 1998): μ_{mQz} = 44.3 x10^9 Pa, K_{mQz} = 37.9 x10^9 Pa, ρ_{mQz}= 2650 g/cm^3). We used standard values of liquid water for the inclusions (K_i = 2.2x10^9 Pa, μ_i = 0, and ρ_i = 1 g/cm^3). α is a free parameter that represents the effective shape of pores in the rock. Although the rock obviously contains many different pore shapes, the effective medium approximation provides a parameterization of the macroscopic behavior of the rock as a whole.

4.11 Tables and Figures

Table 4.1: Summary of the laboratory measurements

Bulk density (ρ), porosity (ϕ_{Tot} and ϕ_{Conn}), permeability (k), P-wave velocity (V_{PDry} and V_{PSat}), S-wave velocity (V_{S1} and V_{S2}), and formation resistivity factor (F_{R1} and F_{R2}). We added the core orientation, parallel (//) or orthogonal ($\perp$), and type of petrographic analysis: thin section (TS), X-ray diffraction, and μX-ray tomography (μXRT).

ID	ρ g/cc	ϕ_{Tot} %	ϕ_{Conn} %	K m^2	V_{PDry} km/s	V_{PSat} km/s	V_{S1} km/s	V_{S2} km/s	F_{R1} Ωm	F_{R2} Ωm	Or	TS/ XRD/ μXRT
TAT-002	1.00	55.79	52.92	2.33E-13	2.57	2.73	1.87	1.39	1.02	1.26	//	TS μXRT
TAT-005D	1.48	32.90	30.49	1.12E-13	3.34	3.76	3.14	2.11	-	-	⊥	TS
TAT-005G	1.37	37.62	35.69	1.85E-15	3.35	3.54	2.45	2.51	-	-	⊥	TS
TAT-005H	1.15	47.95	46.50	7.46E-15	3.14	3.31	3.11	1.92	2.60	2.98	⊥	TS
TAT-005I	1.19	45.51	43.71	-	-	-	-	-		-	⊥	TS
TAT-006A	1.63	25.78	25.17	6.89E-15	3.69	4.09	2.25	2.27	7.71	10.34	⊥	XRD
TAT-006B	1.41	35.32	34.36	1.97E-13	3.63	3.80	1.99	2.04	4.47	2.79	//	-
TAT-006FA	1.36	37.38	36.62	1.09E-12	3.62	3.74	2.17	1.92	9.81	3.47	⊥	-
TAT-006H	1.31	40.39	39.97	9.22E-14	2.63	3.77	1.51	1.19	16.61	4.48	⊥	TS
TAT-006IA	1.51	31.87	30.61	1.11E-14	3.06	3.84	2.09	2.00	5.611	10.98	⊥	XRD
TAT-006IB	1.53	31.13	29.79	4.26E-13	3.66	3.89	2.11	2.66	-	-	//	-
TAT-006LA	1.28	41.62	41.09	2.00E-14	3.35	3.38	2.42	2.35	6.48	3.58	⊥	-
TAT-006LB	1.18	46.25	46.28	3.14E-14	3.15	3.51	1.75	1.86	8.55	5.91	⊥	-
TAT-006LC	1.00	54.14	54.83	9.53E-12	3.48	3.48	2.02	1.94	15.70	5.01	//	-
TAT-006MA	1.26	43.62	42.72	6.99E-13	3.65	3.84	2.35	2.28	-	-	⊥	XRD
TAT-006MB	1.31	41.34	39.56	6.30E-15	3.78	4.17	2.42	2.28	-	-	⊥	-
TAT-006Q	1.47	33.28	31.81	1.65E-13	4.13	4.14	2.57	2.48	17.79	7.38	//	TS
TAT-006RB	1.44	34.58	32.89	4.13E-14	4.00	4.09	3.58	2.14	1.02	8.08	//	XRD
Mean	**1.33**	**39.80**	**38.61**	**7.45E-13**	**3.43**	**3.71**	**2.34**	**2.08**				
Std	**0.18**	**8.06**	**8.33**	**2.28E-12**	**0.42**	**0.36**	**0.53**	**0.38**				

Table 4.2: Petrophysical properties of different rock measured in the laboratory Sinter (this study), consolidate quartz sandstone (Mavko et al., 1998; Bear, 1972, 2012), opaline chalk (Mavko et al., 1998; Chaika and Dvorkin, 1997; Chaika, 1998; Isaacs, 1981; Mallon et al., 2005; Fabricius, 2007), travertine (Mavko et al., 1998; Soete et al., 2015; Török and Vásárhelyi, 2010), pumice (Saar and Manga, 1999; Wright et al., 2009; Nguyen et al., 2015; Vonorio et al., 2002). * Range of permeability includes carbonate chalks.

Rock type	**Main mineral**	$\rho_{mineral}$ **(g/cm^3)**	ϕ **(%)**	ϕ_c **(%)**	K **(m^2)**	V_P **(km/s)**	V_S **(km/s)**
Sinter	Opal-A	2.18	25 - 60	71	10^{-12} - 10^{-15}	2.5 – 4.2	1.0 – 3.2
Consolidate Sandstone	Quartz	2.65	1 - 40	40	10^{-13} - 10^{-20}	3.0 -6.0	1.5- 4.0
Opaline Chalk	Opal-A/CT	2.06	10 - 65	65	10^{-15}- 10^{-22*}	1.2 -4.0	0.8 – 2.2
Tavertine	Calcium carbonate	2.71	5 - 35	-	10^{-11} - 10^{-18}	3.6 -6.0	2.0 – 3.2
Pumice	Silicate glass	2.4	20 - 80	80	10^{-10} - 10^{-15}	2.0– 3.0	1.0 – 2.0

Figure 4.1: El Tatio Geyser Field and samples location
(a) Location on Google Earth (imagery date: 5/17/11); the blue line indicates the normal fault that bounds the El Tatio half-graben and the dots indicate the sampled sites: (b) TAT-002 sinter terrace (22°19'52.09"S/ 68°0'39.47"W), (c) TAT-005 extinct cone/mound without signs of geothermal activity (22°19'30"S/ 68°0'36.36"W), and (d) TAT-006 extinct cone/mound expelling vapor (22°19'44.9"S/ 68°0'32.81"W). The length of the hammer in the images is 0.9m.

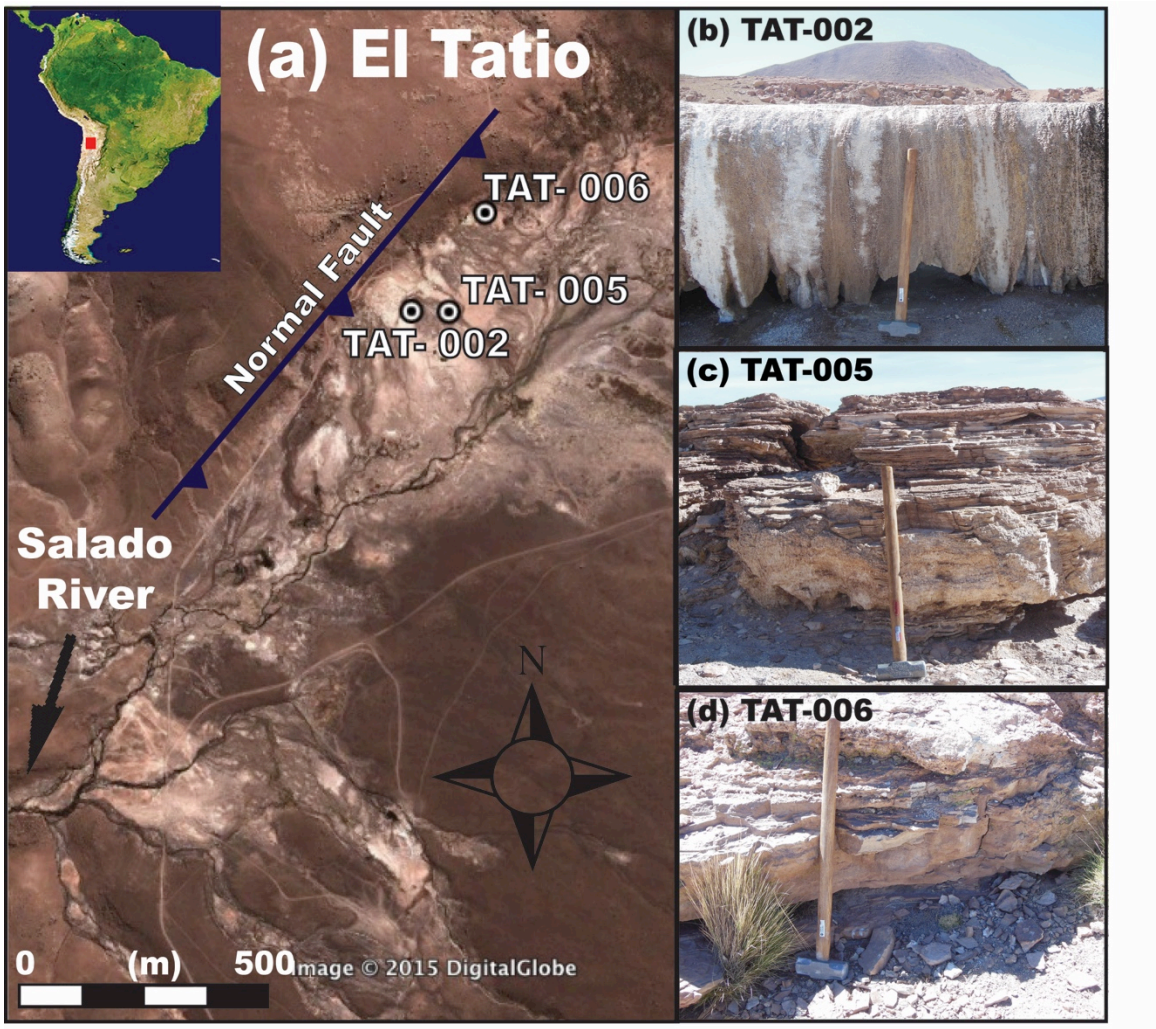

Figure 4.2: Thin sections imaged with transmitted light showing different sinter layers.
(a), (b), and (c) show variation within the same palisade texture from sample TAT-002. (d) TAT-005D, (e) TAT-005G, and (f) TAT-005I, represent different levels of the cone at site TAT-005. (g) and (h) are thin sections of sample TAT-006H, and (i) is a thin sections of TAT-006Q. The scale bar at the top of the images is the same for all images (2.5 mm).

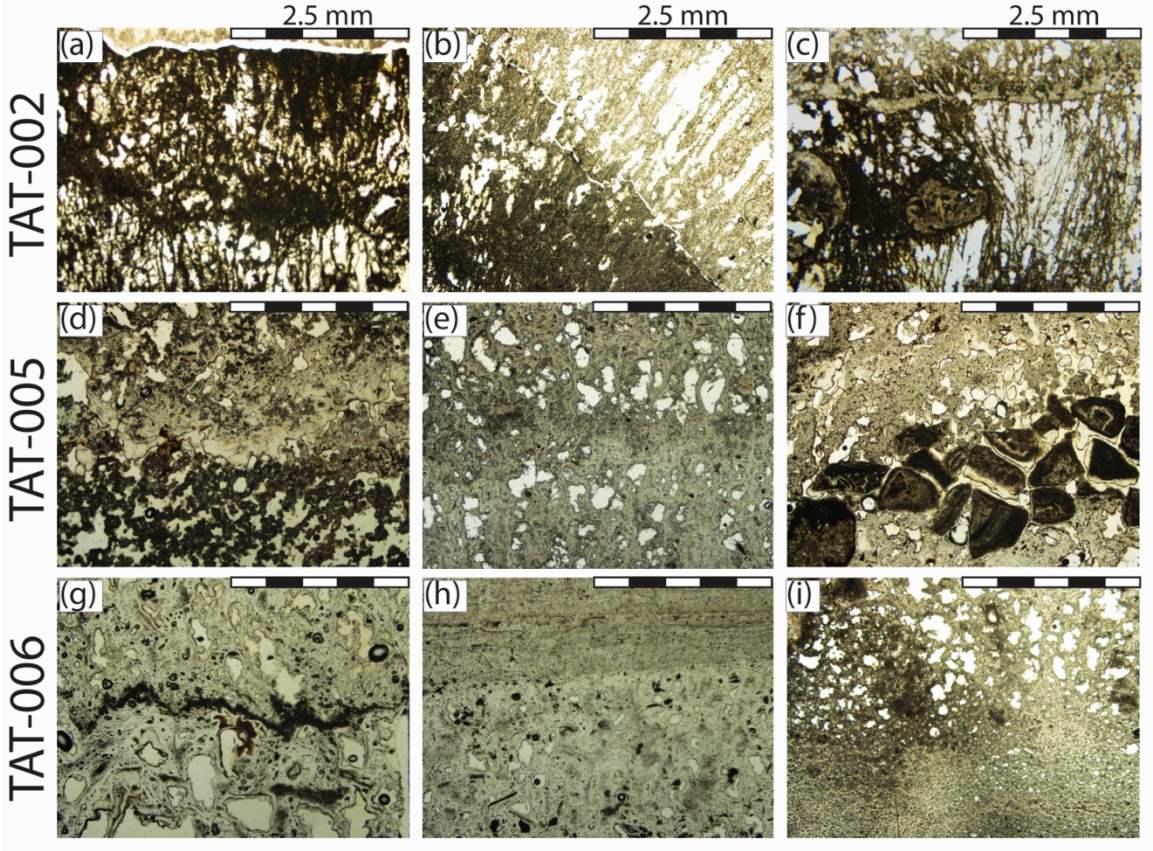

Figure 4.3: Sample TAT-002, thin sections and µXRay Tomography reconstructions (XRT)

(a) Thin section showing palisade texture with elongated pores perpendicular to the layering (Fig. 2c). (b) Magnification of (a) showing elongated microbial filaments between pores, magnified further in (c). (d) One slice through the µXRT image of the rock; black background shows empty space (pores), light blue identifies solid matrix and pink shows the microbe filaments. (e) 3D reconstruction of the core including filaments. (f) 3D reconstruction of filaments, separated from the solid matrix (light blue in d). The image exaggerates the diameter of the filaments by a factor of 4.

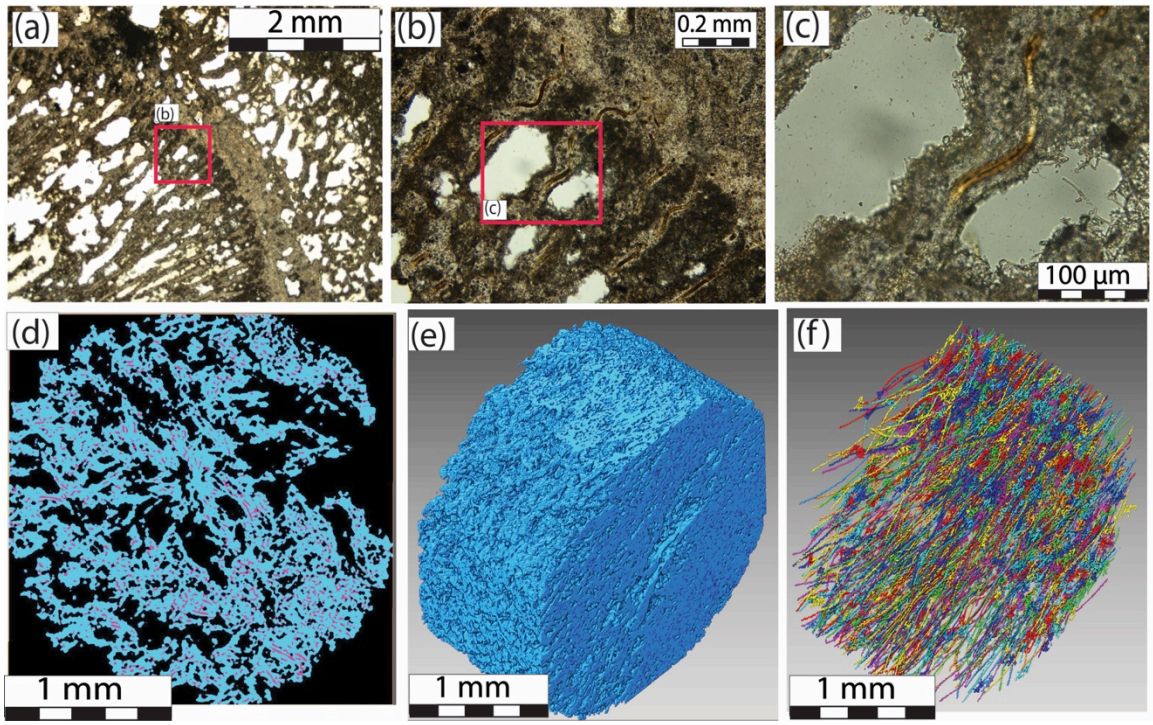

Figure 4.4: Pore structure and XRD in older cones

(a) Sample TAT-005I shows a silica oncoid and porous silica around it forming palisade-like texture. (b) Sample TAT-006Q has wavy laminated structures with pore space between laminae. (c) TAT-006H shows details of silica filling pores from the border to the center of the pores. (d) TAT-006H shows the accessory mineral hornblende filling the pores. (e) XRD diffraction of three different samples from cone TAT006 (TAT-006A was the bottom of the cone, TAT-006I was ~0.5 m height, and TAT-006M was ~1 m height from the bottom of the cone). XRD traces show opal-A broadbands, and accessory crystals of cristobalite (Cb), quartz (Qz), zircon (Zn), and plagioclase (Plg).

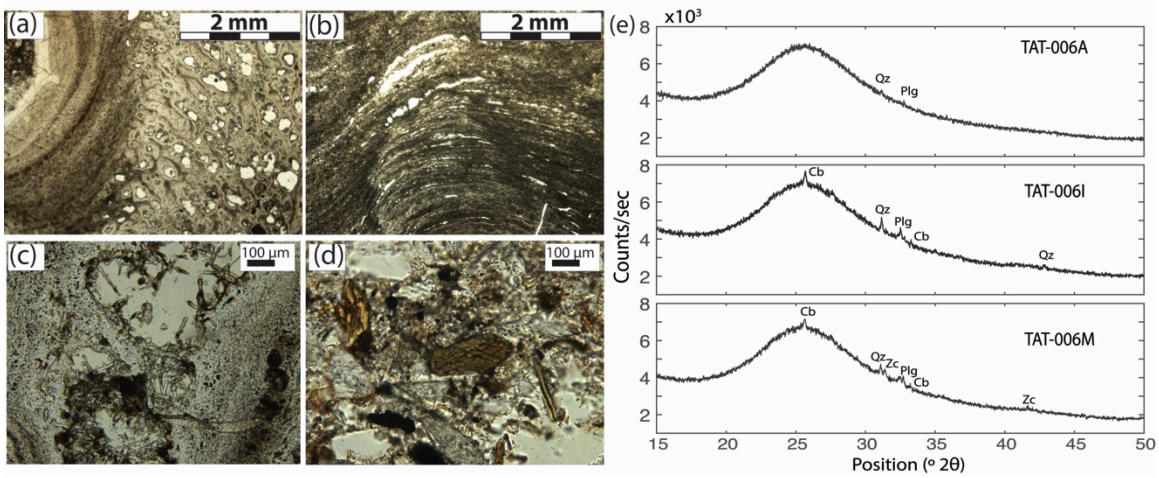

Figure 4.5: 3D XRT reconstruction and pore size distribution of sample TAT-002
(a) 3D reconstruction of the rock and, (b) individual pores in the central part of the core; blue circle on top of black square corresponds to one slice of the XRT as a reference. (c) 3D view of individual pores. (d) Plot of cumulative frequency as a function of pore volume (e) Plot of cumulative volume as a function of pore volume.

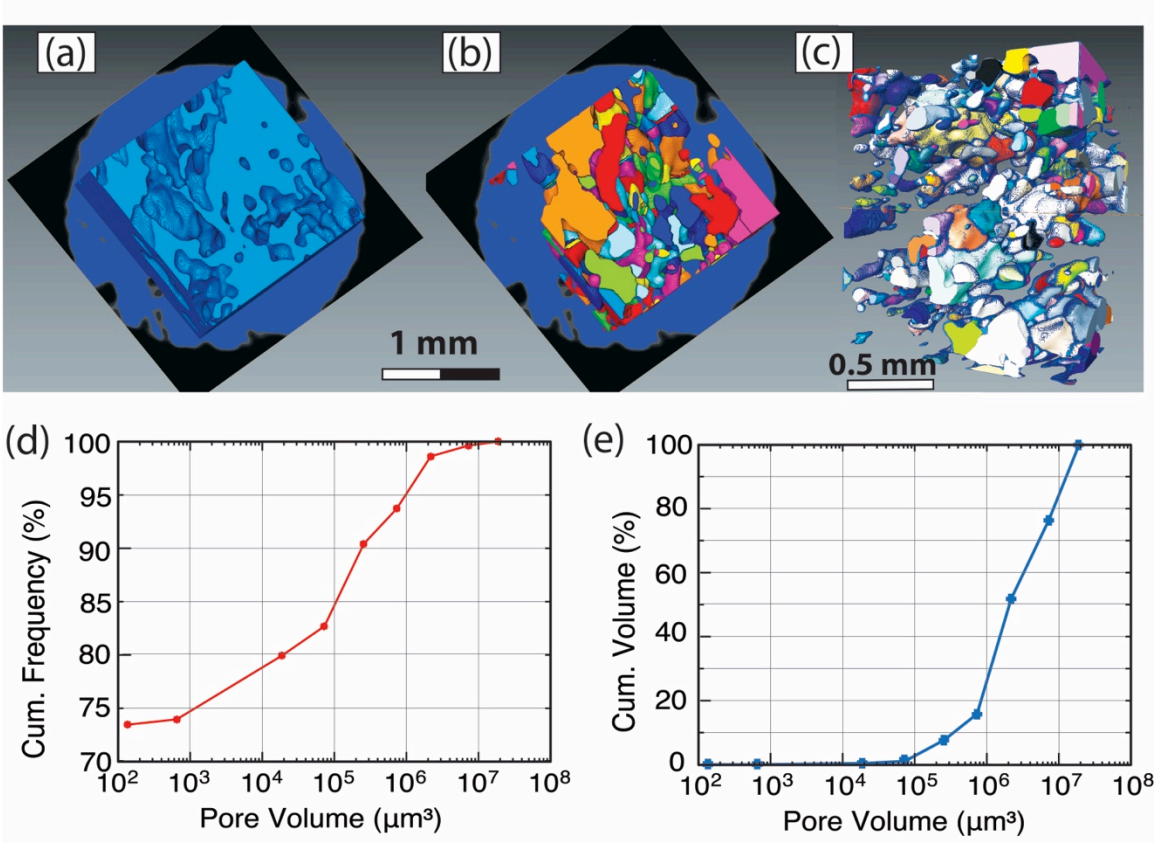

Figure 4.6: Density, porosity and permeability

(a) Linear relationship between total porosity (ϕ_{Tot}) and connected porosity (ϕ_{Conn}). (b) Porosity (ϕ_{Conn} and ϕ_{Tot}) and permeability (k) show a weak relationship. Error bars are smaller than the plotted symbols.

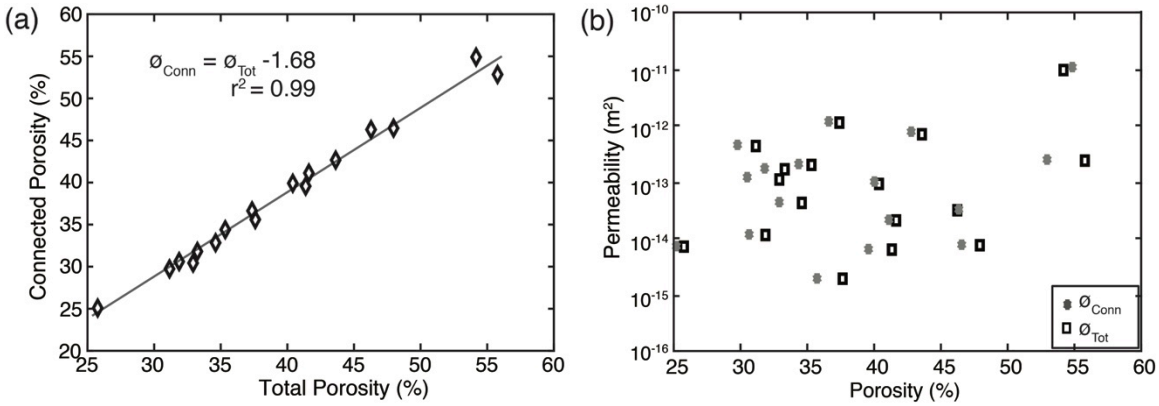

Figure 4.7: Seismic velocities

(a) Anisotropy of S-wave propagation: x-axis shows the name of every sample, and the y-axis is the ratio between the two polarized velocities. The triangles correspond to samples that were measured parallel to the layering and circles are samples perpendicular to the layering. V_{S1}/V_{S2} close to 1 indicate that waves are propagating in isotopic layers. (b) P-velocities (V_{PSat} and V_{PDry}) show a moderate negative relationship with porosity (ϕ_{Tot}). (c) S-velocities (V_{S1} and V_{S2} combined) show a weak negative relationship with porosity (ϕ_{Tot}). Seismic velocities of opal and quartz are shown as a reference for linear regressions at zero porosity. (d) P-wave velocity (V_{PDry}) and S-wave velocity (V_{S1} and V_{S2} combined) show a moderate positive linear relationship. (e) Velocity of P-wave (V_{PSat}) and density (ρ), show a moderate positive linear relationship. Error bars are smaller than the plotted symbols.

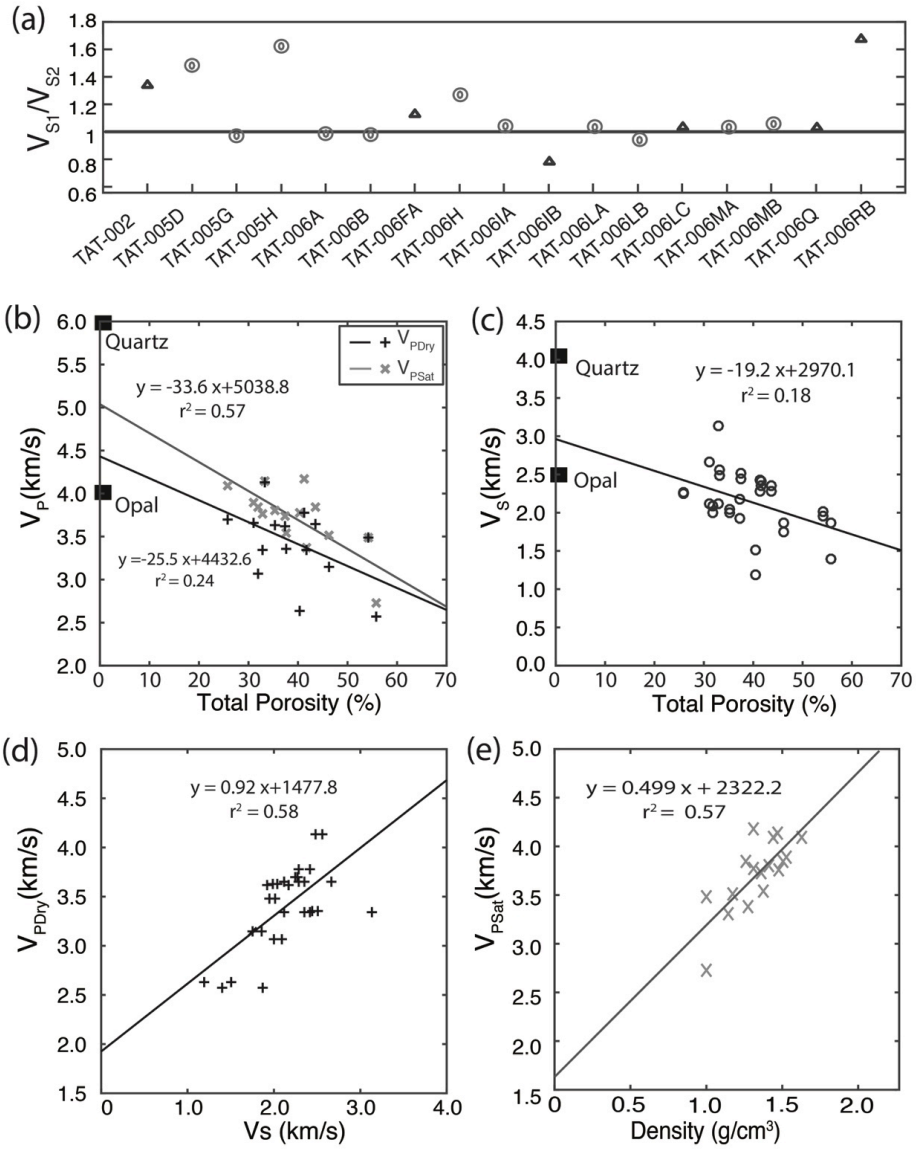

Figure 4.8: Critical porosity and effective medium models (Kuster-Toksoz, 1974), Berryman, 1980)

(a) Density-velocity (ρV^2) relationship with porosity (ϕ_{Tot}) shows a high positive linear relationship at V_{PSat}, and moderate positive relationship with V_{PDy} and V_S (V_{S1} and V_{S2} combined). The critical porosity of sinter (ϕ_c) occurs when $\rho V_S^2 = 0$, and the shear modulus (G) of the mineral occurs in zero porosity. (b) Kuster-Toksoz effective model for Opal-A/CT for pores of penny-shaped cracks with different aspect ratios 0.2 to 0.8 (same legend as a). (c) Kuster-Toksoz effective model for quartz is consistent only with penny-shaped cracks with aspect ratio of 0.1.

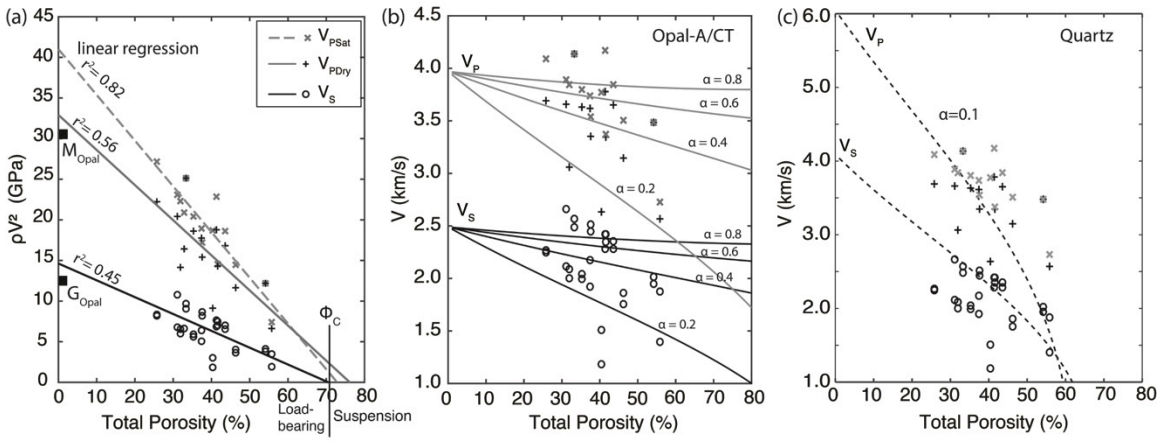

Figure 4.9: Formation resistivity factor (F_R) with total porosity (ϕ)
F_R shows a moderate power law relationship. For F_{R1} the rocks were saturated with a brine of resistivity R_{w1}=41.35 Ωm. For F_{R2} the resistivity of the brine was R_{w2}=15.81 Ωm. Using all the data *m* is 2.16 and a is 0.75.

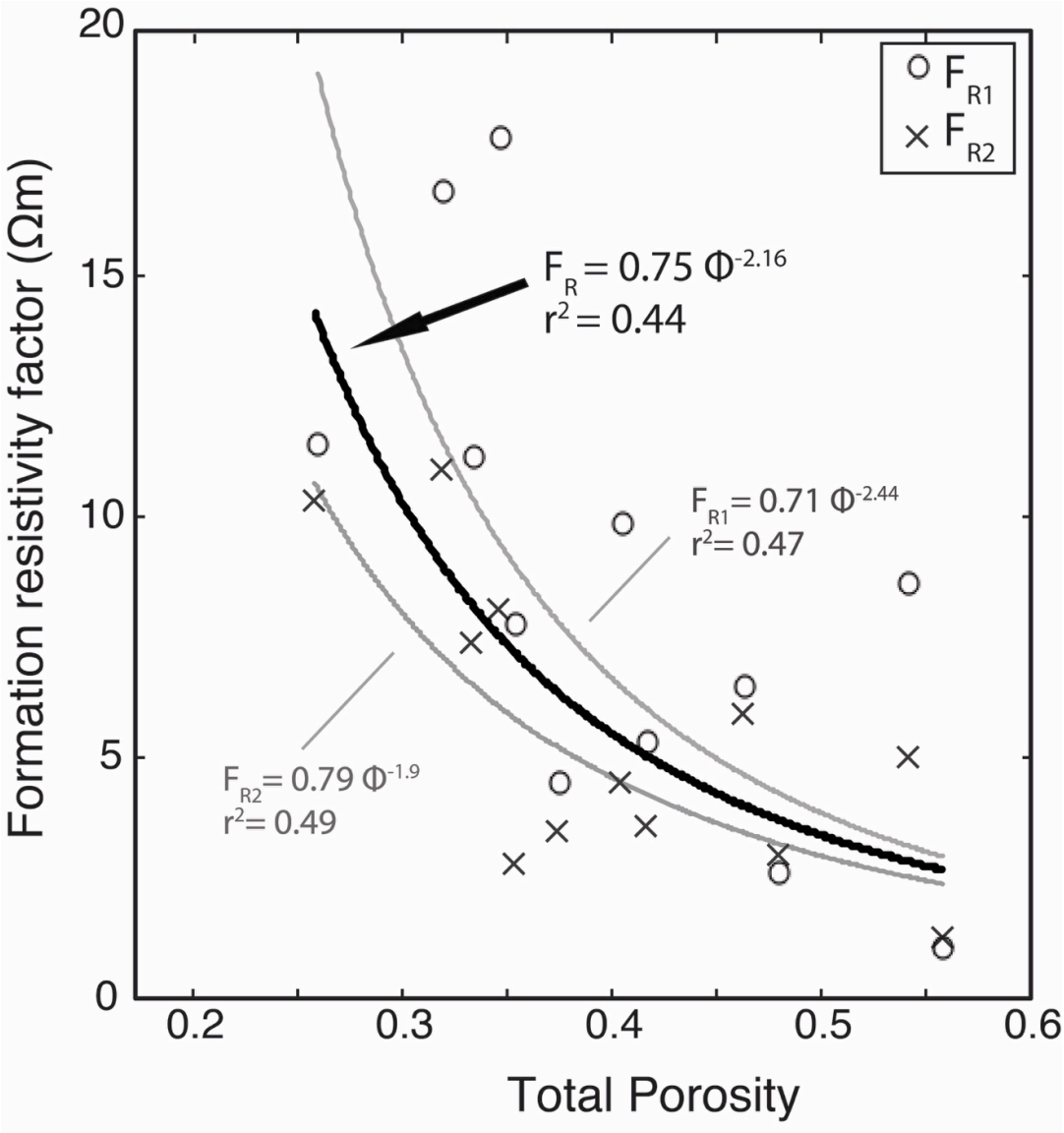

Chapter 5 Hydrogeology and geochemistry of the El Tatio geothermal basin, Atacama, Chile

5.1 Abstract

We collected water samples for isotopic and geochemical analysis and measured temperature and discharge from hydrothermal features and streams in the El Tatio geothermal basin in the Northern Chilean Andes. We found two sources of meteoric water, thermal water ascending from depth and precipitation of water from higher elevation. Andean high elevation precipitation can mix with magmatic water to generate the thermal fluids in the main aquifer, while a secondary aquifer appears to be diluted by local meteoric water. Thermal features are located on the hanging wall of a normal fault. These features present different degrees of mixing. The normal fault would allow the circulation and mixing of fluids. As the thermal fluids ascend to the surface they are affected by steam separation and dilution with local meteoric water. Dilution at shallow depth occurs in thermal springs located in marshy areas where the water table is close to the surface. At the surface, evaporation plays an important role controlling the chemistry of the fluids in thermal pools, perpetual spouters and fountain geysers. Water in discharge channels can lose as much as 30% of their water by evaporation. A field experiment performed at El Jefe geyser allows us to quantify the enthalpy of the erupting water. The specific enthalpy is lower than that in the reservoir implying that heat is lost during ascent or that ascending water mixes with cooler water. For the whole basin, the discharged thermal fluids from deep aquifers are 0.5 m^3/s.

5.2 Introduction

The characteristics of thermal waters discharged at Earth's surface provide insights into subsurface geothermal processes. For example, discharge and temperature help assess the mass and energy budget of geothermal systems; dissolved ions can be used to infer reservoir temperatures; stable isotopes of oxygen and hydrogen reveal mixing, phase separation and water sources; radiogenic isotopes constrain water sources and ages.

The El Tatio basin is the largest geothermal field in South America (Tassi, et al., 2005), and owing to its location in the arid Atacama Desert, Chile, the origin and dynamics of water discharged at the surface have been of considerable interest (e.g, Ellis, 1969; Healy and Hochstein, 1973; Cusicanqui et al., 1976; Giggenbach, 1978; Cortecci et

al., 2005; Tassi, et al., 2005; Munoz-Saez et al., 2015ab). Thermal manifestations appear mostly in three main areas: the upper, middle and lower basins (Figure 5.1). The upper basin, contains the largest number of thermal features, including dozens of geysers, and these are aligned in the northeast direction along the hanging wall of a normal fault (Figure 5.1). The middle basin is located in the southern part of the field; deep pools with fountain–type eruptions dominate, and mud pools are found to the southwest. The lower basin is located to the west, along the banks of the Río Salado, and includes geysers and thermal springs.

Here we report a new data set of stable isotopes of oxygen and hydrogen, and measurements of temperature, pH, and conductivity across the different thermal features. We also report measurements of chemistry, discharge and tritium of water in the channels that collect discharge from the different basins and drain to the Salado River. We performed an active experiment in one geyser to estimate the enthalpy of the erupting water and the amount of steam released to the atmosphere. The goals of this study are to understand: (1) source of fluids, (2) processes affecting these fluids from the source reservoirs to the outflow, and (3) better assess the mass balance and energy balance of the basin.

5.3 Geological setting and Previous Studies

El Tatio is an active geothermal area located in the Atacama Desert, north of Chile (elevation > 4,000 m). El Tatio is the third largest active geyser field in the world, and the largest one in the southern hemisphere (Glennon and Pfaff, 2003). It is located in the semi-arid Chilean Altiplano at 4200 m a.s.l., with environmental conditions characterized by large diurnal temperature oscillations (-10 to 10^{o} C). Most water drainage is associated with summer rains (South American Monsoon) from the Bolivian highlands.

El Tatio more than 200 thermal features (e.g., Zeil, 1959; Trujillo et al., 1969) within an area of ~30 km^2 (Tassi et al., 2005), including ~80 eruptive features with temperature near the local boiling temperature of 86°C (Glennon and Pfaff, 2003). Three basins, the upper, middle and lower basins (Figure 5.1) contain most of the features, and few thermal springs occur north of the Salado River (along the Tucle River), and fumarole activity emerges southwest of the middle basin.

The heat for the system is provided by Holocene andesitic stratovolcanoes with no historical eruptions (Lahsen, 1976ab). Based on chemical and isotopic characteristics of water from wells and surface discharge, the thermal waters originate from mixing between magmatic fluids, meteoric water and hydrothermal sources (Cusicanqui et al., 1976; Giggenbach, 1978; Cortecci et al., 2005; Tassi et al., 2010). Most thermal manifestations are located within an area of ~10 km^2, and the distribution of the thermal features is bounded by a North-South trending half-graben (Figure 5.1). The basin is

filled with ~1000 m of sub-horizontal ignimbrites, tuffs and lavas which are covered by Holocene alluvial, glacial and sinter deposits (Healy, 1974; Lahsen and Trujillo, 1975). Diverse geothermal features have been reported, including geysers, hot springs, perpetual spouters, mud pools, mud volcanoes, fumaroles, and extensive sinter terraces and aprons (Glennon and Pfaff, 2003).

Previous studies at El Tatio were focused on understanding the origin of the fluids and estimating the magnitude of the geothermal resources. These include several geological, geochemical and geophysical studies, and exploration/exploitation drilling campaigns conducted in the upper and middle basins (e.g., Trujillo, 1969; Ellis, 1969; Ambrust et al., 1974; Cusicanqui et al., 1975; Lahsen, 1976; Giggenbach, 1978, 1982; Marinovic and Lahsen, 1984; Cortecci et al., 2005; Tassi et al., 2005). Hydrogeological models indicate that the recharge of meteoric waters occurs 15 km east of the field, infiltrates through normal faults, and heats as it travels to the west at a mean rate of about 1.3 km/year based on tritium isotopes (Healy and Hochstein, 1973; Cusicanqui et al., 1975; Giggenbach, 1978; Muñoz and Hamza, 1993). The fluid is confined in two major aquifers in fractured and permeable volcanic units, with temperatures of 190^{o}C and 250^{o}C (Healy and Hochstein, 1973; Cusicanqui et al., 1975). The colder aquifer appears to be the result of underground dilution of hotter aquifer water with local meteoric water (Giggenbach and Stewart, 1982). Water from springs and wells show high chloride and bicarbonate waters in the north (upper basin), and intermediate to low chloride and sulfate-bicarbonate waters in the south (middle basin) (e.g., Ellis, 1969; Cusicanqui et al., 1975; Giggenbach, 1978; Cortecci et al., 2005; Tassi et al., 2005).

Oxygen and hydrogen isotope studies performed over the past 30 years document ^{18}O enrichment and ^{2}H depletion that support the inferences about water mixing and sources (Giggenbach, 1978; Giggenbach and Stewart, 1982; Cortecci et al., 2005, Tassi et al., 2010). The chemistry and isotopic trends reveal a variety of processes, though some uncertainty and debate remain. The properties of water in the hot aquifer result from rock-water interaction as water travelled from its source 15 km east of El Tatio (Giggenbach, 1978); this interaction would increase $\delta^{18}O$. Alternatively, the isotopic composition of the hot aquifer and some of the chloride thermal features can be explained by mixing of high altitude precipitation and andesitic water (Cortecci et al., 2005; Tassi et al., 2005). Steam separated from both aquifers, in a single-step process or in continuous-steps, as the fluid ascended from the aquifer, would increase δD (Giggenbach, 1978; Giggenbach and Stewart, 1982; Cortecci et al., 2005). The water left after steam separation would be diluted with local groundwater (Giggenbach and Stewart, 1982). High sulfate waters may be the result of steady-state evaporation and absorption of sulfide from magmatic steam (Giggenbach, 1978; Giggenbach and Stewart, 1982; Cortecci et al., 2005). Carbon and strontium in the water (Cortecci et al., 2005), and helium isotopes in the gas (Tassi et al., 2005), also imply significant magmatic input in the chloride thermal waters.

5.4 Methods

5.4.1 Field measurements and sampling

Thermal features appear in clusters; based on these locations, we group samples in six different areas (Figure 5.1):

(1) The upper basin (UP) contains most of the eruptive features -- geysers and perpetual spouters (Glennon and Pfaff, 2003). Thermal features developed on and created a sinter plain aligned with a normal fault. We measured and sampled 20 eruptive features, and 13 non-eruptive hot springs.

(2) Vega Rinconada (VR) is located in the northern part of the upper basin. Thermal features emerge from a marsh. The area contains one active geyser, and numerous hot springs and mud pools. We sampled and measured the geyser, 9 hot springs, and measured the temperature of 39 mud pools.

(3) The middle basin (MB) hosts several boiling pools that erupt as fountains and a few non-eruptive hot springs (Glennon and Pfaff, 2003). Thermal features emerge within a sinter plain. We measured and sampled 8 fountain geysers and one hot spring. We measured the discharge of water from 6 of the fountain geysers.

(4) The south east (SE) of the middle basin is characterized by mud volcanoes and non-eruptive hot springs and mud-pools. Thermal features emerge from hydrothermally altered soil/rock. We measured and collected water samples from 2 hot springs. We measured the temperature of 4 mud volcanoes and 7 mud pools.

(5) The lower basin (LB) is located at the western part of the field; thermal features are distributed along the Salado River (Glennon and Pfaff, 2003) and near the intersection with the Tucle River. We measured and collected water samples for 9 eruptive features and 9 hot springs. We include in this area an eruptive feature located near the southern edge of the normal fault.

(6) Creeks or discharge channels (Figure 5.1) collect water from the basins and wetlands. Wetlands sustain channels with flowing water in the Middle Valley area (Glennon and Pfaff, 2003); we measured and sampled water in one of these channels (GW). Thermal water from the basins drain to different creeks and form the Salado River (sample #1). We studied one discharge channel from the UB (sample #0), two from the MB (sample #112 and #113), one from the SE (sample #100), the Tucle River (sample #400) that collects water from the south, and the Rio Salado that collects water from the entire geothermal field.

We performed in situ measurements and collected water samples from October 5th to 8th, 2014. We measured temperature, pH, electrical conductivity and collected water samples for stable isotopes (δ^{18}O and δD) in eruptive features (geyser and perpetual spouters) during the resting period or during the eruption, hot pools, hot springs, and creeks. Additionally, we measured discharge whenever possible, and collected water samples for tritium (^{3}H) and chemical analysis of major elements (Figure 5.1) from water

in creeks, one hot spring and the geyser in VR. In mud pools and mud volcanoes we only measured temperature.

Digital temperature probes used in the field are accurate to 0.2°C. The pH and electrical conductivity meter has a 2% accuracy. The probe used to measure flow velocity has an accuracy of 0.03 m/s. Discharge was calculated by surveying the cross section of the channel. We measured velocity across the channel following standard gauging procedures (Corbett et al., 1943).

We collected 60 ml of unfiltered water for $\delta^{18}O$ and δD, and 500 ml of unfiltered water for ^{3}H. For major elements, we collected two 120 ml samples at each site, one for anions and the other for cations. For major elements, we stored filtered water (0.45 mm filter) for anions, and acidified the water (nitric acid) for cations. We used high-density polyethylene bottles for all samples.

5.4.2 Analytical methods

Anion concentrations of Cl^-, F^-, Br^-, and SO_4^{2-} were determined using ion chromatography. The analytical errors for Cl^-, F^-, and SO_4^{2-} are <3% and for Br^- is <5%. Total alkalinity as HCO_3^- was measured by titrating 10ml of sample with 0.05 N sulfuric acid to the bicarbonate end-point. Usually, samples were stored for one month before the measurement. The analytical error for alkalinity is ~5%. Cation concentrations, Na^+, K^+, B^+, Mg^{2+} and Ca^{2+} were measured using an inductively coupled plasma atomic emission spectrometer (ICP-AES). The analytical errors for Na^+, K^+, and B^+ were <5%, and for SiO_2^+, Mg^{2+} and Ca^{2+} are <10%. For all samples, the charge balance between anions and cations was < 13%.

Stable isotope analysis of oxygen and deuterium was carried out using the water–CO_2 equilibration method for oxygen (Epstein and Mayeda, 1953) and the zinc-reduction method for deuterium (Coleman et al., 1982). Isotopic ratios ($\delta^{18}O$, and δD) were measured in a mass spectrometer. Results were reported in delta notation per mil, using the standard reference Vienna-Standard Mean Ocean Water (V-SMOW). The analytical errors of $\delta^{18}O$ was ~0.2% and of δD was ~1%.

Tritium (^{3}H) analyses were performed by the ^{3}He in-growth method (Bayer et al., 1989). About 170 ml of unfiltered water was degassed, sealed into a vacuum flask, and stored for approximately 3 months. During this period, the sample accumulated ^{3}He. The amount of ^{3}He was measured by a magnetic mass spectrometer. The ^{3}H concentration was calculated from the storage time and the decay constant (Lucas and Unterweger, 2000). The detection limit was 0.05 TU (1 TU is equal to 1 atom of ^{3}H per 10^{18} atoms of hydrogen).

5.4.3 Active experiment at El Jefe geyser

To estimate the enthalpy associated with a geyser eruption and the steam released to the atmosphere, we performed an active experiment at El Jefe (EJ) geyser (Figure 5.1). The estimated amount of water erupted by EJ in 2012 was >110 liters/eruption (Munoz-Saez et al., 2015a). On Oct. 8th 2014, we added 125 liters of water at ~15^{o}C to the geyser conduit during one quiescent period. Before, during, and after the experiment, we filmed a video of the eruptions at the surface, and we recorded pressure and temperature in the conduit. Sensors were located 1.5 m below the surface. We recorded every 1 s with a data logger. A K-type thermocouple measured temperature with 1^{o}C accuracy, and a pressure transducer measured pressure with 2.5% accuracy.

5.5 Results

5.5.1 Field measurements

Most erupting features during their resting periods have temperatures >80^{o}C (Figure 5.2 aef, Table 5.1), which is close to the local boiling point (~86.6^{o}C). Hot springs and mud pools have temperatures that varied between 45 to 86 ^{o}C. Water in the discharge creeks have temperatures between 20^{o}C and 35^{o}C. The temperature of the wetland (GW) was 35^{o}C.

Values of pH (Figure 5.2 be, Table 5.1) in the field varied from 5.3 to 8. Most of geysers in the upper basin (UB) have pH close to neutral (6.5 to 7.5). At the southern part of the UB, hot springs and perpetual spouters are more acidic, pH down to 6.2. The geyser at Vega Rinconada (VR) has neutral pH, while the hot springs and mud pools have pH neutral to acidic (as low as pH 5.4). The pH in VR tended to decrease with decreasing the temperature (Figure 5.2 e). Thermal features in the middle basin (MB) are neutral to slightly basic (6.9 to 7.4). The hot springs in the southeast (SE) show more basic pH (7.1 to 7.8). In the lower basin (LB), the hot springs located in the north had more acidic pH (6.5 to 6.8) compared with the thermal features (hot springs and eruptive features) in the south (pH 7 to 7.5). The water in the discharge channels tends to be basic, pH 7.4 to 8. The GW has pH 7.5.

Electrical conductivity of the water measured in the field (Figure 5.2 cf, Table 5.1) varied from 0 to 19 µS/cm. The UB has the highest values, and most of thermal features are between 14 and 19 µS/cm. The thermal features located in the VR show the greatest spread of conductivity. In VR there are two distinct groups: the geyser and some hot springs have conductivity between 12 and 16 µS/cm, similar to the UB; and hot springs of conductivity between 0.2 to 6 µS/cm. Thermal features in the MB show conductivity between 12 and 15 µS/cm. The hot springs at the SE show low conductivity ~0.7 µS/cm. The thermal features in the LB have conductivity values between 11 and 14 µS/cm. The GW has a conductivity of ~1 µS/cm. The conductivity of the discharge channels varies from 7 to 15 µS/cm.

Discharge from UB (sample #0) is 250 L/s (Figure 5.2d, Table 5.1). Downstream, the discharge from MB is 15 L/s in the north discharge channel (sample #112), and 4.7 L/s in the south discharge channel (sample #113). Discharge from the SE (sample #100) was 3.8 L/s. The discharge of the GW is 0.48 L/s. Discharge in the Tucle River is 140 L/s (sample #400), and the Salado River is 860 L/s (sample #1). Discharge from the thermal features located in the MB varied between 0.1 cm^3/s and 5.8 cm^3/s.

5.5.2 Major elements

Chemistry of major elements (Figure 5.1, Table 5.2) show that concentrations of Cl^- and Na^+ are at least one order of magnitude higher than other ions. Highest concentrations of Cl^- (>7000 mg/l), F^- (>3.5 mg/l), Br^- (>7.5 mg/l), Na^+ (>4000 mg/l), Ca^{2+} (>290 mg/l), K^+ (>220 mg/l), As^{+3} (>43 mg/l), and B^+ (>140 mg/l) are associated with the channels coming from the MB (samples #112, 113) and from the geyser in VR (sample # 225).

Intermediate values of Cl^- (3350 to 5400 mg/l), F^- (1.1 to 1.7 mg/l), Br^- (3.0 to 5.5 mg/l), Na^+ (1974 to 3236 mg/l), Ca^{2+} (120 to 240 mg/l), K^+ (150 to 220 mg/l), As^+ (19 to 32 mg/l), and B^+ (84 to 140 mg/l) appear in the channels coming from the UB (sample #100), SE (sample #0) and Salado River (sample #1). Lower values are present in water coming from the Tucle River (sample #400): Cl^- 1540 mg/l, Na^+ 961 mg/l, F^- 0.5 mg/l, Br^- 1.5 mg/l, Ca^{2+} 92 mg/l, K^+ 93 mg/l, As^+ 11.6 mg/l, and B^+ 41 mg/l. Much lower concentrations of Cl^- (<350 mg/l), F^- (<0.3 mg/l), Br^- (<0.3 mg/l), Na^+ (<271 mg/l), Ca^{2+} (<20 mg/l), K^+ (<31 mg/l), As^+ (<3 mg/l), and B^+ (<9.2 mg/l) are present in the GW and the hot spring in VR (sample #231).

The highest values of SO_4^{2-} (117 mg/l), HCO_3^- (271 mg/l) and Mg^{2+} (20.6 mg/l) are found in the water from the Tucle River. Lower values of SO_4^{2-} (53 to 81 mg/l) are associated to the Salado River, the SE, and the MB. The samples with lowest concentration of SO_4^{2-} (<50 mg/l) were from the UB, the GW, the geyser and hot spring in VR. HCO_3^- varies between 145 and 180 mg/l in the Salado River, the UB, the SW, and GW, while the lowest concentration samples (HCO_3^- <60 mg/l) are from the MB, and the geyser and hot spring from VR. Values of Mg^{2+} between 5.7 and 12.4 mg/l are found in the Salado River, all of the discharge channels, and GW, while concentrations <1 mg/l are associated with the geyser and hot spring from VR.

The highest concentration of SiO_2 is in the VR geyser (319 mg/l). Water from channels and rivers had lower SiO_2 concentrations (from 190 to 250 mg/l). The lowest values of SiO_2 are associated with GW and the hot spring, 147 and 143 mg/l respectively.

5.5.3 Isotopes of oxygen and deuterium ($\delta^{18}O$ and δD)

The value of $\delta^{18}O$ varies between -9.08‰ and 1.18‰, while δD varies between -88.3‰ and -46.4‰. Figure 5.3 shows the distribution of isotopic values noting that -8.8

for $\delta^{18}O$ and -53 for δD (Giggenbach, 1978), and -8.8‰ for $\delta^{18}O$ -58‰ for δD (Cortecci et al., 2005), are taken as reference values from the literature for local meteoric water. The GW sample has an isotopic signature of $\delta^{18}O$ -9.08‰ and δD -57.9‰, the most similar to meteoric water of our samples. Creeks and rivers seem to be enriched in $\delta^{18}O$ and δD with respect to meteoric water. The thermal features at UB tend to be enriched in $\delta^{18}O$ and depleted in δD with respect to meteoric water, except for sample 209 that is extremely enriched in δD. In VR, the geyser and most thermal pools are enriched in $\delta^{18}O$ and depleted in δD, similar to the UB. Few pools have δD slightly higher than meteoric water but they are strongly depleted in $\delta^{18}O$. Values of $\delta^{18}O$ tend to increase with conductivity (Figure 5.3d, VR) but δD does not show any clear trend (Figure 5.3e, VR). Isotopic values of thermal features in the MB and LB were less variable; we observe an enrichment of $\delta^{18}O$ and depletion of δD with respect to meteoric water. In the MB, values of $\delta^{18}O$ are between -6‰ and -4‰, and values of δD are between -69‰ and -65‰. In the LB, values of $\delta^{18}O$ are between -6.5‰ and -5.2‰, and values of δD are between -72‰ and -68‰. The hot springs in the SE area are enriched in $\delta^{18}O$ and δD with respect to meteoric values.

5.5.4 Tritium

Tritium concentrations (Table 5.3, Figure 5.1 for locations) are low, though a few (samples # 100, 112, 231, 400) are above the detection limit (>0.05 TU). The highest value of ^{3}H is found in the GW sample (0.28 ± 0.03 TU). The drainage from the UB (sample # 0) has a concentration of ^{3}H of 0.14 ± 0.04 TU, the water draining from the MB (sample # 113) has a ^{3}H value of 0.18 ± 0.05 TU, and the water from the Salado River is 0.13 ± 0.05 TU.

5.5.5 Active experiment at EJ geyser

During the addition of cold water into the conduit, the temperature of the water in the conduit at 1.5 m decreased from 86°C to 69°C in less than 30 s. The pressure in the conduit increases linearly from 6.8×10^4 to 7.5×10^4 Pa, these values include atmospheric pressure (6.1×10^4 Pa). The initial height of the water column above the sensor was 0.7 m. During the experiment the conduit was filled up to the surface, which accounts for an additional 0.8 m of water above the sensor, explaining the pressure increase. Before the experiment, El Jefe geyser (Figure 5.4) had periodic eruptions every 110 s. After adding the cold water the geyser skipped two eruptions, however the periodic signal of pressure and temperature continued. The geyser restored the 110 s cycle after the two missed eruptions.

5.6 Discussion

5.6.1 Origin of the fluids

The sample from the wetland, GW (Figure 5.1), has a pH close to neutral (slightly basic), low electrical conductivity (Figure 5.2), low concentration of dissolved ions, the highest value of ^{3}H, and an isotopic signature similar to meteoric water described in previous studies (e.g., Ellis, 1969; Cusicanqui et al., 1969; Giggenbach, 1978; Cortecci et al., 2005). The isotopic signature of GW ($\delta^{18}O$ about -9‰ and δD about -58‰) coincides with the local meteoric water line LMWL (Aravena, 1995; Chaffaut et al., 1998; Figure 5.5). Streams in this wetland had been previously been described as thermal features (Zeil, 1956; Trujillo, 1968) because they present temperatures >35^{o}C. Previous studies (e.g., Cusicanqui et al., 1969; Giggenbach, 1978; Cortecci et al., 2005) found local meteoric water slightly enriched in the heavy isotopes ($\delta^{18}O$ about -8.5 and δD about -52). Thus, this light GW water might correspond to local meteoric water that infiltrates underground and warms up with steam before reaching the surface again.

Measured Cl^- has a linear relationship with electrical conductivity (coefficient of correlation of r^2 of 0.99) and electrical conductivity will be considered a proxy for Cl^- concentration in the waters for which we did not perform chemical analysis. We found high values of electrical conductivity, and Cl^- >8,000 mg/kg, associated with the UB (Figure 5.2 cf). Similar values of salinity are reported in previous studies (e.g., Ellis, 1969; Cusicanqui et al., 1969; Giggenbach, 1978; Cortecci et al., 2005; Nicolau et al., 2014), suggesting that these waters are less diluted with meteoric waters and are more closely related to the reservoir (Giggenbach, 1978). The geyser in the VR area shows similarities to the UB geysers in temperature, pH, electrical conductivity, Cl^- concentration (8000 mg/kg), and isotopic composition, suggesting that the fluids originate from the same reservoir. Intermediate values of Cl^- >5000 mg/kg are predominant in the UB, MB, and LW.

In general, chloride thermal waters are enriched $\delta^{18}O$ and depleted in δD (Figures 5.3 and 5.5). Several processes had been invoked in previous studies to explain these isotopic trends (Figure 5.5a and Figure 5.6). Two reservoirs had been inferred based on information from geothermal wells drilled in the 1960s and 1970s (e.g. Cusicanqui et al., 1969; Giggenbach, 1978; Cortecci et al., 2005): a hot aquifer (A) of 260 to 270^{o}C, $\delta^{18}O_A$ about -6.9‰, and δD_A about -78‰, feeding the UB and VR, and a colder and more diluted aquifer (B) of 170^{o} to 190^{o} C, $\delta^{18}O_B$ about -7.2‰ and δD_B about -73‰ supplying water to the MB and LB (e.g., Cusicanqui et al., 1969; Giggenbach, 1978). Geothermal wells 2 and 5, drilled around the UB (e.g., Ellis, 1969; Cusicanqui et al., 1969; Giggenbach, 1978), have isotopic values and temperatures >200^{o}C similar to aquifer A. Wells 3 and 4 (e.g., Ellis, 1969; Cusicanqui et al., 1969; Giggenbach, 1978), which are located near the MB, have isotopic compositions similar to the cold aquifer but temperatures > 200^{o}C.

The hot reservoir can be generated by mixing (Cortecci et al., 2005; Tassi et al., 2010) between andesitic water (Taran et al., 1989; Giggenbach, 1992) and meteoric water from high altitude, different than the local meteoric water (GW), with δD about -107‰, and $\delta^{18}O$ about -14.6‰ (e.g., Mahon and Cusicanqui, 1980; Fritz et al., 1979; Gonfiantini et al., 2001); alternatively, infiltration of water enriched with respect to meteoric water that interacted with the surrounded rock may explain this trend (Figure 5.5a, Giggenbach, 1978). Our isotopic data show that most of thermal waters from the UB and the geyser of VR are aligned with the mixing line with hot aquifer A, favoring the idea of a magmatic input to the reservoir. Low values of pH <6 for some pools in VR may also point to magmatic input. The tendency of pH to decrease with decreasing temperature (Figure 5.2be) can be associated to the development of acid-sulfate water, which occurs by addition of HCl and SO_2 from a magmatic source of water. This magmatic input would be consistent with magmatic mixing suggested by the isotopes. Previous studies also reported thermal pools with high sulfate concentration >240 mg/kg in the area (Ellis, 1969; Cusicanqui et al., 1969; Giggenbach, 1978), however the two measured thermal sources had low values of sulfate <50 mg/kg.

The thermal features in the MB and LB have lower amounts of chloride indicating a more diluted origin, probably related to aquifer B. Considering the dilution line between GW and A, we estimate that the cold aquifer B was diluted with ~25% local meteoric water, which is slightly higher than the value described in previous studies of 17% (Giggenbach, 1978).

5.6.2 Process affecting the fluids rising up to the surface

Steam separation can occur as the fluid rise to the surface from the reservoir, and steam separation would explain the enrichment in $\delta^{18}O$ and δD of the chloride thermal waters with respect to the aquifer (e.g., Giggenbach, 1978; Giggenbach and Stewart, 1982; Cortecci et al., 2005). The isotopic composition of some of our thermal sources coincides with multi-stage steam separation from both aquifers (Figure 5.5b). Using the chemical analysis of VR geyser (sample # 225, Table 5.1), we estimate a reservoir temperatures using various geothermometers: for silica, 195.8°C for adiabatic ascent and 214.3°C for conductive heat loss (Founier, 1977); for Na/K/Ca, 213.3°C (Fournier and Truesdell, 1973); for Na/K, 250.4°C (Fournier, 1979), 254.1°C (Giggenbach, 1988), or 240.9°C (Arnorsson, 2000). The highest estimated temperature of 254.1°C is close to the temperature of hot aquifer A ~260°C (Giggenbach, 1978) used for steam separation calculation (section 5.1).

In the UB and VR (Figure 5.5cd), the isotopic signature of the chloride water of most of the geysers and thermals pools, show a trend that can be attributed to mixing or steam separation processes, while some perpetual spouters are enriched in $\delta^{18}O$ and δD with respect to values from steam separation. The linear regression of all the thermal features in the UB generates a line with $r^2 = 0.8$, and a slope of ~3.5, which is identical to

slope of the mixing line. These thermals features are located on the hanging wall of a normal fault (Figure 5.1). This structure would allow the circulation of meteoric fluid derived from higher altitude and deeper magmatic components to generate different degrees of mixing along the mixing line. Additionally, evaporation might occur in the samples with the highest electrical conductivity and thus chloride (Figure 5.3, sample #209), which are highly enriched in the heavy isotopes. Those samples correspond to perpetual spouters that are constantly erupting and losing steam while recycling the liquid water.

Thermal waters from the MB show isotopic values that form a line; the linear regression of the isotopic values generates a line of $r^2 = 0.95$ and a slope of 1.9. The departure point of the line can be the residual liquid from steam separation from the cold aquifer (δ_{SSB}). Thermal features in the MB correspond to large pools of > 2 m diameter with permanent fountain eruptions. They are subjected to high evaporation, given the large area exposed to the air. We assess this evolution considering only the effect of kinetic fractionation during evaporation given by the simplified Rayleigh distillation equation

$$\delta_L - \delta_e = \varepsilon_k \qquad (1)$$

where δ_L is the composition of liquid, δ_e is the composition of the evaporated vapor, and ε_k is the kinetic fractionation factor. The kinetic factor ($\varepsilon_k = \varepsilon_{eq} + \varepsilon_{Dif}$) can be described as a combination of the equilibrium fractionation (ε_k) and diffusion (ε_{Dif}). The diffusive factor (ε_{Dif}) is evaluated in 8.4 for deuterium and 10.12 for oxygen-18 using experimental data described in the literature (Welhan and Fritz, 1977; Craig et al., 1963). Combining the effect of dilution, steam separation and evaporation at the surface, we obtain a slope ($S_{DSE}S_{DE}$) of the dilution-steam separation-evaporation line given by:

$$S_{DSE} = \frac{(\delta D_{Dil} + \delta D_{SS} + \varepsilon_{kD})}{(\delta^{18}O_{Dil} + \delta^{18}O_{SS} + \varepsilon_{k18O})} \qquad (2)$$

where water δD_{Dil} and $\delta^{18}O_{Dil}$ are the deuterium and oxygen isotopic compositions of the dilution from the aquifer A to B ($\delta_A - \delta_B$); δD_{SS} and $\delta^{18}O_{SS}$ the composition of the steam separation from δD_{Dil} $\delta^{18}O_{Dil}$ the aquifer B ($\delta_B - \delta_{SSB}$); and ε_{kD} of about 42.4‰ for deuterium and ε_{k18O} of about 15.7‰ are kinetic factors for water at 85°C estimated from the equilibrium fractionation (e.g., Horita et al., 2008), which are associated to evaporation. The slope S_{DSE} calculated with equation (2) is 2.2, which is similar to the slope calculated from the linear regression. Most of the isotopic data of the LB is distributed along the steam separation lines of the colder aquifer B, which would suggest the same diluted origin from aquifer B.

Low chloride/electrical conductivity waters were found in the marshy areas around the SE and VR. The isotopic composition of the SE thermal waters (Figure 5.3) form a line with the GW, and present a slope estimated at ~1.9. Previous studies (Giggenbach, 1978; Giggenbach and Stewart, 1982; Cortecci et al., 2005) attribute these waters to steady state evaporation of local meteoric water that had been heated by steam

from the hot reservoir. Similar to equation (2), the slope of steam heated waters (S_{SH}) can be calculated as (Giggenbach and Stewart, 1982):

$$S_{SH} = \frac{(\delta D_A - \delta D_{Gw} + \varepsilon_{kD})}{(\delta^{18}O_A - \delta^{18}O_{Gw} + \varepsilon_{k18O})} \qquad (3)$$

where δD_A and $\delta^{18}O_A$ correspond to the deuterium and oxygen isotopic composition of the main aquifer. Considering that the temperature of these features is slightly below the boiling point, we use same ε_{kD}, ε_{k18O} reported previously to calculate the slope. The slope calculated from equation (3) is 1.2, which is very close to that estimated by the linear regression. Additionally, chemical analysis in previous studies showed high sulfate water in this area (Giggenbach, 1978; Cortecci et al., 2005), suggesting some steam addition, and defining a slope of 1.6 using values of ε_{kD}, ε_{k18O} for 70°C Giggenbach, 1978; Giggenbach and Stewart, 1982; Cortecci et al., 2005).

Low chloride/electrical conductivity of thermal pools in VR show that >30% of local meteoric water is diluting water from the hot aquifer. The dilution might occur at shallow depth given that VR is a marsh, and the water table should be close to the surface. Continuous dilution at different depths was previously identified as one of the most important process affecting thermal features (Giggenbach, 1978; Giggenbach and Stewart, 1982) for samples collected at the end of the 1960s and beginning of the 1970s (e.g. Ellis, 1969; Cusicanqui et al., 1969; Giggenbach, 1978; Giggenbach and Stewart, 1982). Our samples collected in 2014 show <10% dilution at depth for the MB and LB, and shallow dilution <30% in VR (Figure 5.5b). This difference can be explained if the previous samples were collected during different seasons, or if there has been a reduction of local meteoric water input over time. We are not able to distinguish between these two possibilities with available data.

Even though models applied in equation (2) and (3) include many simplifications and have strong dependence on the conditions in the hot aquifer, they capture the main processes affecting the isotopic content of thermal waters, which are summarized in Figure 5.6. Additional constrains can be added, for example the evaporation effect calculated from the Rayleigh distillation equation neglects the relative humidity of the atmosphere, the isotopic composition of the atmosphere, and the effect of the wind. Additionally, erupted water from thermal sources can drain back to the conduit or infiltrate into the ground and return to the conduit. This recycling would increase the proportion of heavy isotopes. Geyser models describe a bubble trap that would add steam to the system to generate an eruption (e.g., Belousov et al, 2013; Vandemeulebrouck et al., 2014; Munoz-Saez et al, 2015ab). This steam addition, in contrast to recycling, would increase the input of light isotopes.

5.6.3 Mass Balance

The discharge channels that collect water from the basins are subjected to higher amounts of evaporation than thermal sources. The slope of the evaporation line from the isotopic data (S_E) can be determined from the Rayleigh equation (1)

$$S_E = \frac{\varepsilon_{kD}}{\varepsilon_{k18O}} \quad . \qquad (4)$$

Water in streams evaporate at lower temperature than the thermal waters (<35°C), and the kinetic fractionation factors are higher, about 74.4‰ for deuterium and ε_{k18O} of about 18.5‰ for oxygen. With these values the slope calculated for evaporation is closer to 4. The isotopic trend determined by the channel in the MB (Figure 5.5e) has a slope ~3.8, which is very close to the slope from equation (4).

The channel that collects water from UB, VR, and local meteoric water (GW) shows lower electrical conductivity than the thermal springs, and much closer to GW (Figure 5.2). However the isotopic composition of δ^{18}O and δD (Figure 5.5c) disagrees with a simple dilution of thermal water and GW, suggesting evaporation. The residual fraction of liquid (f) from evaporation can be calculated using

$$\delta_{intial} - \delta_{final} = \varepsilon \ln f \qquad (5)$$

where δ_{intial} and δ_{final} are the initial and final isotopic compositions of the water. Considering that the slope of the evaporation line is 4 (equation 4), the projection of this line onto the dilution line (Figure 5.5c) gives an initial composition of the water in the streams of -7.2‰ and -61‰, for δ^{18}O and δD respectively. We calculate that 6% evaporated. The discharge measured in the channel was 250 L/s (Figure 5.2d), so adding the evaporated fraction we estimate a total discharge of 267 cm^3/s. The initial composition on the dilution line indicates that about 39% local meteoric water dilutes about 61% thermal water.

The channel collecting water from the SE (Figure 5.5e sample #100) has high electrical conductivity and an isotopic composition enriched in heavy isotopes. The isotopic composition aligns with the thermal sources of the SE, suggesting that the same steam heating and evaporation process occur, but that the water in the channel has been cooled.

The discharge channels (samples #112 and # 113) from the MB have an electrical conductivity similar to the thermal sources (Figure 5.2), and the isotopic enrichment δ^{18}O and δD with respect to thermal sources (Figure 5.5d), suggests evaporation from the thermal sources and a small dilution with local meteoric water. Considering that the initial composition is close to the composition of the thermal waters (-6.4 and -69.5 for δ^{18}O and δD respectively), we estimate that the residual liquid fraction (equation 5) for the channel at the north (sample #112) is around 75%, and the total flow before evaporation was 20 L/s; the residual liquid fraction of the channel at the south is around 65%, which corresponds to 7.5 L/s before evaporation. Adding the flow from both channels, the water from the thermal sources of the MB would be at least 27.5 L/s.

Channels from the Tucle River (sample # 400) and the Salado River (sample # 1) also show evidence of evaporation from a thermal water diluted by meteoric water. Using equation (5), and the initial composition on the dilution line, we infer that the residual water after evaporation on Tucle River is about 93% and hence that the recharge before evaporation is 150 L/s. About 45% ground water dilutes the thermal water. The residual liquid of the Salado River would be about 85%, thus 1005 L/s recharged the river before evaporation, and 45% of ground water diluted the thermal water, which corresponds to 452 L/s of meteoric water and 553 L/s of thermal water.

The recharge from the Andean water and the mixing with magmatic water probably takes a long time before discharging at El Tatio. The absence of the tritium in thermal water are evidence that both the magmatic water and the meteoric water at high elevation are older than 1960 (nuclear tests). The local meteoric water instead has the highest tritium values, and the channels and thermal sources that show some degree of dilution with the local meteoric water also contain amounts of tritium above the detection limit. We note, however, that the values of tritium obtained in this study are lower than those reported in the literature (e.g., Cusicanqui et al., 1969).

5.6.4 Energy Balance

During the experiment the geyser skipped two eruptions but the periodic signal of pressure and temperature continued, confirming that the periodic addition of heat is coming from below and is not affected by conditions in the conduit. Eruptions resumed when the additional water in the conduit warmed enough to boil and erupt again. We calculated that ~ 3.8 x 10^4 kJ were needed to warm the 125 liters of added water from 15^{o}C to 86.6 ^{o}C (using $H_{erupted} = C_p mT$, and C_p=4.2 kJ kg^{-1} K^{-1}). We thus assume that warming occurred during two heat pulses of ~1.9 x 10^4 kJ each. In previous studies on El Jefe the estimation for temperate increases before the an eruption was 3^{o}C and the mass of erupted water was 110 kg (Munoz-Saez et al., 2015a), with these data we estimated that heat required for one eruption was one order of magnitude lower ~1.6 x 10^3 kJ. The present data suggests that about 90% of the heat added to the conduit is discharged as latent heat in vapor. Using a latent heat of steam of 2660 kJ/kg (for P_{air} and T_{boil}), the equivalent amount of steam added to the conduit was ~7 kg, and volume of steam required is ~17.6 m^3 (steam density of 0.4 kg/m^3), equivalent to a spherical cavity ~3.2 m in diameter. The total enthalpy of the erupted liquid plus steam in one eruption is equal to that in the same mass of water at about 122.6^{o}C. Given that the reservoir temperature is > 200^{o}C, the erupted water must be a combination of reservoir and cooler water, and/or loses heat during ascent. Other studies have similarly inferred that large amounts of enthalpy are lost between the deep reservoir and the surface (Karlstrom et al., 2013).

5.7 Conclusions

In the introduction we listed the three objectives of our study. We conclude by listing those objectives and our findings based on the data we collected.

- *Origin of the fluids:*

There two sources of meteoric water with different relative ages: 1) Old, high altitude Andean precipitation, which might have a distant zone of recharge that would take more than 50 years to reach the discharge zone. 2) Local meteoric water that infiltrates and is discharged in less than 50 years.

Mixing of old meteoric water from high altitude with magmatic water seems to be the most likely origin of the hot reservoir. Thermal sources in the UB seem to be generated from this mixing. The normal fault governs the location of the thermal sources permitting the mixing and then ascent of deep magmatic and distant Andean fluids.

- *Processes affecting the fluids:*

In the UB, perpetual spouters show a higher degree of the magmatic component and evaporation, while for geyser and hot pools, mixing and steam separation trends cannot be distinguished.

Continuous dilution of the hot aquifer with local meteoric water at different depths is insignificant. We only found evidence of dilution only in the second cooler aquifer and shallow dilution in VR.

Fountain geysers in the MB appear to result from the superposition of three processes: dilution of the hot aquifer at depth with local meteoric water up to 25%, steam separation as the fluid is rising from the diluted aquifer, and evaporation from pools exposed to the air.

Abundant thermal pools and mud pools in VR and SE can be associated with the shallow addition of local meteoric water. Those areas are marshes, suggesting that the water table is close to the surface.

- *Mass and energy balance*

Evaporation at $<35^{o}C$ can explain isotopic trends in the streams draining the basins. Water in discharge channels can lose as much as 30% of their water by evaporation.

Discharge channels collect water from the thermal features and local meteoric water, with different degrees of mixing. Channels from UB and LB have a higher amount of meteoric water. In the Salado River, 45% of the discharge can be attributed to the addition of local meteoric water.

About 10% of the mass of steam added to the conduit of a geyser is used to warm water to the eruption temperature and the rest is lost to the atmosphere.

The erupted water must be a combination of reservoir and cooler water, and/or loses heat during ascent.

5.8 Acknowledgments

This research was supported by the National Science Foundation (EAR1114184), CEGA-University of Chile, Conicyt-Chile, Center for Latin American Studies-University of California Berkeley, and the Judy Webb Chair. We thank those who provided essential help in the field: Angello Negri, Camilo Gonzalez, Alberto Ardid, Prof. Martin Reich and Prof. Emilio Vera. We acknowledge the U.S. Geological Survey laboratories in Menlo Park, California for the chemical analysis, and the U.S. Geological Survey Noble Gas Laboratory in Denver, Colorado for the tritium analysis. We thank Felipe Aguilera for the shape files provided for the geological map of El Tatio and Seth Saltiel for editing. The fieldwork was performed with the permission of the Amayras Communities of Caspana and Toconce.

5.9 Tables and Figures

Table 5.1: Field measurements and stable isotopes

ID	Latitude	Longitude	T(^{0}C)	pH	Cond	del ^{18}O	del D
0	-22°20'20.5"	-68°01'05.1"	36.3	7.8	7.4	-6.2	-58.3
1	-22°20'04.0"	-68°01'58.5"	30.5	7.9	8.2	-5.7	-55.4
2	-22°20'07.9"	-68°01'40.6"	61.4	6.6	11.8	-6.0	-70.0
3	-22°20'06.3"	-68°01'35.4"	86.3	7.5	11.8	-6.2	-71.4
4	-22°20'06.6"	-68°01'34.4"	81.8	6.8	11.8	-6.4	-72.0
5	-22°20'08.8"	-68°01'34.6"	83.5	6.5	11.5	-6.6	-73.3
6	-22°20'13.4"	-68°01'35.3"	85.6	7.3	12.3	-5.7	-68.5
7	-22°20'14.7"	-68°01'34.4"	86.7	7.6	12.2	-6.0	-70.1
8	-22°20'19.6"	-68°01'34.5"	74.3	7.1	11.4	-6.0	-71.3
9	-22°20'20.8"	-68°01'34.2"	68.2	7.5	11.2	-5.9	-70.4
10	-22°20'23.4"	-68°01'29.8"	86.6	7.2	12.9	-5.3	-71.1
11	-22°20'27.1"	-68°01'32.7"	83.7	7.2	11.6	-6.1	-72.3
12	-22°20'25.7"	-68°01'34.9"	86.1	7.5	12.3	-5.9	-70.8
13	-22°20'25.7"	-68°01'34.3"	85.9	7.6	12.0	-5.7	-71.6
14	-22°20'25.3"	-68°01'36.6"	86.8	7.4	12.4	-5.3	-68.0
15	-22°20'25.5"	-68°01'36.4"	71.9	7.4	12.4	-5.3	-68.8
16	-22°20'25.9"	-68°01'37.6"	84.8	7.5	12.7	-5.5	-69.3
17	-22°20'27.1"	-68°01'37.5"	82.3	7.6	12.1	-5.4	-68.3
100	-22°20'45.7"	-68°00'35.7"	21.2	7.9	12.1	-3.9	-61.4
101	-22°20'56.4"	-67°59'48.2"	83.1	7.1	0.7	-4.6	-51.6
102	-22°20'56.2"	-67°59'48.0"	81.4	7.7	0.7	-2.1	-49.0
103	-22°20'32.7"	-68°00'46.2"	86.5	7.3	14.2	-5.4	-67.7

104	-22°20'33.1"	-68°00'45.5"	84.2	6.8	13.9	-4.3	-65.8
105	-22°20'33.2"	-68°00'44.5"	86.4	7.4	14.6	-5.2	-67.6
106	-22°20'33.4"	-68°00'43.8"	74.7	7.0	15.2	-4.1	-65.7
107	-22°20'36.6"	-68°00'42.4"	86.2	7.0	14.0	-5.1	-66.9
108	-22°20'38.7"	-68°00'42.4"	84.6	7.2	14.0	-5.0	-67.0
109	-22°20'38.7"	-68°00'43.1"	86.7	7.2	14.3	-5.2	-68.0
110	-22°20'33.7"	-68°00'43.2"	84.6	7.3	14.4	-5.5	-68.3
111	-22°20'31.4"	-68°00'43.2"	86.4	7.3	11.9	-6.2	-69.5
112	-22°20'27.0"	-68°01'02.6"	23.8	7.3	13.9	-1.9	-53.4
113	-22°20'32.4"	-68°01'03.7"	21.4	7.2	14.4	-0.1	-46.4
201	-22°19'55.6"	-68°00'46.9"	85.8	7.7	16.8	-5.0	-70.9
202	-22°19'55.7"	-68°00'46.4"	83.2	7.4	13.6	-3.6	-65.2
203	-22°19'56.0"	-68°00'47.4"	86.1	6.8	17.4	-2.8	-64.1
204	-22°19'55.8"	-68°00'48.8"	86.6	7.3	15.5	-4.5	-68.6
205	-22°19'55.2"	-68°00'49.2"	82.0	7.0	15.2	-4.9	-70.8
206	-22°19'55.5"	-68°00'48.5"	87.1	7.0	15.3	-4.8	-70.1
207	-22°19'55.1"	-68°00'48.0"	71.9	7.1	14.8	-4.5	-70.2
208	-22°19'55.6"	-68°00'47.9"	86.6	7.2	14.5	-4.2	-69.4
209	-22°19'54.9"	-68°00'46.0"	86.5	6.7	18.9	1.2	-46.7
210	-22°19'55.2"	-68°00'45.9"	75.8	6.5	6.7	-7.4	-88.3
211	-22°19'57.0"	-68°00'46.6"	58.9	6.4	13.9	-2.2	-64.7
212	-22°19'57.4"	-68°00'47.0"	76.4	6.6	15.3	-5.0	-71.1
213	-22°20'00.0"	-68°00'47.7"	86.1	6.8	14.5	-5.0	-69.5
214	-22°19'59.9"	-68°00'47.4"	56.1	6.4	14.7	-3.9	-65.4
215	-22°20'00.4"	-68°00'47.0"	82.7	7.2	14.5	-5.0	-69.2
216	-22°19'59.2"	-68°00'46.6"	83.2	6.9	14.2	-4.9	-67.9
217	-22°19'58.7"	-68°00'46.3"	49.2	6.2	15.5	-4.1	-66.6
218	-22°19'56.8"	-68°00'43.9"	86.0	6.6	15.2	-4.9	-70.2
219	-22°19'57.0"	-68°00'43.9"	79.4	6.3	15.5	-4.6	-70.9
220	-22°19'54.7"	-68°00'45.2"	85.9	7.4	15.3	-5.1	-71.8
221	-22°19'54.2"	-68°00'44.9"	77.4	6.8	14.6	-4.5	-70.7
222	-22°19'54.2"	-68°00'44.8"	79.0	7.0	15.0	-4.7	-69.0
223	-22°19'53.8"	-68°00'43.0"	73.0	7.5	15.3	-4.9	-70.2
224	-22°19'53.2"	-68°00'42.4"	85.6	7.2	14.9	-4.9	-70.9
225	-22°19'41.4"	-68°00'22.7"	85.6	6.9	15.5	-4.6	-69.4
226	-22°19'41.4"	-68°00'22.7"	84.0	6.9	15.5	-4.6	-68.5
227	-22°19'41.4"	-68°00'22.0"	55.4	5.6	14.3	0.0	-56.6
228	-22°19'40.0"	-68°00'23.6"	66.2	6.4	6.2	-5.1	-68.5
229	-22°19'39.3"	-68°00'24.5"	79.8	6.4	13.1	-4.7	-68.3
230	-22°19'39.7"	-68°00'25.6"	65.3	6.8	2.9	-6.6	-66.4
231	-22°19'36.2"	-68°00'25.6"	77.3	6.6	0.2	-6.0	-64.0

232	-22°19'37.7"	-68°00'23.2"	70.7	6.1	5.6	-1.9	-57.6
233	-22°19'37.8"	-68°00'20.7"	70.1	5.4	11.9	-3.3	-65.3
234	-22°19'39.0"	-68°00'20.2"	63.6	6.2	0.7	-7.6	-78.0
235	-22°19'54.8"	-68°00'44.3"	84.3	6.3	14.0	-5.2	-71.8
236	-22°19'54.4"	-68°00'43.9"	70.5	7.3	14.1	-4.1	-68.7
237	-22°19'52.4"	-68°00'42.2"	86.5	7.4	14.4	-4.8	-69.8
238	-22°19'51.6"	-68°00'39.8"	86.4	7.4	14.7	-4.8	-68.6
239	-22°19'50.2"	-68°00'37.9"	86.5	7.5	14.0	-5.1	-70.8
240	-22°19'48.5"	-68°00'37.2"	83.0	7.3	14.1	-4.6	-70.6
241	-22°19'48.6"	-68°00'36.8"	86.8	7.4	14.3	-5.2	-71.4
242	-22°19'47.3"	-68°00'34.3"	81.3	7.5	14.6	-4.7	-68.9
243	-22°19'46.4"	-68°00'34.9"	82.6	7.3	14.5	-4.7	-69.6
301	-22°20'22.4"	-68°01'06.9"	86.4	7.4	11.3	-6.4	-69.1
401	-22°20'32.0"	-68°01'30.0"	86.6	7.7	11.9	-6.0	-70.1
402	-22°20'31.4"	-68°01'30.9"	68.4	7.4	10.0	-6.3	-70.2
403	-22°20'30.5"	-68°01'30.2"	38.9	8.3	3.8	-7.1	-57.8
GW	-22°20'00.2"	-68°00'30.8"	35.7	7.6	1.3	-9.1	-57.9
mp1	-22°20'56.0"	-67°59'48.5"	52.3				
mp10	-22°20'55.8"	-67°59'49.0"	84.6				
mp11	-22°20'56.0"	-67°59'48.7"	86.4				
mp12	-22°19'37.6"	-68°00'18.6"	39.6				
mp13	-22°19'37.4"	-68°00'21.9"	49.0				
mp14	-22°19'39.9"	-68°00'18.8"	49.2				
mp15	-22°19'39.8"	-68°00'19.5"	53.7				
mp16	-22°19'40.1"	-68°00'19.3"	55.1				
mp17	-22°19'40.6"	-68°00'21.3"	56.4				
mp18	-22°19'39.4"	-68°00'24.1"	56.9				
mp19	-22°19'37.2"	-68°00'20.5"	62.2				
mp2	-22°20'56.0"	-67°59'48.2"	65.3				
mp20	-22°19'37.5"	-68°00'24.7"	62.5				
mp21	-22°19'41.0"	-68°00'21.9"	66.3				
mp22	-22°19'37.3"	-68°00'22.8"	67.6				
mp23	-22°19'37.2"	-68°00'23.0"	68.9				
mp24	-22°19'40.0"	-68°00'19.6"	70.7				
mp25	-22°19'37.5"	-68°00'22.0"	71.3				
mp26	-22°19'39.1"	-68°00'24.4"	71.5				
mp27	-22°19'37.3"	-68°00'22.8"	71.8				
mp28	-22°19'37.7"	-68°00'22.4"	72.3				
mp29	-22°19'40.0"	-68°00'23.5"	73.0				
mp3	-22°20'56.0"	-67°59'48.4"	71.3				
mp30	-22°19'37.5"	-68°00'22.3"	73.6				

mp31	-22°19'37.6"	-68°00'22.5"	74.0				
mp32	-22°19'37.8"	-68°00'19.1"	76.4				
mp33	-22°19'40.1"	-68°00'19.8"	77.2				
mp34	-22°19'37.5"	-68°00'22.2"	77.6				
mp35	-22°19'37.0"	-68°00'23.2"	78.1				
mp36	-22°19'39.7"	-68°00'24.0"	79.4				
mp37	-22°19'41.0"	-68°00'21.6"	79.4				
mp38	-22°19'37.1"	-68°00'23.0"	81.2				
mp39	-22°19'36.9"	-68°00'23.5"	81.4				
mp4	-22°20'55.7"	-67°59'48.1"	73.9				
mp40	-22°19'40.7"	-68°00'21.7"	81.4				
mp41	-22°19'37.2"	-68°00'23.2"	82.1				
mp42	-22°19'37.6"	-68°00'22.4"	82.7				
mp43	-22°19'37.6"	-68°00'22.4"	82.8				
mp44	-22°19'40.7"	-68°00'21.1"	84.6				
mp45	-22°19'40.9"	-68°00'21.6"	84.6				
mp46	-22°19'37.0"	-68°00'22.3"	85.6				
mp47	-22°19'36.9"	-68°00'21.6"	86.4				
mp48	-22°19'37.5"	-68°00'22.5"	87.0				
mp49	-22°19'37.3"	-68°00"23.0"	87.2				
mp5	-22°20'56.1"	-67°59'48.1"	74.3				
mp50	-22°19'41.0"	-68°00'21.5"	87.5				
mp6	-22°20'56.1"	-67°59'47.8"	77.5				
mp7	-22°20'55.9"	-67°59'49.0"	79.5				
mp8	-22°20'55.7"	-67°59'47.9"	81.9				
mp9	-22°20'55.7"	-67°59'49.1"	84.2				

Table 5.2: Major elements

ID	Cl	F	SO_4	HCO_3	Ca	Na	K	Mg
0	3050	1.1	47.5	145.0	128.4	1974.0	217.7	7.6
1	3350	1.2	81.0	180.0	148.4	2030.8	180.3	12.4
100	5400	2.7	53.0	164.0	242.9	3235.7	155.1	10.8
112	7400	3.8	68.0	53.0	353.6	4329.7	222.5	5.7
113	8100	4.3	77.0	57.0	374.4	4653.1	236.2	6.9
225	8000	3.6	42.0	49.0	290.0	4604.2	597.9	0.6
231	1	0.1	22.0	44.0	7.1	20.1	2.9	0.4
403	1540	0.5	117.0	271.0	92.4	961.1	92.9	20.6
500	340	0.3	41.0	167.0	19.9	271.0	30.7	7.2
ID	**Li**	**Rb**	**Sr**	**Ba**	**Al (<)**	**As**	**SiO_2**	**B**
0	17.5	2.9	1.9	0.2	0.1	19.2	203.9	83.6
1	17.5	2.5	2.2	0.2	0.1	20.7	190.7	87.1
100	27.8	2.7	3.5	0.1	0.1	31.8	209.7	139.8
112	36.5	3.9	5.2	0.2	0.2	42.8	233.7	191.0
113	39.0	4.2	5.6	0.2	0.2	45.5	250.3	206.7
225	42.7	8.1	4.8	0.2	0.2	47.4	319.5	206.6
231	0.0	0.0	0.1	0.0	0.0	0.1	142.7	0.7
403	8.3	1.0	1.1	0.2	0.0	11.6	219.3	41.3
500	2.3	0.3	0.2	0.0	0.0	2.8	146.8	9.2

Table 5.3: Values of tritium isotope (H^3)

Dead samples correspond to values of H^3 <0.05 TU below the detection limit.

Sample	H^3	Error (TU)	Not Dead (> 0.05 TU)
ET-2-112	0.03	0.04	Dead
ET-2-000	0.14	0.04	Not Dead
ET-2-231	0.08	0.15	Dead
ET-2-113	0.18	0.05	Not Dead
ET-2-001	0.13	0.05	Not Dead
ET-2-403	-0.02	0.04	Dead
ET-2-100	0.04	0.04	Dead
GW	0.28	0.09	Not Dead
Blank	0.04	0.03	Dead

Figure 5.1: Geology of El Tatio geothermal field (modified from Marinovic and Lahsen, 1984)

Map shows structures, lithology, age of the deposits, types of features sampled, and sampled areas: upper basin (UP), Vega Rinconada (VR), middle basin (MB), southeast (SE), and lower basin (LB). We labeled sites sampled for major elements: sample #0 is the stream draining the UB and VR, #1 to Salado River, #110 is f drainage from the SE, #122 and #113 are drainages from the MB, and #400 is discharge in the Tucle River. In the VR area we sampled the geyser (sample #225) and one hot stream (sample #231). EJ shows the location of El Jefe geyser. Profiles abc are shown in Figure 6. Coordinates conform to the Universal Transverse of Mercator System (UTM), Datum WGS 84, and Zone 19S.

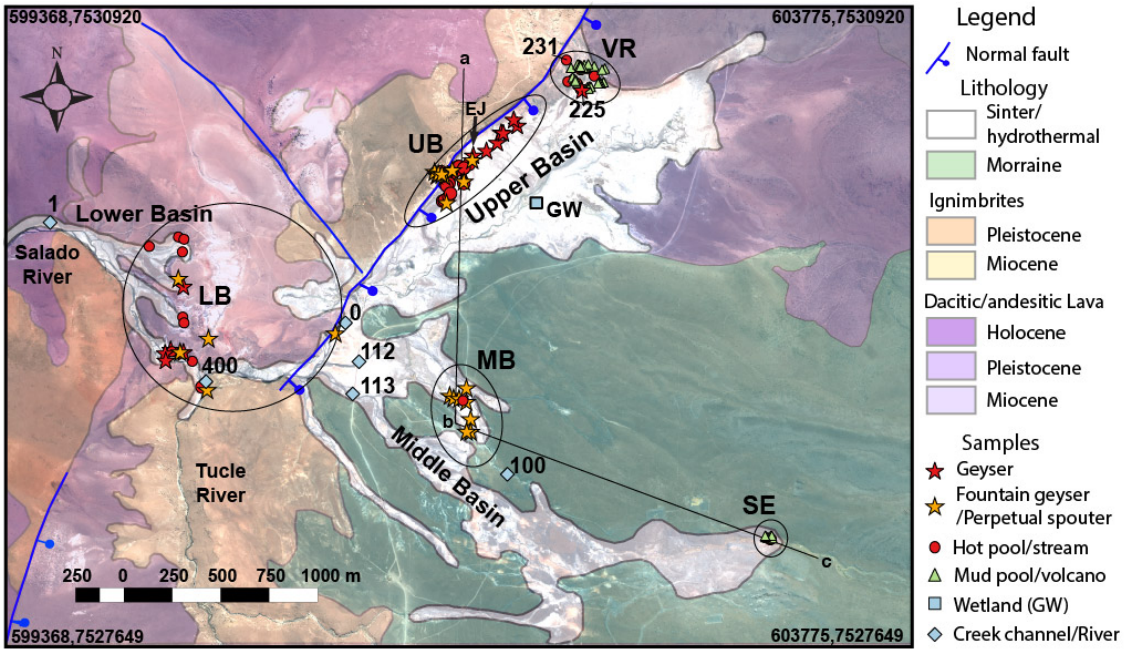

Figure 5.2: Field measurements

(a) temperature, (b) pH, (c) electrical conductivity, and (d) discharge plotted on a raster image of El Tatio area from Oct. 11, 2006 (DigitalGlobe Inc.), coordinates conform to the Universal Transverse of Mercator System (UTM), Datum WGS 84, and Zone 19S. Relationship between (e) pH and temperature, and (f) electrical conductivity and temperature in different areas. Legend (same Figure 1): stars are eruptive features; circles are hot pools and streams; diamonds are channels and rivers; square is a wetland (GW).

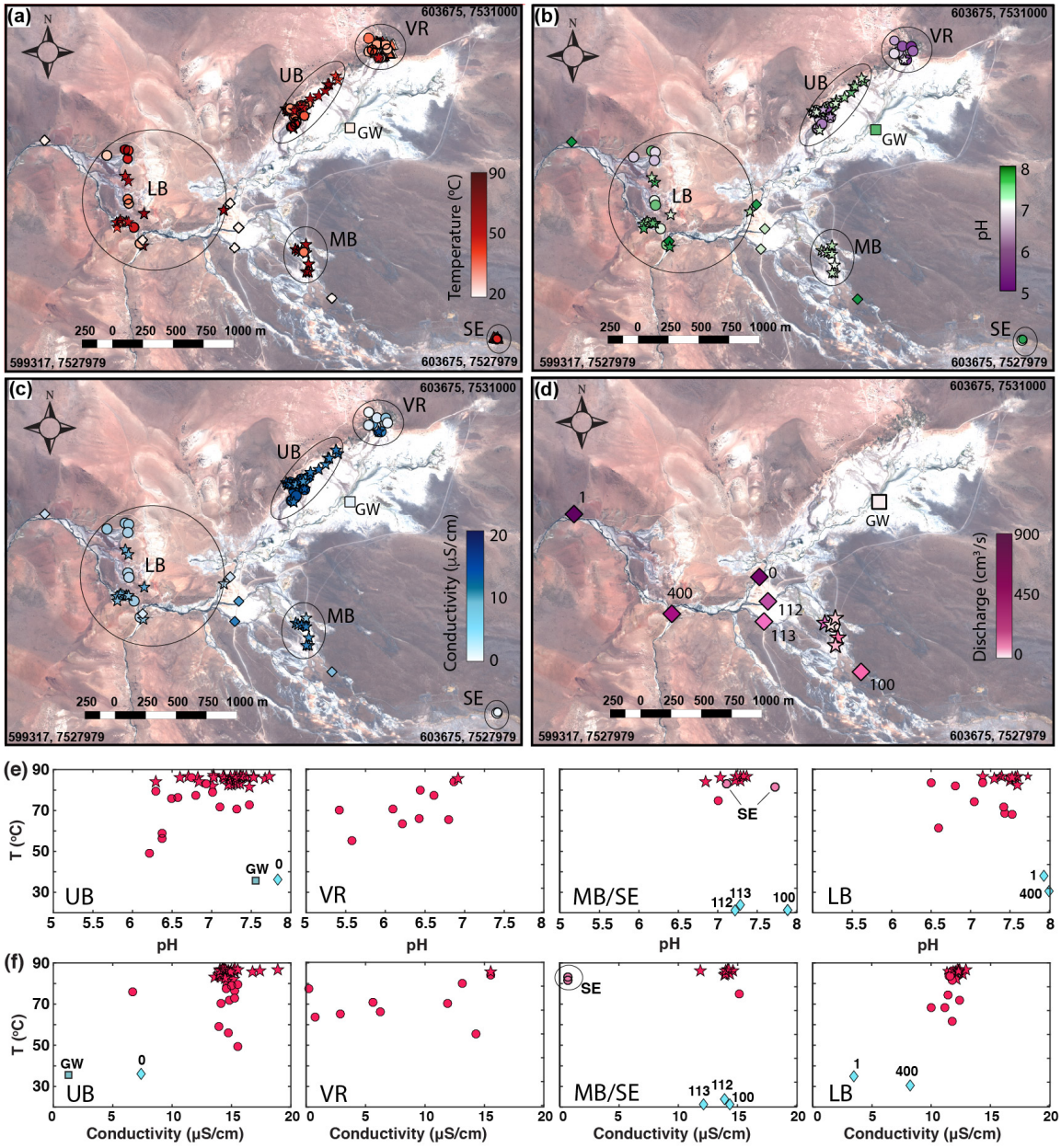

Figure 5.3: Distribution of stable isotopes

(a) $\delta^{18}O$ and (b) δD plotted on a raster image of El Tatio area from Oct. 11, 2006 (DigitalGlobe Inc.), coordinates conform to the Universal Transverse of Mercator System (UTM), Datum WGS 84, and Zone 19S. Relationship between (c) $\delta^{18}O$ and electrical conductivity, and (d) δD and electrical conductivity in different areas. We use the same legend as that in Figure 5.2.

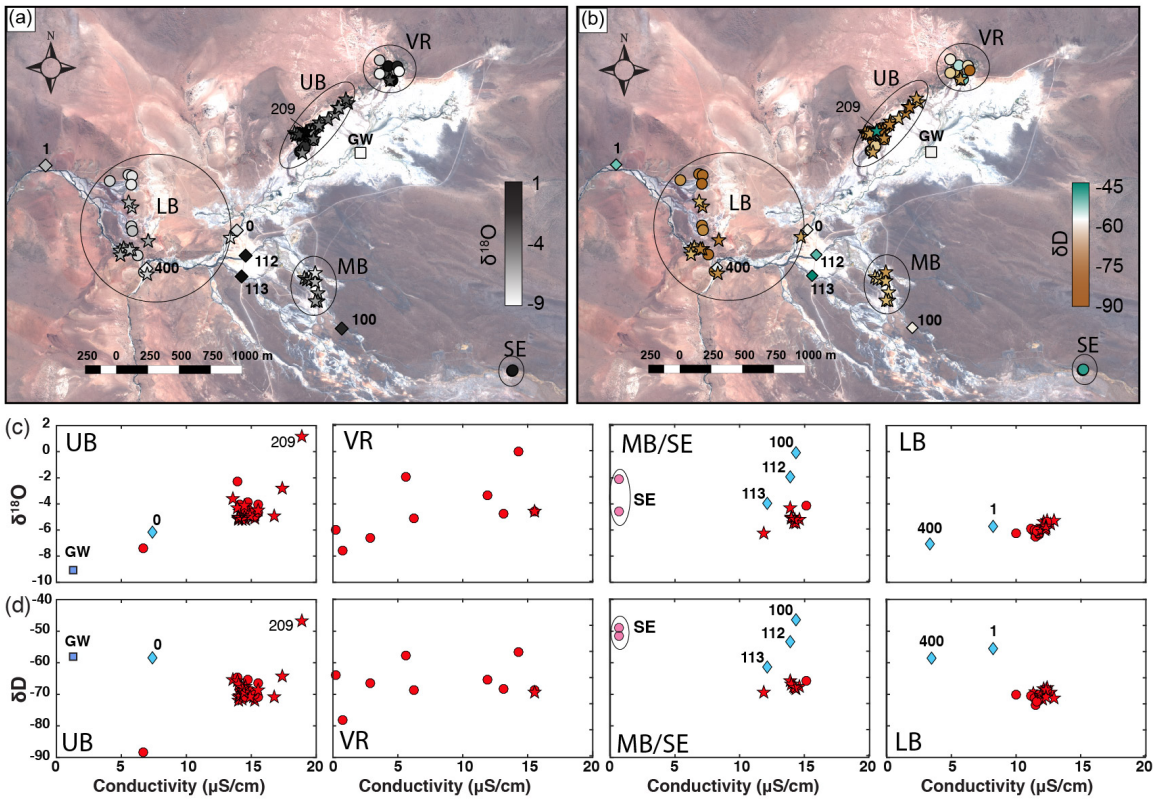

Figure 5.4: Experiment at El Jefe geyser

(a) Photo of the geyser erupting at the surface (time = 10s). (b) Photo of cold water being added to the geyser conduit (time = 170s). (c) Time series of the eruption at the surface on Oct. 8, 2004, staring at 15:45:52 UTC time; height 0.0 corresponds to the base of the geyser shown in the rectangle in panel (a). (d) Time series of pressure (*P*) and temperature (*T*) sensors inside the conduit 1.5 below the surface.

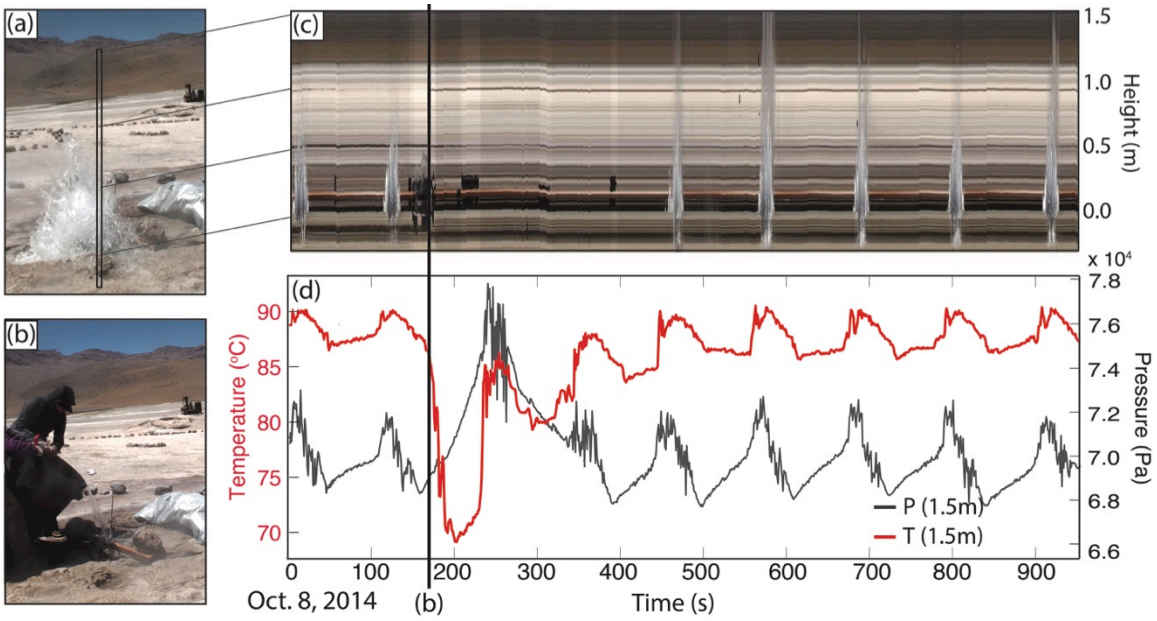

Figure 5.5: Stable isotopes (δ18O, δD) and interpretation of different processes affecting fluids

(a) Previous studies and (b) this study. Details from different areas in this study: (c) upper basin, (d) Vega Rinconada, (e) middle basin and southeast, and (f) lower basin. We use the same legend as in Figures 2 and 3. Line GMWL is the global meteoric line $\delta^{18}O = 8\ \delta D + 10$ (Craig, 1961), LMWL is the local meteoric line $\delta^{18}O = 8.15\ \delta D + 15.3$ (Aravena, 1995; Chaffaut et al., 1998). Isotopic composition of proposed deep aquifers (Giggenbach, 1978) are shown by white triangles labeled A, and B. Black crosses show the trajectory of compositions from continuous steam separation, departing from the initial composition of the aquifers and decreasing in 20°C steps until they reach to 90°C. White triangles labeled 85°C show the final composition of a single steam separation process. GW sample is the reference for meteoric water in this study, $\delta^{18}O = -9.08$ and $\delta D = -57.9$. The steam-heated line with slope 1.5 connects local meteoric water and andesitic water (AW) (Taran et al., 1989; Giggenbach and Soto, 1992). Mixing line connects a possible source of meteoric water of composition $\delta^{18}O$ about -14.6 and δD about -107, corresponding to water at 4,000 m of altitude (e.g., Mahon and Cusicanqui, 1980; Fritz et al., 1979; Cortecci et al., 2005) with andesitic water. We define an evaporation line of slope ~3.8 departing from the composition from steam separation.

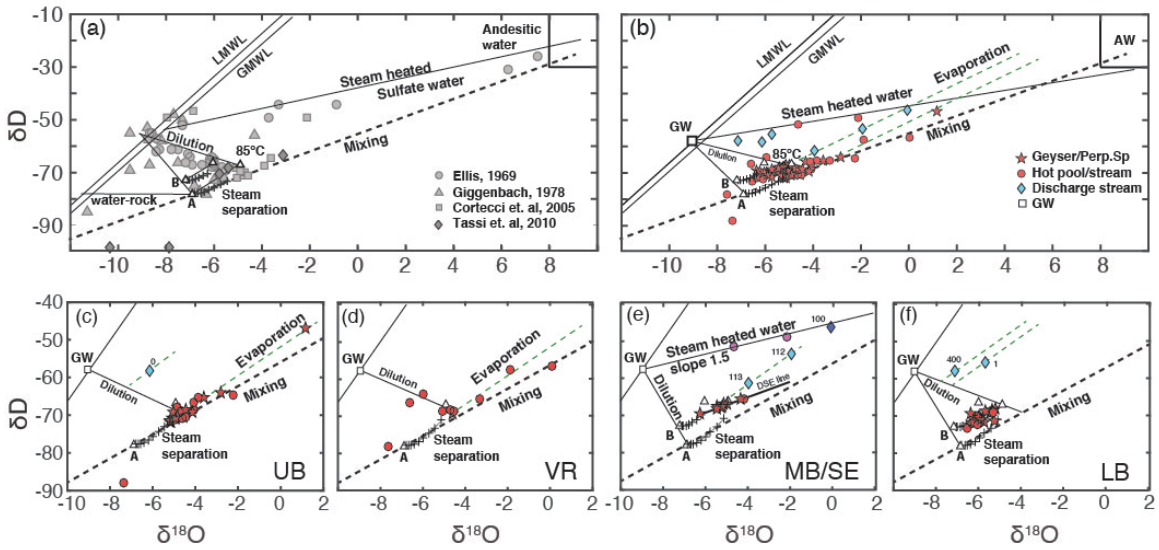

Figure 5.6: Conceptual model of El Tatio geothermal field

Summary of the main processes affecting the composition of the thermal fluids. The profile abc is in shown in figure 1; at the surface we indicate the lithological units defined in Figure 1. The profile ab runs from North to South from the UB to MB, while bc run from the MB to the SE, from North West to South East. The elevation is exaggerated by a factor of 4. The depth is not to scale; reference depth of 650 m depth is the location of the aquifers according to well data (e.g., Ellis, 1969; Cusicanqui et al, 1975)

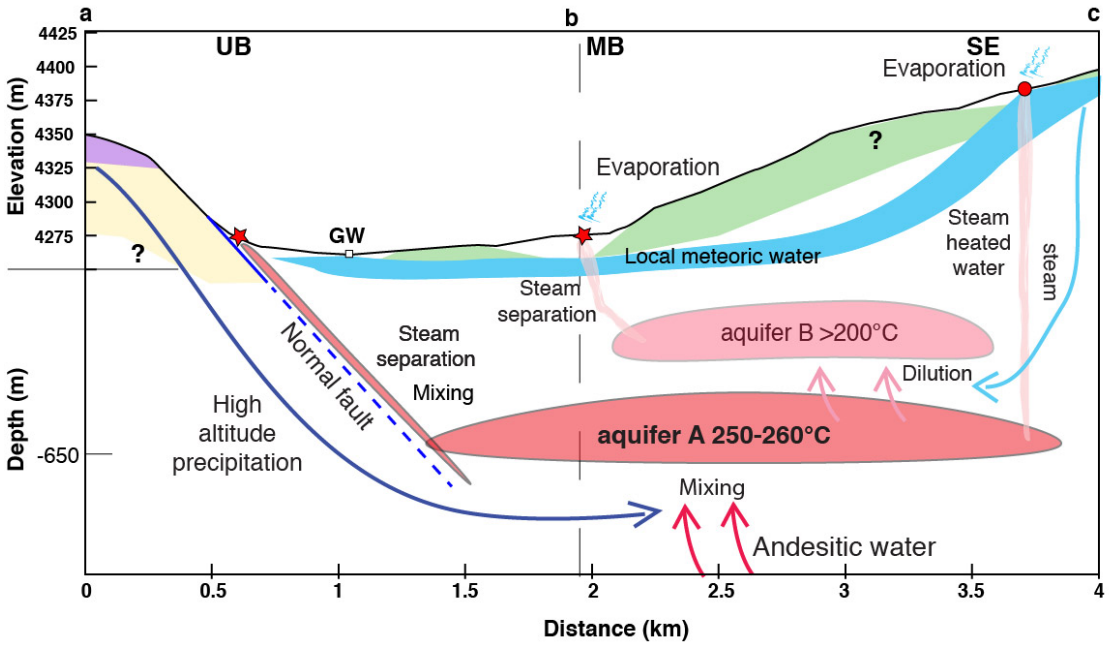

Chapter 6 Conclusions

Our study provided complete records of pressure and temperature inside geyser conduits during the entire eruption cycle, providing a unique dataset for natural geysers. This is the first study reporting hydraulic and physical rocks of sinter rocks.

In the introduction we listed a number of questions that were still unsolved about geyser systems that we aimed to address with the studies at El Tatio. Here we restate those questions and summarize some answers.

- What are processes and thermodynamic conditions in the conduit during the entire cycle? At what depth does the eruption begin?

A single reservoir dominates the recharge to the conduit of a geyser. The temperature remains within a few degrees of the boiling point at the surface; the pressure in the conduit is close to hydrostatic and increases as the conduits refills (Chapters 1 and 2). Rapid boiling of water occurs at the top of the water column by a sudden increase of temperature. As water is removed from the conduit the remaining water decompresses, causing the boiling front to propagate downward. Eruption terminates when the addition of steam has ceased.

- How is heat transported in geyser systems?

Thermal energy used in boiling during the eruption comes from steam ascending from depth. Convection may occur into the deeper part of conduit as steam is added (e.g., Vega Rinconada geyser, Chapter 2). Given that the water in the conduit is close to the boiling point, only a small part of the steam added to the conduit is used in the eruption, the rest is released to the atmosphere (e.g., El Jefe geyser, Chapters 1 and 4). The episodic addition of heat determinates the periodicity of geyser eruptions. A model in which cavities accumulate and release steam episodically is consistent with the observed addition of heat. The speed of propagation of pressure fluctuations in the conduit is similar to the sound speed for liquid and steam mixtures, suggesting that flow may be choked at vent, however there are large uncertainties in this inference (e.g., El Jefe geyser, Chapter 1).

- What is the geometry of subsurface permeable zones? How does this geometry affect the eruption process? Are geysers connected through permeable pathways to other thermal sources? How does this connection affect the eruption cycle? Do properties of sinter rocks play a role in the circulation of fluid?

The geometry underground controls the eruption style, given enough heat and sufficient water supply (Chapter 2). Geysers with deeper cavities and greater volume are more likely to have pre-play or minor eruptions. Non-eruptive hot springs seem to be disconnected from the heat supply or cavity, and the temperature remains constant. Geysers can be connected through permeable pathways to other nearby hot springs. Pressure changes in one geyser can be sensed in the others that are nearby (Chapter 2).

Sinter is a highly porous rock with a pore structure that resembles vesicular volcanic rocks. Permeability of sinter measured in the lab (Chapter 3) represents a lower bound on field values -- permeable zones are likely controlled by larger fractures.

- How and why does the geyser cycle evolve over time? How do external perturbation including earthquakes, atmospheric conditions, and Earth tides affect the eruption cycle?

From data over a one-week period in 2012 and 2014 (Chapters 1 and 2) we established no apparent effect of external conditions on the interval between eruptions (IBE) over that period. However, we observed annual changes of hydrogeological pathways. Between 2012 and 2014, we found differences of ~20% in the IBE of El Jefe geyser and we documented the appearance of new eruptive features. With this data we are not able to determine if changes occur progressively over time or are caused by discrete events as earthquakes or rainfall.

- What is the origin of the fluids? Do geysers and non-eruptive hot springs have the same origin?

The thermal waters of El Tatio are the product of different amounts of mixing between water from the reservoir and meteoric water, followed by steam separation, dilution and evaporation. Two different sources of meteoric water were found: old water (>50 years) from with precipitation at higher altitude in the Andean Mountains, and younger local meteoric water (<50 years). Perpetual spouters show more of the magmatic component and evaporation, while at geysers and hot pools, mixing and steam separation trends cannot be distinguished. Fountain geysers show evidences of greater dilution with local meteoric water, steam separation, and evaporation. Areas where the water table is close to the surface show abundant thermal pools and mud pools rather than eruptive features.

6.1 Future Research

Fundamental questions about geyser dynamics remain unsolved, including:

- Why do so few hot springs erupt as geysers? Why most geysers concentrated in few areas? How does geology control the distribution of thermal features?

The dynamics of eruptive features are dominated by geometric and thermodynamic complexities in the conduit and reservoir. These complexities are not required for non-eruptive hot springs. The proposed bubble trap model can explain some of the observations, but we have not been able to image the underground geometry that connects the deep aquifer and the outflow. The location of thermal sources seems to be controlled by normal faults that permit the circulation and ascent of deep fluids. Geophysical studies including seismic surveys and electrical resistivity tomography can be performed in order understand the geological and structural control on geyser formation.

- How do external perturbations including earthquakes, atmospheric conditions, and Earth tides affect the eruption cycle?

Some geysers seem to respond to external factors such as the dynamic stress from regional or distant earthquakes, and other geysers show seasonal eruption intervals controlled by the hydrological cycle and climate. Long term monitoring is required to separate internal and external controls on geyser periodicity.

- What is the longevity of geothermal systems?

Studying the evolution of sinter deposits over time, including constraints on sinter precipitation, the evolution rock properties, stratigraphy, textures, and ages of the deposits would provide additional insights into the dynamics of the vents and the longevity of geothermal systems. Additionally, numerical modeling can be useful to better understand vent migration, interaction between thermal sources, and the connection of geysers with deep aquifers.

Chapter 7 Bibliography

Adelstein, E., Tran A., Muñoz-Saez, C, Shteinberg, A., Manga, M. (2014). Geyser preplay and eruption in a laboratory model with a bubble trap. J. Volcanology Geothermal Research, in press.

Agnew, D. C. (2012). SPOTL: Some programs for ocean-tide loading.

Allen, E., and Day A. (1935), Hot springs of the Yellowstone National Park, Carnegie Inst. Washington Publ., 466, 525.

Amorsson, S., 2000. The quartz-and Na/K geothermometers. I. New thermodynamic calibration. In Proceedings of the World Geothermal Congress, pp. 929-934.

Aravena, R., 1995. Isotope hydrology and geochemistry of Northern Chile groundwaters. Bull. Inst. Fr. Études Andines 24, 497–503.

Archie, G.E., 1942. Electrical Resistivity Log as an Aid in Determining Some Reservoir Characteristics. Trans., AIME 146, 54-61.

Armbrust, G.A., Arias, J., Lahsen, A., Trujillo, P, 1974. Geochemistry of the hydrothermal alteration at the El Tatio geothermal field, Chile, IAVCEI Symposium Internacional de Volcanología, Santiago, Chile, 9-14 Septiembre 1974, pp.1-11.

Bassiouni, Z., 1994. Theory, measurement, and interpretation of well logs. SPE Textbook Series, Vol. 4.

Bayer, R., Schlosser, P., Bonisch, G., Rupp, H., Zaucker, F., Zimmek, G., 1989. Performance And Blank Components of a Mass Spectrometic System Routine Measurement of Helium Isotopes and Tritium by 3He Ingrowth Method, Sitzungsber. Heidelb. Akad. Wiss. Math. Naturwiss. Kl., 89, 44 pp., doi:10.1007/978-3-642-48373-8.

Benning, L.G., Phoenix, V.R., Yee, N., Konhauser, K.O., 2004. The dynamics of cyanobacterial silicification: an infrared microspectroscopic investigation. Geochim. Cosmochim. Acta 68, 743 – 757.

Berryman, J. G., 1980. Long-wavelength propagation in composite elastic media II. Ellipsoidal inclusions: J. Acoust. Soc. Am. 68, 1820–1831.

Bear, J., 2012. Hydraulics of groundwater. Courier Corporation.

Bear, J., 1972. Dynamics of Fluids in Porous Media, Elsevier, New York.

Belousov, A., Belousova, M., and Nechayev, A. (2013), Video observations inside conduits of erupting geysers in Kamchatka, Russia, and their geological framework: Implications for the geyser mechanism, Geology, 41, 387–390, doi:10.1130/G33366.1.

Birch, F., and G.C. Kennedy, 1972, Note on geyser temperatures in Iceland and Yellowstone National Park, in Heard, H.C., I.Y. Borg and C.B. Rayleigh, eds., Flow and Fracture of Rocks, American Geophysical Union Geophysical Monograph Series, 16, 329-336.

CHAPTER 7: BIBLIOGRAPHY

Blank, C.E., Cady, S.L., Pace, N.R., 2002. Microbial composition of near-boiling silicadepositing thermal springs throughout Yellowstone National Park. Appl. Environ. Microbiol. 68, 5123–5135.

Bott, T.L., Brock, T.D., 1969. Bacterial growth rates above 99 °C in Yellowstone hot springs. Science 164, 1411–1412.

Bloss, F. D., and Barth, T. F. W (1949), Observations on some Yellowstone geysers, Geol. Soc. Amer. Bull., 60, 861–886.

Braunstein, D., Lowe, D.R., 2001. Relationship between spring and geyser activity and the deposition and morphology of high temperature (73°C) siliceous sinter, Yellowstone National Park, Wyoming, U.S.A. J. Sediment. Res. 71, 747–763.

Bryan, T. S. (1995), The Geysers of Yellowstone, 463 pp., Univ. Press of Colorado, Boulder, Colorado.

Bunsen, R.W. (1847), Physikalische Beobachtungen uber die hauptsachlichsten Geysir Islands: Annalen der Physik und Chemie, 83, 159–170.

Cady, S.L., Farmer, J.D., 1996. Fossilization processes in siliceous thermal springs: trends in preservation along thermal gradients. In: Bock, G.R., Goode, G.A. (Eds.), pp. 150–173.

Cady, S.L., 2008. Hyperthermophilic biofilm mineralization; implications for biosignature detection. Geological Society of America, Abstracts with Programs 40(6), 295–296.

Campbell, K.A., Sannazzaro, K., Rodgers, K.A., Herdianita, N.R., Browne, P.R.L., 2001. Sedimentary facies and mineralogy of the Late Pleistocene Umukuri silica sinter, Taupo Volcanic Zone, New Zealand. J. Sediment. Res. 71, 727–746.

Campbell, K.A., Guido, D.M., Gautret, P., Foucher, F., Ramboz, C., Westall, F., 2015a. Geyserite in hot-spring siliceous sinter: window on earth's hottest terrestrial (paleo) environment and its extreme life. Earth-Sci. Rev. 148, 44–64. http://dx.doi.org/10.1016/j.earscirev.2015.05.009

Campbell, K.A., Lynne, B.Y., Handley, K.M., Jordan, S., Farmer, J.D., Guido, D.M., Foucher, F., Turner, S. and Perry, R.S., 2015b. Tracing Biosignature Preservation of Geothermally Silicified Microbial Textures into the Geological Record. Astrobiology, 15(10), pp.858-882.

Cassie, V., 1989. A taxonomic guide to thermally associated algae (excluding diatoms) in New Zealand. Bibliotheca Phycologica 78:1–159.

Chaika, C., Dvorkin, J., 1997. Ultrasonic velocities of opaline rocks undergoing silica diagenesis Geophysical Research Letters, 24, pp. 2039–2042.

Chaika, C., 1998, Physical Properties and Silica Diagenesis: Ph.D. thesis, Stanford University.

Chaffaut, I., Coudrain-Ribstein, A., Michelot, J.L., Pouyaud, B., 1998. Prècipitations d'altitude du Nord-Chile, origine des sources de vapeur et donnèes isotopiques. Bull. Inst. Fr. Études Andines 27, 367–384.

CHAPTER 7: BIBLIOGRAPHY

Chouet, B. (1992), A seismic model for the source of long-period events and harmonic tremor. Volcanic seismology. Springer Berlin Heidelberg, 133-156.

Cortecci, G., T. Boschetti, M. Mussi, C. H. Lameli, C. Mucchino, and M. Barbieri, 2005. New chemical and original isotopic data on waters from El Tatio geothermal field, northern Chile, Geochem. J., 39(6), 547–571.

Coleman, M.L., Shepherd, T.J., Durham, J.J., Rouse, J.E. and Moore, G.R., 1982. Reduction of water with zinc for hydrogen isotope analysis. Analytical Chemistry, 54(6), pp.993-995.

Compton, J.S., 1991. Porosity reduction and burial history of siliceous rocks from the Monterey and Sisquoc Formations, Point Pedernales area, California. Geological Society of America Bulletin, 103(5), pp.625-636.

Corbett, D.M., 1943. Stream-gaging procedure, a manual describing methods and practices of the Geological Survey (No. 888). US Govt. Print. Off.

Craig, H., 1961. Isotopic variations in meteoric waters. Science, 133: 1702-1703.

Craig, H., Gordon, L.I. and Horibe, Y., 1963. Isotopic exchange effects in the evaporation of water: 1. Low ‐ temperature experimental results. Journal of Geophysical Research, 68(17), pp.5079-5087.

Cusicanqui, H., Mahon, W. A. J. and Ellis, A. J. (1975), The geochemistry of the El Tatio geothermal field, Northern Chile. Second United Nations Symposium on the Development and Utilization of Geothermal Resources, 703–711, San Francisco.

Cusicanqui, H., Mahon, W.A.J., & Ellis, A.J. (1976), The geochemistry of the El Tatio geothermal field, northern Chile.In: Proc. 2nd U.N. Symposium on Geothermal Fields, Berkeley, California, 140 - 156.

Denlinger, R. P., Moran, S. C. (2014). Volcanic tremor masks its seismogenic source: Results from a study of noneruptive tremor recorded at Mount St. Helens, Washington. Journal of Geophysical Research: Solid Earth, 119(3), 2230-2251.

Ellis, A. J., 1969. Survey for geothermal development in Northern Chile. Preliminary geochemistry report, El Tatio geothermal field. UNDP-Report.

Epstein, S. and Mayeda, T., 1953. Variation of O18 content of waters from natural sources. Geochimica et cosmochimica acta, 4(5), pp.213-224.

Fabricius, I. L., 2007. Chalk: composition, diagenesis and physical properties. Geological Society of Denmark. Bulletin, 55, 97-128.

Fernandez-Turiel, J.L., Garcia-Valles, M., Gimeno-Torrente, D., Saavedra-Alonso, J., Martinez-Manent, S., 2005. The hot spring and geyser sinters of El Tatio, northern Chile. Sediment. Geol. 180, 125–147.

Fournier, R.O., Rowe, J.J., 1966. Estimation of underground temperatures from the silica content of water from hot springs and steam wells. Am. J. Sci. 264, 685–697.

Fournier, R. O. (1969), Old Faithful: A physical model, Science, 163, 304–305.

Fournier, R.O. and Truesdell, A.H., 1973. An empirical Na/K/Ca geothermometer for natural waters. Geochimica et Cosmochimica Acta, 37(5), pp.1255-1275.

CHAPTER 7: BIBLIOGRAPHY

Fournier, R.O., 1977. Chemical geothermometers and mixing models for geothermal systems. Geothermics, 5 (1-4), pp.41-50.

Fournier, R.O., 1979. A revised equation for the Na/K geothermometer. Geothermal Resources Council Transactions, 3, pp.221-224.

Fritz, P., Silva Heggings, C., Susuki, O. and Salati, E., 1979. Isotope hydrology in Northern Chile. Proc. IAEA-UNESCO Symposium on Isotope Hydrology, 19–23 June 1978, Neuherberg. IAEA, Vienna, Vol. 2, 525–544.

Fukutomi, T. A (1942a), New mechanism of the geyser I, Bull. Seism. Soc. Jpn., 14, 157–174.

Fukutomi, T. A (1942b), New mechanism of the geyser II, Bull. Seism. Soc. Jpn., 14, 189–202.

Garcia-Valles, M., Fernandez-Turiel, J.L., Gimeno-Torrente, D., Saavedra-Alonso, J., Martinez-Manet, S., 2008. Mineralogical characterization of silica sinters from the El Tatio geothermal field, Chile. Am. Mineral. 93, 1373–1383.

Giggenbach, W. F., 1978. The isotopic composition of waters from the El Tatio geothermal field, Northern Chile. Geochim. Cosmochim. Acta, 42, 979–988.

Giggenbach, W.F. and Stewart, M.K., 1982. Processes controlling the isotopic composition of steam and water discharges from steam vents and steam-heated pools in geothermal areas. Geothermics, 11(2), pp.71-80.

Giggenbach, W.F., 1988. Geothermal solute equilibria. derivation of Na-K-Mg-Ca geoindicators. Geochimica et cosmochimica acta, 52(12), pp.2749-2765.

Giggenbach, W.F. and Soto, R.C., 1992. Isotopic and chemical composition of water and steam discharges from volcanic-magmatic-hydrothermal systems of the Guanacaste Geothermal Province, Costa Rica. Applied geochemistry, 7(4), pp.309-332.

Glennon, J. A., and Pfaff, R. M., 2003. The extraordinary thermal activity of El Tatio Geyser Field, Antofagasta Region, Chile, GOSA Trans., 8, 31–78.

Gonfiantini, R., Roche, M.A., Olivry, J.C., Fontes, J.C. and Zuppi, G.M., 2001. The altitude effect on the isotopic composition of tropical rains. Chemical Geology, 181(1), pp.147-167.

Guido, D.M., Campbell, K.A., 2009. Jurassic hot-spring activity in a fluvial setting at La Marciana, Patagonia, Argentina. Geol. Mag. 146, 617–622.

Guido, D.M., Campbell, K.A., 2014. A large and complete Jurassic geothermal field at Claudia, Deseado Massif, Santa Cruz, Argentina. J. Volcanol. Geotherm. Res. 275, 61–70.

Guidry, S.A., Chafetz, H.S., 2003. Anatomy of siliceous hot spring examples from Yellowstone National Park, Wyoming, U.S.A. Sediment. Geol. 157, 71–106.

Handley, K.M., Campbell, K.A., Mountain, B.W., Browne, P.R.L., 2005. Abiotic–biotic controls on the origin and development of spicular sinter: in situ growth experiments, Champagne Pool, Waiotapu, New Zealand. Geobiology 3, 93–114.

Healy, J. (1974) Geological report on El Tatio geothermal field, Antofagasta province, Chile. UNDP-Report.

CHAPTER 7: BIBLIOGRAPHY

Herdianita, N.R., Browne, P.R.L., Rodgers, K.A., Campbell, K.A., 2000. Mineralogical and textural changes accompanying ageing of silica sinter. Mineral. Deposita 35, 48-62.

Hinman, N.W. and Lindstrom, R.F., 1996. Seasonal changes in silica deposition in hot spring systems. Chem. Geol., 132, 237-246.

Honeywell Sensing and Control. N.p., n.d. Web. 09 Sept. 2015. http://images.vnsky.com/upfile/pdf/2013020904/55a6fbb8-0f96-42f8-8ca1-fc646537bfea.pdf

Horita, J., Rozanski, K. and Cohen, S., 2008. Isotope effects in the evaporation of water: a status report of the Craig–Gordon model. Isotopes in environmental and health studies, 44(1), pp.23-49.

Huber, R., Eder, W., Heldwein, S., Wanner, G., Huber, H., Rachel, R., Stetter, K.O., 1998. Thermocrinis ruber, gen. nov., sp. nov., a pink-filament-forming hyperthermophilic bacterium isolated from Yellowstone National Park. Appl. Environ. Microbiol. 64, 3576–3583.

Hurwitz, S., Kumar, A., Taylor, R., Heasler, H., (2008) Climate-induced variations of geyser periodicity in Yellowstone National Park, USA, Geology, 36, 451-454.

Hurwitz, S., Hunt, A.G., Evans, W.C., (2012) Temporal variations of geyser water chemistry in the Upper Geyser Basin, Yellowstone National Park, USA. Geochemistry Geophysics Geosystems, 13, Q12005, doi:10.1029/2012GC004388.

Hurwitz, S., Sohn, R.A., Luttrell, K., Manga, M. (2014) Triggering and modulation of geyser eruptions in Yellowstone National Park by earthquakes, earth tides, and weather. Journal of Geophysical Research, in press, doi: 10.1002/2013JB010803.

Hurwitz, S., Lowenstern, J.B. (2014), Dynamics of the Yellowstone Hydrothermal System, Reviews of Geophysics, 51, doi:10.1002/2014RG000452

Husen et al. (2004a), Changes in geyser eruption behavior and remotely triggered seismicity in Yellowstone National Park produced by the 2002M 7.9 Denali Fault earthquake, Alaska, Geology, 32, 537–540, doi:10.1130/G20381.

Husen, S., S. Wiemer, and R. B. Smith (2004b), Remotely triggered seismicity in the Yellowstone National Park region by the 2002 Mw 7.9 Denali Fault earthquake, Alaska, Bull. Seismol. Soc. Am., 94, S317–S331.

Hutchinson, R.A., 1985, Hydrothermal changes in the upper Geyser Basin, Yellowstone National Park, after the 1983 Borah Peak, Idaho, earthquake, in Stein, R.S., and Bucknam, R.C., eds., Proceedings of Workshop 28—On the Borah Peak, Idaho, earthquake: U.S. Geological Survey Open-File Report OF 85–0290-A, 612–624.

Hutchinson, R. A., Westphal, J. A., and Kieffer, S. W. (1997), In situ observations of Old Faithful Geyser, Geology, 25, 875–878.

Ingebritsen, S.E., and Rojstaczer, S.A. (1993), Controls on geyser periodicity: Science, 262, 889–892, doi: 10.1126/science.262.5135.889.

Ingebritsen, S.E., and Rojstaczer, S.A. (1996), Geyser periodicity and the response of geysers to deformation: Journal of Geophysical Research, 101, 21,891–21,905, doi: 10.1029/96JB02285.

Isaacs, C.M., 1981. Porosity reduction during diagenesis of the Monterey Formation, Santa Barbara coastal area, California. In Garrison, R. E., and Douglas, R. G., eds., The Monterey Formation and related siliceous rocks of California: Los Angeles, Pacific Section, Society of Economic Paleontologists and Mineralogists, p. 257–271.

Johnson, J. B., and Ripepe, M. (2011). Volcano infrasound: A review. Journal of Volcanology and Geothermal Research, 206(3), 61-69.

Jones, B., Renaut, R.W., 2004. Water content of opal-A: implications for the origin of laminae in geyserite and sinter. J. Sediment. Res. 74, 117–128.

Jones, B., Renaut, R.W., Rosen, M.R., 2003. Silicified microbes in a geyser mound: the enigma of low-temperature cyanobacteria in a high-temperature setting. Palaios 18, 87–109.

Jones, B., Renaut, R.W., Rosen, M.R., 2000. Stromatolites forming in acidic hot-spring waters, North Island, New Zealand. Palaios 15, 450–475.

Jones, B., Renaut, R.W. 1997. Formation of silica oncoids around geysers and hot springs at El Tatio, northern Chile. Sedimentology, 44: 287–304.

Jones, B., Renaut, R.W. 1996. Influence of thermophilic bacteria on calcite and silica precipitation in hot springs with water temperatures above 90 °C; evidence from Kenya and New Zealand. Canadian Journal of Earth Sciences, 32: 72–83.

Karlstrom, L., Hurwitz, S., Sohn, R. A., Vandemeulebrouck, J., Murphy, F., Rudolph, M. L., Johnston, M. J. S., Manga, M., and McCleskey, R. B. (2013), Eruptions at Lone Star Geyser, Yellowstone National Park, USA, Part 1: Energetics and eruption dynamics, J. Geophys. Res. Solid Earth, 118,1–15, doi:10.1002/jgrb.50251.

Kedar, S., Kanamori, H. and Sturtevant B. (1998), Bubble collapse as the source of harmonic tremor at Old Faithful Geyser, J. Geophys. Res., 103,24,283–224,299, doi:10.1029/98JB01824.

Kieffer, S. W. (1984), Seismicity at Old Faithful Geyser: An isolated source of geothermal noise and possible analogue of volcanic seismicity, Journal of Volcanology and Geothermal Research, 22, 59–95.

Kieffer, S. W. (1989), Geologic nozzles, Rev. Geophys, 27, 3–38, doi:10.1029/RG027i001p00003.

Kim, J.M., and Parizek R.R. (1997), Numerical simulation of the Noordbergum effect resulting from groundwater pumping in a layered aquifer system, Journal of Hydrology, 202, 231-243. doi:10.1016/S0022-1694(97)00067-X.

Kinsler, L.E., Frey, A.R., Coppens, A.B., and Sanders J.V. (1982) Fundamentals of Acoustics, 3rd Edition, Wiley, New York.

Kiryukhin, A. V., T. V. Rychkova, and I. K. Dubrovskaya (2012), Formation of the hydrothermal system in Geysers Valley (Kronotsky Nature Reserve, Kamchatka)

and triggers of the Giant Landslide, Appl. Geochem., 27, 1753–1766, doi:10.1016/j.apgeochem.2012.02.011.

Konhauser, K.O., Ferris, F.G., 1996. Diversity of iron and silica precipitation by microbial mats in hydrothermal waters, Iceland: implications for Precambrian iron formations. Geology 24, 323–326.

Konhauser, K.O., Phoenix, V.R., Bottrell, S.H., Adams, D.G., Head, I.M., 2001. Microbial–silica interactions in modern hot spring sinter: possible analogues for some Precambrian siliceous stromatolites. Sedimentology 48, 415–433.

Konhauser, K.O., Jones, B., Reysenbach, A., Renaut, R.W., 2003. Hot spring sinters: keys to understanding Earth's earliest life forms. Can. J. Earth Sci. 40, 1713–1724.

Kuster, G.T., and Toksoz, M.N., 1974, Velocity and attenuation of seismic waves in two-phase media. Part I. Theoretical formulations: Geophysics, v. 39, p. 587–606.

Lahsen, A. and Trujillo, P. (1975), El Tatio Geothermal Field. Proc. of the Second United Nations Symposium on the Development and Use of Geothermal Resources, 157–178, San Francisco, California, May 20–29, 1975.

Lahsen, A. (1976a), La actividad geotermal y sus relaciones con la tectónica y el volcanismo en el norte de Chile. I Congreso Geológico Chileno, Actas, B105 – B127. Antofagasta

Lahsen, A. (1976b), Geothermal exploration in Northern Chile-Summary. Circum Pacific Energy and Mineral Resources Conference, 169 – 175. Honolulu.

Lahsen, A., Trujillo, P., 1976. El campo geotermico de El Tatio, Chile. Proyecto Geotermico CORFU-ONU. Internal Report.

Landrum, J.T.; Bennett, P.C.; Engel, A.S.; Alsina, M.A.; Pastén, P.A.; Milliken,K., 2009. Partitioning geochemistry of arsenic and antimony, El Tatio Geyser Field, Chile. Applied Geochemistry 24, 664-676.

Lowe, D.R., Braunstein, D., 2003. Microstructure of high-temperature (>73 ◦C) siliceous sinter deposited around hot springs and geysers Yellowstone National Park: the role of biological and abiological processes in sedimentation. Canadian Journal of Earth Sciences 40, 1611–1642.

Lowe, D.R., Anderson, K.S., Braunstein, D., 2001. The zonation and structuring of siliceous sinter around hot springs, Yellowstone National Park, and the role of thermophilic bacteria in its deposition. In: Reysenbach, A.M., Voytech, M., Mancinelli, R. (Eds.), Thermophiles: Biodiversity, Ecology and Evolution. Kluwer Academic/Plenum Publishers, New York, pp. 143–166.

Lu, X., and S.W. Kieffer (2009), Thermodynamics and mass transport in multicomponent multiphase H2O systems of planetary interest, Ann. Rev. Earth Planet. Sci., 37, 449–77.

Lucas, L.L. and Unterweger, M.P., 2000. Comprehensive review and critical evaluation of the half-life of Tritium. Journal of research-National institute of standards and technology, 105(4), pp.541-550.

Lynne, B.Y., 2012. Mapping vent to distal-apron hot spring paleo-flow pathways using siliceous sinter architecture. Geothermics 43, 3–24.

Lynne, B.Y., Morata, D., and Reich, M., 2012. High Versus Low Altitude Hot Spring Settings and Associated Sinter Textures from El Tatio, Chile, and the Taupo Volcanic Zone, New Zealand. Geothermal Resources Council Transactions, v. 36, pp. 925-929.

Lynne, B.Y., Campbell, K.A., Moore, J.N., Browne, P.R.L., 2008. Origin and evolution of the Steamboat Springs siliceous sinter deposit, Nevada, U.S.A. Sedimentary Geology, 210, pp. 111–131.

Lynne, B.Y., Campbell, K.A., Moore, J., Browne P.R.L., 2005. Diagenesis of 1900-year-old siliceous sinter (opal-A to quartz) at Opal Mound, Roosevelt Hot Springs, Utah, U.S.A. Sedimentary Geology, 119, pp. 249–278.

Lynne, B.Y. and Campbell, K.A., 2003. Diagenetic transformations (opal-A to quartz) of low- and mid-temperature microbial textures in siliceous hot-spring deposits, Taupo Volcanic Zone, New Zealand. Canadian Journal of Earth Sciences, 40:1679-1696.

Mackenzie, G. (1811), Travels in the Island of Iceland, Edinburgh, vol. 27, Alam and Company, Edinburgh.

Mahon, W.A.J. and Cusicanqui, H., 1980. Geochemistry of the Puchuldiza and Tuja hot springs, Chile. NZJ Sci, 23, pp.149-159.

Mallon, A.J., Swarbrick, R.E. and Katsube, T.J., 2005. Permeability of fine-grained rocks: New evidence from chalks. Geology, 33(1), pp.21-24.

Manga, M., and E.E. Brodsky (2006), Seismic triggering of eruptions in the far field: volcanoes and geysers, Ann. Rev. Earth Planetary Sci., 34, 263-291.

Manga, M., Beresnev, I., Brodsky, E.E., Elkhoury, J.E., Elsworth, D., Ingebritsen, S.E., Mays, D.C., and Wang, C.-Y. (2012), Changes in permeability by transient stresses: Field observations, experiments and mechanisms, Reviews of Geophysics, 50, RG2004, doi:10.1029/2011RG000382.

Marler, G. D. (1951), Exchange of function as a cause of geyser irregularity [Wyoming], Am. J. Sci., 249, 329–342, doi:10.2475/ajs.249.5.329.

Marler, G. D. (1964), Effects of the Hebgen Lake earthquake of August 17, 1959 on the hot springs of the Firehole geyser basins, Yellowstone National Park, U.S. Geol. Surv. Prof. Pap., 435, 185.

Marler, G. D., and D. E. White (1975), Seismic Geyser and its bearing on the origin and evolution of geysers and hot springs of Yellowstone National Park, Geol. Soc. Am. Bull., 86, 749–759.

Marinovic, N., Lahsen, A., 1984. Hoja Calama: región de Antofagasta: carta geológica de Chile 1: 250.000. Servicio Nacional de Geología y Minería, Chile

Mavko, G., T. Mukerji, and J. Dvorkin, 1998, The rock physics handbook: Tools for seismic analysis in porous media: Cambridge University Press.

McSkimin, H.J., Andreatch Jr, P. and Thurston, R., 1965. Elastic moduli of quartz versus hydrostatic pressure at 25 and− 195.8 C. Journal of Applied Physics, 36(5), pp.1624-1632.

Merzhanov, A. G., A. S. Shteinberg, and G. S. Shteinberg (1990), Heat and mass exchange in geyser systems, in Proceedings of the 9th International Heat Transfer Conference, edited by G. Hestroni, 323–328.

Mountain, B. W., L. G. Benning, and J. A. Boerema. 2003. Experimental studies on New Zealand hot spring sinters: Rates of growth and textural development:. Canadian Journal of Earth Sciences 40:1643–1667.

Munoz, M., and V. Hamza (1993), Heat flow and temperature gradients in Chile, Studia Geoph. Et Geod. , 37, 315–348.

Munoz-Saez, C., Manga, M., Hurwitz, S., Rudolph, M., Namiki., A., Wang, C.-Y., 2015a. Dynamics within geyser conduits, and sensitivity to environmental perturbations: Insights from a periodic geyser in the El Tatio geyser field, Atacama Desert, Chile. Journal of Volcanology and Geothermal Research, 292, 41–55, doi:10.1016/j.jvolgeores.2015.01.002.

Munoz-Saez, C., Namiki, A., Manga, M., 2015b. Geyser eruption intervals and interactions: examples from El Tatio, Atacama, Chile, Journal of Geophysical Research, vol. 120, doi: 10.1002/2015JB012364.

Namiki, A., Munoz-Saez, C., Manga, M., (2014). El Cobreloa: A geyser with two distinct eruption styles. Journal of Geophysical Research, 119, doi:10.1002/2014JB11009.

Nicolau, C. Reich, M., Lynne, B. (2014) Physico-chemical and environmental controls on siliceous sinter formation at the high-altitude El Tatio geothermal field, Chile. Journal of Volcanology and Geothermal Research, 282, 60–76, doi: 10.1016/j.jvolgeores.2014.06.012.

Nishimura, T., M. Ichihara, and S. Ueki (2006), Investigation of the Onikobe geyser, NE Japan, by observing the ground tilt and flow parameters, Earth Planets Space, 58, e21–e24.

Nur, A., Mavko, G., Dvorkin, J. and Galmudi, D., 1998. Critical porosity: A key to relating physical properties to porosity in rocks. The Leading Edge, 17(3), pp.357-362.

Nur, A., Mavko, G., Dvorkin, J., and Galmundi, D., 1995, Critical porosity: the key to relating physical properties to porosity in rocks: Proc. 65th Ann Int. Meeting Soc. Expl. Geophys., 878.

Nur, A., Marion, D., and Yin, H., 1991, Wave velocities in sediments in Hovem, J., Richardson, M. D., and Stoll, R. D., Eds., Shear Waves in Marine sediments: Kluwer Academic, 131-140.

Nguyen, C.T., Gonnermann, H.M., Houghton, B.F., 2014. Explosive to effusive transition during the largest volcanic eruption of the 20th century (Novarupta 1912, Alaska). Geology 42 (8), 703–706.

O'Connell, R. J., Budiansky, B., 1974. Seismic velocities in dry and saturated cracked solids. J. Geophys. Res., 79(35), 5412–5426, doi:10.1029/JB079i035p05412.

ONEMI, National Office of Emergency of the Interior Ministry, Chile (2013), Monitoreo actualizado de Alerta Roja Comunal por precipitaciones en San Pedro de Atacama. Web. February 7, 2013 http://www.onemi.cl/informate/monitoreo-actualizado-de-alerta-roja-comunal-por-precipitaciones-en-san-pedro-de-atacama/.

Omega Thermocouple Home Page. Thermocouple Probes. N.p., n.d. Web. 09 Sept. 2015. http://www.omega.com/thermocouples.html

Pierson, B.K., Castenholz, R.W., 1974. A phototrophic gliding filamentous bacterium of hot springs, Chloroflexus aurantiacus. Arch. Microbiol. 100, 5–24.

Phoenix, V. R., Bennett, P. C., Engel, A. S., Tyler, S. W. and Ferris, F. G., 2006. Chilean high-altitude hot-spring sinters: a model system for UV screening mechanisms by early Precambrian cyanobacteria. Geobiology, 4: 15–28. doi:10.1111/j.1472-4669.2006.00063.x

Renaut, R.W., Jones, B., and Le Turdu, C. 1999. Calcite lilypads and ledges at Lorusio Hot Springs, Kenya Rift Valley: travertine precipitation at the air–water interface. Canadian Journal of Earth Sciences, 36: 649–666.

Rice, C.M., Trewin, N.H., Anderson, L.I., 2002. Geological setting of the Early Devonian Rhynie cherts, Aberdeenshire, Scotland: an early terrestrial hot-spring system. J. Geol. Soc. Lond. 159, 203–214.

Rodgers, K.A. and Cressey, G., 2001. The occurrence, detection and significance of moganite (SiO2) among some silica sinters. Mineralogical Magazine, 65, 157-167.

Rinehart, J. S., and A. Murphy (1969), Observations on pre- and post-earthquake performance of Old Faithful geyser. Journal of Geophysical Research, 74, 574–575.

Rinehart, J.S. (1972), Fluctuations in geyser activity caused by variations in Earth tidal forces, barometric pressure, and tectonic stresses. Journal of Geophysical Research, 77, 342–350, doi: 10.1029/JB077i002p00342.

Rinehart, J. S. (1980), Geysers and Geothermal Energy, Springer-Verlag, New York.

Rojstaczer, S., Galloway, D.L., Ingebritsen, S.E., and Rubin, D.M. (2003), Variability in geyser eruptive timing and its causes; Yellowstone National Park: Geophysical Research Letters, 30, no. 18, 1953, doi: 10.1029/2003GL017853.

Rodgers, K.A., Greatrex, R.,Hyland, M., Simmons, S.F., Browne, P.R.L., 2002. A modern evaporitic occurrence of teruggite, Ca4MgB12As2O28 · 18H2O, and nobleite, CaB6O10 · 4H2O, from the El Tatio geothermal field, Antofagasta Province, Chile. Mineral. Mag. 66, 253–259.

Rodgers, K.A., Browne, P.R.L., Buddle, T.F., Cook, K.L., Greatrex, R.A., Hampton, W.A.,Herdianita, N.R., Holland, G.R., Lynne, B.Y., Martin, R., Newton, Z., Pastars, D.,Sannazarro, K.L., Teece, C.I.A., 2004. Silica phases in sinters and residues from geothermal fields of New Zealand. Earth-Sci. Rev. 66, 1–61.

Rojstaczer, S., Galloway, D. L., Ingebritsen, S. E., and Rubin, D. M., 2003. Variability in geyser eruptive timing and its causes: Yellowstone National Park, Geophys. Res. Lett., 30(18), 1953, doi:10.1029/2003GL017853.

Rudolph, M. L., M. Manga, S. Hurwitz, M. J. Johnston, L. Karlstrom, and C.-Y. Wang (2012), Mechanics of old faithful Geyser, Calistoga, California, Geophys. Res. Lett., 39, L24308, doi:10.1029/2012GL054012.

Ruff, S.W., Farmer, J. D., Calvin, W. M., Herkenhoff, K. E., Johnson J. R., 2011. Characteristics, distribution, origin, and significance of opaline silica observed by the Spirit rover in Gusev crater, Mars, J. Geophys. Res. 116, E00F23. doi:10.1029/2010JE003767.

Saar, M.O., Manga, M., 1999. Permeability of vesicular basalts, Geophys. Res. Lett., 26, 111-114. doi: 10.1029/1998GL900256. issn: 0094-8276.

Schinteie, R., Campbell, K.A., Browne, P.R.L., 2007. Microfacies of stromatolitic sinter from acid–sulphate–chloride springs at Parariki Stream, Rotokawa geothermal field, New Zealand. Palaeontol. Electron. 10 (1), 1–33 (4A, http://palaeo-electronica.org/paleo/ 2007_1/sinter/index.html).

Scott, B. J. (1992), Characteristics of cyclic activity in Frying Pan and Inferno Crater Lakes, Waimangu, paper presented at 14th New Zealand Geothermal Workshop, Geotherm. Inst., Univ. of Auckland, Auckland, New Zealand.

Scott, B. J. (1994), Cyclic activity in the crater lakes of Waimangu hydrothermal system, New Zealand, Geothermics, 23, 555– 572.

Shteinberg, A.S. (1999) An experimental study of geyser eruption periodicity, Power engineering, 366, 47-50.

Shteinberg, A., M. Manga, and E. Korolev (2013), Measuring pressure in the source region for geysers, Geyser Valley, Kamchatka, Journal of Volcanology and Geothermal Research, 264, 12–16.

Sillitoe, R.H., 1993. Epithermal models: genetic types, geometrical controls and shallow features. In: Kirkham, R.V., Sinclair, W.D., Thorpe, R.I., Duke, J.M. (Eds.). Mineral Deposits Modeling: Special Paper of the Geological Association of Canada 40, pp. 403–417.

Sillitoe, R.H., 2015. Epithermal paleosurfaces. Mineralium Deposita, Vol. 50, Issue 7, pp. 767–79. DOI: 10.1007/s00126-015-0614-z.

Silver, P., and Valette-Silver, N.J. (1992), Detection of hydrothermal precursors to large northern California earthquakes, Science, 257, 1363-1368.

Soete, J., Kleipool, L.M., Claes, H., Claes, S., Hamaekers, H., Kele, S., Özkul, M., Foubert, A., Reijmer, J.J.G., Swennen, R., 2015. Acoustic properties in travertines and their relation to porosity and pore types. Marine and Petroleum Geology, Vol. 59, Pp 320–335. doi:10.1016/j.marpetgeo.2014.09.004.

Squyres S. W., Arvidson R. E., Ruff S., Gellert R., Morris R. V., Ming D. W., Crumpler L., Farmer J. D., Des Marais D. J., Yen A., McLennan S. M., Calvin W., Bell J. F.,

Clark B. C., Wang A., McCoy T. J., Schmidt M. E., and DeSouza Jr. P. A., 2008. Detection of silica-rich deposits on Mars. Science, 320(5879):1063-1067.

Steinberg, G. S., A. G. Merzhanov, and A. S. Steinberg (1982), Geyser process: Its theory, modeling and field experiment. Part 4. On seismic influence on geyser regime, Mod. Geol., 8, 79–86.

Taran, Y.A., Pokrovsky, B.G. and Esikov, A.D., 1989. Deuterium and oxygen-18 in fumarolic steam and amphiboles from some Kamchatka volcanoes:“andesitic waters”. In Dokl. Akad. Nauk SSSR (Vol. 304, pp. 440-443).

Tassi, F., C. Martinez, O. Vaselli, B. Capaccioni, and J. Viramonte (2005), Light hydrocarbons as redox and temperature indicators in the geothermal field of El Tatio (northern Chile), Appl. Geochem., 20, 2049–2062.

Tassi, F., Aguilera, F., Darrah, T., Vaselli, O., Capaccioni, B., Poreda, R.J., Delgado Huertas, A. (2010), Fluid geochemistry of hydrothermal systems in the Arica-Parinacota, Tarapacá and Antofagasta regions (northern Chile). Journal of Volcanology and Geothermal Research, 192, 1–15.

Török, Á., Vásárhelyi, B., 2010. The influence of fabric and water content on selected rock mechanical parameters of travertine, examples from Hungary. Engineering Geology, 115(3), pp.237-245.

Trujillo, P., 1969, Estudio para el desarollo geotermico enel norte de Chile. Manifestaciones termales de El Tatio, Provencia de Antofagasta: CORFO Project Report.

USGS, United States Geological Service (2014), M8.2 - 94km NW of Iquique, Chile. Web. April 1, 2014. <http://earthquake.usgs.gov/earthquakes/eventpage/usc000nzvd#general_summary>.

Vandemeulebrouck, J., P. Roux, and E. Cros (2013), The plumbing of Old Faithful Geyser revealed by hydrothermal tremor. Geophys. Res. Lett., 40, 1989–1993, doi:10.1002/grl.50422.

Vandemeulebrouck, J., Sohn, R., Rudolph, M., Hurwitz, S., Manga, M., Johnston, M., Soule, A., McPhee, D., Glen, J., Karlstrom, L., Murphy, F. (2014), Eruptions at Lone Star geyser, Yellowstone National Park, USA: 2. Constraints on subsurface dynamics, J. Geophys. Res. Solid Earth, 119, doi:10.1002/2014JB011526.

Vanorio, T., Prasad, M., Patella, D. and Nur, A., 2002. Ultrasonic velocity measurements in volcanic rocks: correlation with microtexture. Geophysical Journal International, 149(1), pp.22-36.

Walter, M.R., Des Marais, D., Farmer, J.D., Hinman, N.W., 1996. Lithofacies and biofacies of mid-Paleozoic thermal spring deposits in the Drummond Basin, Queensland, Australia. Palaios 11, 497–518.

Walter, M.R., 1972. A hot spring analog for the depositional environment of Precambrian iron formations of the Lake Superior region. Econ. Geol. 67, 965–980.

Walter, M.R., 1976a. Geyserites of Yellowstone National Park: an example of abiogenic "stromatolites". In:Walter, M.R. (Ed.), Stromatolites. Elsevier, Amsterdam, pp. 87–112.

Walter, M.R., 1976b. Hot-spring sediments in Yellowstone National Park. In:Walter, M.R. (Ed.), Stromatolites. Elsevier, Amsterdam, pp. 489–498.

Watanabe, M.M. and Kurogi, M., 1975. Taxonomic Calothrix scopulorum and C. crustacea. Botanical Magazine-Tokyo 88:111–125.

Weed, W.H., 1889. On the formation of siliceous sinter by the vegetation of thermal springs. Am J Sci 37:351–359.

Welhan, J.A. and Fritz, P., 1977. Evaporation pan isotopic behavior as an index of isotopic evaporation conditions. Geochimica et Cosmochimica Acta, 41(5), pp.682-686.

Westall, F., Boni, L., Guerzoni, E., 1995. The experimental silicificationof microorganisms. Palaeontology 38 (3), 495– 528.

Westall, F., Steele, A., Toporski, J., Walsh, M., Allen, C., Guidry, S., McKay, D., Chafetz, H., 2000. Polymeric substances and biofilms as biomarkers in terrestrial materials: implications for extraterrestrial samples. J. Geophys. Res. 105 (E10), 24,511–24,527.

Westall, F., Campbell, K.A., Breheret, J.G., Foucher, F., Gautret, P., Hubert, A., Souriel, S., Grassineau, N., Guido, D.M., 2015. Archean (3.3 Ga) microbe-sediment systems were diverse and flourished in a hydrothermal context. Geology http://dx.doi.org/10.1130/G36646.1.

White, D.E., Thompson, G.A., Sandberg, C.H., 1964. Rocks, structure, and geologic history of Steamboat Springs thermal area, Washoe County, Nevada. U. S. Geol. Surv. Prof. Pap. 458-B (63 pp.).

White, D. E. (1967), Some principles of geyser activity, mainly from Steamboat Springs, Nevada, Am. J. Sci., 265, 641–684.

White, D.E., and Marler, G.D. (1972), Fluctuations in geyser activity caused by Earth tidal forces, barometric pressure, and tectonic stresses: Comment: Journal of Geophysical Research, 77, 5825–5829, doi: 10.1029/JB077i029p05825.

Wright, H.M., Cashman, K.V., Gottesfeld, E.H. and Roberts, J.J., 2009. Pore structure of volcanic clasts: measurements of permeability and electrical conductivity. Earth and Planetary Science Letters, 280(1), pp.93-104.

Yee, N., Phoenix, V.R., Konhauser, K.O., Benning, L.G., Ferris, F.G., 2003. The effect of cyanobacteria on silica precipitation at neutral pH: implications for bacterial silicification in geothermal hot springs. Chem. Geol. 199, 83 – 90.

Zeil, W., 1959, Das Fumarolen– und Geysir–Feld westlich der Vulkangruppe des Tatio (Provinz Antofagasta, Chile). Bayerische Akademie der Wissenschaften, Abhandlung der Mathematisch-Naturwissenschaftliche Klasse: Muenchen, Deutschland, n. 96, pp 22.